ABSTRACT

Title of Document: SOLID OXIDE IONIC MATERIALS FOR ELECTROCHEMICAL ENERGY CONVERSION AND STORAGE.

Ashley Lidie Ruth, Doctor of Philosophy, 2015

Directed By: Professor Eric D. Wachsman, Materials Science and Engineering

Solid state ionic materials can be utilized in components of both solid oxide fuel cells and lithium ion batteries. Solid oxide fuel cells (SOFCs) are devices used to convert chemical energy into useful electrical energy. The higher temperatures required to effectively conduct oxygen vacancies is a material limitation that prevents the implementation of this technology in today's society. Our group has developed the novel incorporation of a bilayer electrolyte utilizing the high conductivity properties of the cubic fluorite bismuth oxide material in the low temperature regime at 650 °C and below. This phase is stabilized by single and double doping of Er, Dy-W, Dy-Ce, and Dy-Gd chemistries in this study. Conductivity measurements through electrochemical impedance spectroscopy champion $(Bi_{0.88}Dy_{0.08}Gd_{0.04})_2O_3$ as the most suitable electrolyte for future testing in SOFCs. Using the bilayer system in button type cells, the layer thickness ratio is optimized for highest open circuit

voltage. Using neutron diffraction was used to better understand the activation energy change in conductivity in DWSB due to phase transformation that masked oxygen ordering at lower temperatures. Stabilized bismuth oxides are incorporated into a suitable composite cathode via an in-situ nano-scale mixing with $La_{0.8}Sr_{0.2}MnO_{3-\delta}$, improving the oxygen reduction reaction kinetics.

Utilizing lessons from ceramic materials synthesis in SOFCs, cathode materials for Li-ion batteries were synthesized. In previous work, $Li_xMn_2O_{4-y}Cl_z$ spinel demonstrated enhanced charge potential and discharge potential while maintaining reversibility. However the original method for synthesis was extremely cumbersome. Using the simple glycine-nitrate reaction, we could fabricate an operating button cell starting from raw powders in less than 8 hours. X-ray diffraction and x-ray fluorescence confirm spinel structure and maintenance of chlorine through ignition respectively. In demonstrating favorable charge/discharge performance and cyclability, we considered the benefits of B-site doping of the spinel. For the first time $Li_xMn_{2-w}Fe_wO_{4-y}Cl_z$ was also easily synthesized and tested for more than 250 charge-discharge cycles with 98% capacity retention. Similarly, Ni is introduced to the $Li_xMn_2O_{4-y}Cl_z$ spinel in order to take advantage of the intrinsic redox couple of Ni^{2+}/Ni^{4+} at 4.7V and demonstrate reversibility from 5.0 V to 2.0 V.

SOLID OXIDE MATERIALS FOR ELECTROCHEMICAL ENERGY CONVERSION AND STORAGE

By

Ashley Lidie Ruth

Dissertation submitted to the Faculty of the Graduate School of the
University of Maryland, College Park, in partial fulfillment
of the requirements for the degree of
Doctor of Philosophy
2015

Advisory Committee:
Professor Eric D. Wachsman, Chair
Dr. Terrill B. Atwater
Professor Isabel Lloyd
Professor Chunsheng Wang
Professor Efrain Rodriguez

Dedication

I dedicate this to my loving husband for believing in me and supporting me when I needed it most.

Acknowledgements

I would like to acknowledge the mentorship of influential undergraduate mentors, Dr. Isabel Lloyd and Mr. Steve Kilczewski. Your guidance in academia and in the lab is a major factor in my achievements today as you have nurtured my education since I was but a budding materials scientist.

For saving me on more than one occasion, I must thank Kathleen Hart for all of her efforts. I have had the pleasure of knowing you for about 9 years and any time I needed help you swiftly took care of it for me.

I wish to also acknowledge my early graduate school mentor, Dr. Kang Taek Lee, for his guidance as I began my graduate school career and teaching me how to apply influential science.

I must certainly acknowledge my office mates, Colin Gore, Yilin Huang, Keji Pan, Gregory Hitz, Chris Pellegrinelli, Tom Hays, and Adam Jolley for countless hours of both useful and absolutely counterproductive (yet always intriguing) conversation. Colin for your leadership as our senior lab member, and allowing me to be your first undergraduate assistant. Yilin and Keji, for offering valuable advice for my work. Greg and Chris, you have become friends I hope to stay in touch with for a lifetime. Tom and Adam, you are welcome additions to our group and I have seen great things from both of you.

Dr. Hee Sung Yoon, you have been an absolutely invaluable resource. You have helped me in all aspects, and most notably for all your effort you put into the anode substrates just to hand them off to me for my work. While I wish you took

better notes, I also wish I could tap into all the knowledge you contain. Thank you for being a great role model.

Dr. Keith Duncan, thank you for your assistance with understanding my data for the bilayer system. Your work was a tremendous help, and I appreciate your effort in providing insight to the theory and modeling.

Much of the credit to the work in neutron diffraction goes to Dan Taylor and Craig Brown for helping me run the experiment itself, and taking the time to perform the refinement to a level beyond my ability. Thank you for all of your help in probing the properties of my material.

The oxygen isotope exchange experiment required the effort of Gil Cohn, Chris Pellegrinelli, and Yilin Huang. Thank you all for helping me acquire the useful information about my material.

For his overwhelming level of aptitude and success, I must of course thank my advisor, Dr. Eric Wachsman. You had saved me from far more than you know by picking me up when you did. And you helped me beat the odds against me, and allowed me to achieve my dream. You are such an influential member of society, and I thank the stars that our world has people like you with the drive to do something to make this world better.

At Army Power, I must acknowledge Terrill Atwater and his angels: Lauren Marzocca, Paula Latorre, Cassandra Reilly, Julie Douglas, and Yakira Kirzner as well as the entire Battery Team and Army Power Division. Everyone has been so welcoming and in the few short summers I spent there I know I have made

friendships that will last forever. Terrill, you have been an absolutely wonderful mentor and I look forward to working with you upon graduation.

I must also thank my life heroes. Dad, somehow we did it. My in-laws Kelly and Steve, for supporting me so much and always being willing to stand up for me. Maria, Sandy, Sharon, and Latina, for getting me through. Uncle Bruce, for treating me like one of your own. I miss you so much, rest in peace. My big brother Dave for being the one person who just understands. And finally my husband Steve for being my dream come true and my biggest fan.

I must acknowledge the availability of facilities and their operators for helping acquire much of this data: Dr. Peter Zavalij in the X-ray Crystallographic Center, Dr. Wen-An Chiou, John Abrahams, and Larry Lai from the Nanocenter's Fablab and NISP Lab, Dr. Craig Brown and NIST for the use of the NCNR neutron facility, and Mr. Ed Plichta for the use of DOD facilities.

This work has been supported by the American Society of Engineering Education via the Science, Mathematics & Research for Transformation Scholarship. This work has been funded by Redox Power Systems, LLC.

Table of Contents

List of Tables

List of Figures

List of Acronyms

1LMNO-Cl - Chlorinated lithium manganese oxide spinel with nickel doping on the B-site (of $AB_{2-y}M_yO_{4-d}Cl_d$) where y = 0.1.
2LMNO - Lithium manganese oxide spinel with nickel doping on the B-site (of $AB_{2-y}M_yO_4$) where y = 0.2.
2LMNO-Cl - Chlorinated lithium manganese oxide spinel with nickel doping on the B-site (of $AB_{2-y}M_yO_{4-d}Cl_d$) where y = 0.2.
3LMNO-Cl - Chlorinated lithium manganese oxide spinel with nickel doping on the B-site (of $AB_{2-y}M_yO_{4-d}Cl_d$) where y = 0.3.
4LMNO-Cl - Chlorinated lithium manganese oxide spinel with nickel doping on the B-site (of $AB_{2-y}M_yO_{4-d}Cl_d$) where y = 0.4.
5LMNO-Cl - Chlorinated lithium manganese oxide spinel with nickel doping on the B-site (of $AB_{2-y}M_yO_{4-d}Cl_d$) where y = 0.5.
6D3CSB - 6 mol% dysprosium 3 mol% cerium stabilized bismuth oxide
6D3GSB - 6 mol% dysprosium 3 mol% gadolinium stabilized bismuth oxide
8D4CSB - 8 mol% dysprosium 4 mol% cerium stabilized bismuth oxide
8D4GSB - 8 mol% dysprosium 4 mol% gadolinium stabilized bismuth oxide
8D4WSB - 8 mol% dysprosium 4 mol% tungsten stabilized bismuth oxide
10D5CSB - 10 mol% dysprosium 5 mol% cerium stabilized bismuth oxide
10D5GSB - 10 mol% dysprosium 5 mol% gadolinium stabilized bismuth oxide
AFL - Anode functional layer
AMT - Ammonium metatungstate hydrate
ASR - Area specific resistance
BBP - Butyl benzyl phthalate
BET - Brunauer Emmett, and Teller surface area analysis method
BSCF - Barium strontium cobalt ferrite
CE - Counter electrode
CERDEC - Communication Electronics Research, Development, and Engineering Center
CP - Co-precipitation
DCSB - Dysprosium cerium stabilized bismuth oxide
DEC - Diethyl carbonate
DGSB - Dysprosium gadolinium stabilized bismuth oxide
DI-H20 - Deionized water
DMC - Dimethyl carbonate
DWSB - Dysprosium tungsten stabilized bismuth oxide
EC - Ethylene carbonate
EDS/EDX - Energy dispersive X-ray spectroscopy
EIS - Electrochemical impedance spectroscopy
ESB - Erbium stabilized bismuth oxide with 20 mol% Er doping
ESL - ElectroScience (Company)
FEC - Fluoroethylene carbonate
GDC - Gadolinia-doped ceria
G/N - Glycine to nitrate ratio

GNP - Glycine nitrate process/combustion
HDPE - High density polyethylene
ICE - Internal combustion engine
icn - in situ coassembled nanocomposite
IIE - in situ isotope exchange
IV - Current-voltage, usually referring to galvanodynamic result
JCPDS - Joint Committee on Powder Diffraction Standards (diffraction catalog)
LDPE - Low density polyethylene
LiFSI - Lithium bis(fluorosulfonyl)imide
LMFO - Lithium manganese oxide spinel with iron doping on the B-site of $AB_{2-y}M_y O_4$.
LMO - Lithium manganese oxide
LMO-Cl - Chlorinated lithium manganese oxide
LMNO - Lithium manganese oxide spinel with nickel doping on the B-site of $AB_{2-y}M_y O_4$.
LMNO-Cl - Chlorinated lithium manganese oxide spinel with nickel doping on the B-site of $AB_{2-y}M_y O_4$.
LSC - Lanthanum strontium cobalt oxide
LSCF - Lanthanum strontium cobalt ferrite
LSM - Lanthanum strontium manganese oxide
MIEC - Mixed ionic electronic conductor
MPD - Maximum power density
NBSR - Neutron Beam Split-Core Reactor
NCNR - NIST Center for Neutron Research
NISP - Nanoscale Imaging, Spectroscopy, and Properties Laboratory
NIST - National Institute of Standards and Technology
OCV - Open circuit voltage
ORR - Oxygen reduction reaction
PEM - Proton exchange membrane
PTFE - Polytetrafluoroethylene (trade name Teflon)
PVB - Polyvinyl butryal
RE - Reference electrode
ScSZ - Scandium stabilized zirconia
SE - Sensing electrode
SEM - Scanning electron microscope
SMART - Science, Mathematics and Research for Transformation
SNDC - Samarium neodymium doped ceria
SOFC - Solid oxide fuel cell
SS - Solid state
SSC - Samarium strontium cobalt oxide
STEM - Scanning transmission electron microscope
TEM - Transmission electron microscope
TGA - Thermogravimetric analysis
TPB - Triple phase boundary
WE - Working electrode
XRD - X-ray diffraction

XRF - X-ray fluorescence
YSB - Yttrium stabilized bismuth oxide
YSZ - Yttrium stabilized zirconia

Chapter 1: General Introduction

1.1 Solid oxide fuel cells

Solid oxide fuel cells (SOFCs) offer a feasible method for reducing the impact of fossil fuels due to higher efficiency over the traditional internal combustion engine (ICE). With negligible NO_x and SO_x emissions, and less than half of the CO_2 emissions, SOFCs can reduce acid rain and smog causing pollutants, and bring CO_2 emissions to a range comparable to an amount photosynthetic plants are capable of converting (35). Currently, renewable energy is not capable of taking on the global power demand due to technology limitations or non-sustainable sources, like wind or available sunshine. As a gateway technology, current infrastructure can be maintained for use with SOFCs due to the capability for operation with hydrocarbon fuels. This is a significant advantage over the proton exchange membrane (PEM) as they must operate with pure hydrogen, and there are still significant barriers to the hydrogen market requiring advances in hydrogen storage and transport.

A fuel cell is an electrochemical device consisting of three main parts: a solid state ionically conductive electrolyte separating an anode for fuel oxidation and cathode to accept the oxidizer. Several fuel cells have been studied over time, including microbial fuel cells, phosphoric acid fuel cells, molten carbonate fuel cells, direct methanol fuel cells, SOFCs and PEM fuel cells, among a number of others. Fig.1.1.1 shows a schematic of both SOFCs and PEM fuel cells to demonstrate their operation of conducting either a proton or oxygen ion through the electrolyte with charge compensation through electron current in an external circuit (4). Due to the

difference in conducting species, the redox reactions vary. In the case of a PEM the cathode reaction is:

$$\frac{1}{2}O_2(g) + 2H^+ + 2e' \rightarrow H_2O \qquad \textit{(Eq. 1.1)}$$

and the oxidation reaction at the hydrogen anode is:

$$H_2 \rightarrow 2H^+ + 2e' \qquad \textit{(Eq. 1.2)}$$

In the case of SOFCs, at the cathode, the oxygen reduction reaction is of the general form:

$$\frac{1}{2}O_2(g) + 2e' \rightarrow O^{-2} \qquad \textit{(Eq. 1.3)}$$

and the oxidation reaction at a hydrogen anode is of the general form:

$$H_2 + O^{-2} \rightarrow H_2O + 2e' \qquad \textit{(Eq. 1.4)}$$

The most widely studied of these is the PEM fuel cell largely due to the linking of fuel cells with the push towards a future hydrogen economy (1). However, as mentioned above, a hydrogen economy is not a short term reality, and SOFCs can meet the energy demand with existing conventional fuels.

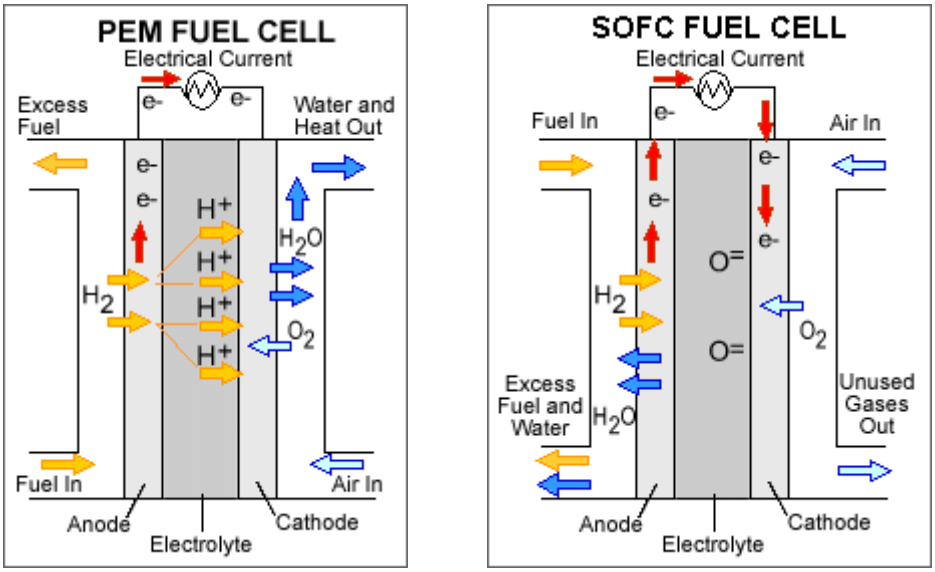

Figure 1.1.1: Diagrams of PEM fuel cell and Solid Oxide Fuel Cell operation among three material components: anode, cathode, and electrolyte (4).

The main shortcoming of bringing this technology to market is its high temperature operation. Typical fuel cells, including ones currently in the market like the Bloom Energy Server, require temperatures at or even above 900°C for operation due to material limitations of the ionic conducting oxide yttrium stabilized zirconia (YSZ). YSZ has ionic conductivity of ~ 0.1 S/cm at 1000°C, and therefore requires ceramics for insulation and interconnects as well as start up energy to reach such high temperatures (36). In order to bring costs down, it would be ideal to operate in the low temperature regime of 500 °C - 700 °C. A suitable electrolyte would need to have high oxygen ion conductivity in this temperature range, negligible electronic conductivity, and mechanical and chemical stability over a wide range of temperatures and oxygen partial pressures (37).

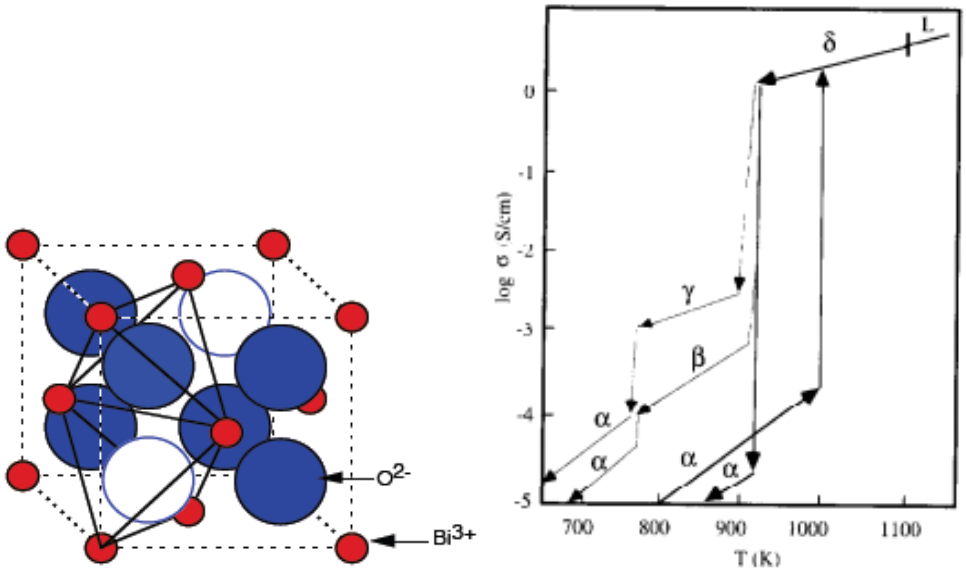

Figure 1.1.2: a) Schematic of δ-Bi_2O_3 cubic fluorite structure showing 3/4 oxygen site occupancy and b) phase diagram from Shuk et al. showing stability region of the δ fluorite phase (5)

Cubic bismuth oxide exhibits the highest ionic conductivities at lower temperatures due to its defect fluorite structure, shown in Fig. 1.1.2a (38-40). Intrinsic to the structure are two oxygen vacancies per unit cell because only six of the eight possible oxygen sites are filled. However, as shown in Figure 1.1.2b, this phase in Bi_2O_3 only exists between 730 °C and melting at about 824 °C (5, 41).In order to take advantage of this material's properties, the phase must be stabilized by the addition of dopants to stabilize the lattice for low temperature applications. Several lanthanides of smaller atomic radii than bismuth have been used to stabilize this phase, each having their own minimum doping concentration to do so. Verkerk et al. shows that the lowest total concentration for stabilization with single doping occurs with erbium at 20 at% (6-7) (Figure 1.1.3). They demonstrated that this correlated to the highest conductivity among Er, Yb, Y, Dy, and Gd, indicating that lower total doping should yield better performance due to the limitation of defect

association at higher concentrations (6-7). The conductivity trends tend to follow the atomic radii of the dopant, being smaller but close to the ionic radius of bismuth, but the long term stability tends to follow the polarizability of the dopant, as demonstrated by Wachsman (42-43).

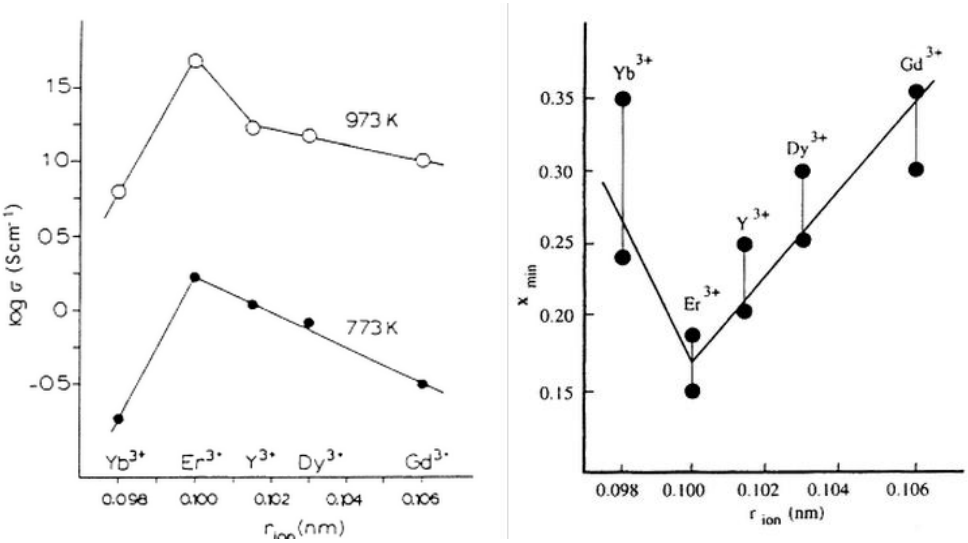

Figure 1.1.3: Verkerk and Burggraaf results showing a) conductivity of doped Bi_2O_3 with minimum doping level for stabilization of the phase versus ionic radius of the dopants and b) X_{min} as a function of ionic radius (r_{ion}) of the dopant ion. (6-7)

Understanding the ideal dopant properties of polarizabiltiy and ionic radius to achieve stability at lower total doping, a double-doping technique is employed to increase entropy and achieve even lower total doping. Using this strategy with dopants dysprosium and tungsten, Wachsman has demonstrated a 3-fold increase in ionic conductivity over erbium stabilized bismuth oxide (ESB) with just 12 at% total doping (39, 44). This result is shown in Fig.1.1.4 adapted from Wachsman et al. (1). One can see the relative conductivity of this higher conductivity bismuth oxide material over another electrolyte material, gadolina doped cerium oxide (GDC), and YSZ.

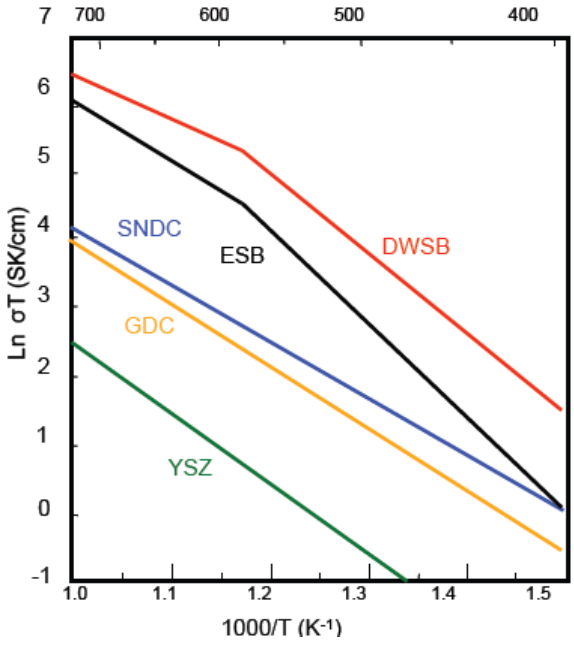

Figure 1.1.4: Comparison of ionic conductivity of various solid oxide electrolytes. Stabilized bismuth oxides (ESB-Er 0.4Bi1.6O3and DWSB-Dy0.08W0.04Bi0.88O1.56) show superior ionic conductivity compared with that of doped ceria (GDC-Gd0.1Ce0.9O1.95 and SNDC-Sm0.075Nd0.075Ce0.85O2-d) and stabilized zirconia (YSZ-Y0.16Zr0.92O2.08) (1).

A major shortcoming of bismuth oxide is its decomposition at low P_{O2}, making it unsuitable for use at the fuel side of the cell (1, 45-47). In order to protect the bismuth oxide layer, another electrolyte material is used as a barrier to create higher interfacial P_{O2} (1, 47). This bilayer system takes advantage of GDC's enhanced conductivity over conventional YSZ. Additionally, GDC is suitable because ESB can act as a blocking layer for leakage current due to its partial electronic conductivity at operating temperatures (47). This unique design allows for utilization of the high conductivity bismuth oxide and has been demonstrated to show greatly enhanced power density experimentally. Ahn et al. has shown a reduction in ASR from 0.13 Ωcm^2 to 0.08 Ωcm^2 and a power density increase from 1W/cm^2 to 2W/cm^2 at 650 °C between GDC only and the ESB/GDC electrolyte through the pulsed laser deposition of ESB onto the GDC electrolyte (47).

The bilayer concept has been demonstrated but there must be a reasonable method to deposit dense bismuth oxide materials. This work hopes to take advantage of nano-scale processing of bismuth oxide powders in conjunction with higher conductivity double-doped bismuth oxide to be able to easily and inexpensively fabricate experimental cells with dense thin layer bismuth oxide electrolytes. Testing of these cells to reveal true benefits of this design via reasonable synthesis routes will prove beneficial for bringing low temperature SOFCs to market.

1.2 Lithium ion battery cathodes

Lithium ion batteries with their high energy density are perhaps the most successful solution for small scale portable electronic devices like cell phones and laptops. However, there is a drive for optimizing these systems to support the emerging large scale technologies in transportation. One of the key challenges to bringing electric vehicles to market is developing cathode materials with high energy density. Some of the more popular cathode materials include $LiCoO_2$, $LiFePO_4$, layered $LiNiO_2$, and $LiMn_2O_4$ spinel. $LiCoO_2$ has excellent cycling stability and superior capacity, but is high in cost, and most importantly lacks the safety required for use in personal vehicles (48-50). The latter three options are all safe solutions, but reasonable capacity for $LiFePO_4$ requires expensive synthesis for making nanopowder with carbon coating (51).

Lithium manganese spinel meets cost and safety requirements as well as comparable capacity and high specific energy (~610 Wh/kg) (49). This coupled with the higher voltage capability makes them very attractive as future cathode materials.

The lattice acts as a 3D network for fast lithium insertion and exit, this is shown visually in Fig. 1.2.1a (8). Unfortunately, these materials suffer from limited cycle life due to gradual degradation of the microstructure due to fracturing or the spinel structure either through the Jahn-Teller distortion, loss of crystallinity, or alternative phase formation usually due to non-stoichiometry (52-54). It is important to address these concerns through inexpensive options for stabilizing the structure to achieve limited capacity fading during cycling. The most common method is to dope with accessible transition metals, and is discussed later. Our group considered introducing various halogens into the material to attempt to address these concerns and achieved success with the addition of Cl to form $Li_xMn_2O_{4-y}Cl_z$ (55). In the resulting patent of this work, only solid state methods were used for synthesizing this material (9). Going to the nano-scale can help further extend the cycle life of this material by eliminating the negative impacts from fracturing and enhancing lithium insertion kinetics.

By considering both the addition of B-site dopants of transition metals and halogenated spinels, we can try to enhance the properties of existing materials through fast nano-scale synthesis. Combined we expect to see improvements in durability both in terms of cycle life and extreme cycling conditions requiring more than one stoichiometric lithiation/delithiation.

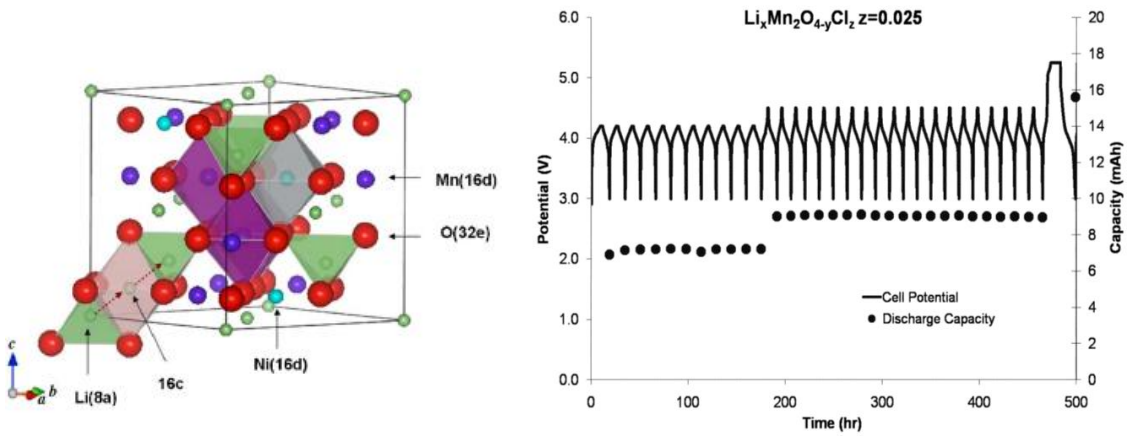

Figure 2.2.1: a) Diffusion path of lithium in the spinel $LiNi_{0.5}Mn_{1.5}O_4$ (8). b) Charge/discharge cycling of $Li_xMn_2O_{4-y}Cl_z$ (9).

Chapter 2: Experimental Procedures

Several synthesis, fabrication, and measurement techniques were employed during the study of the various ceramic materials for SOFCs and Li-ion batteries. This chapter discusses all of the synthesis techniques for materials, the fabrication of cells for electrochemical testing including testing apparatus, and the preparation of samples and methods for characterization.

2.1 Materials

2.1.1 Solid State Oxide Synthesis

Solid state (SS) synthesis of doped metal oxides requires individual metal oxide powders of the final material constituents. For all of the bismuth oxides studied in this work, Bi_2O_3 (Alfa Aesar) was used. To make ESB, DWSB, DCSB, and DGSB, stoichiometric amounts of Er_2O_3 (Alfa Aesar), Dy_2O_3 (Alfa Aesar), WO_3 (Alfa Aesar), CeO_2 (Alfa Aesar), or Gd_2O_3 (Alfa Aesar) were added to the bismuth oxide. The materials were milled in a 125 mL HDPE bottle with spherical 5mm yttria-stabilized zirconium oxide milling media in ethyl alcohol for 24 to 72 hours. The material was collected through a 40 μm (325 mesh) sieve and dried at 100 °C. The material was calcined at 800 °C for 16 hours to achieve the appropriate fluorite phase. The powder was ground and sieved through a 40 μm (325 mesh) sieve and milled again in ethyl alcohol for 24 hours. The powder was collected and dried at 100 °C.

2.1.2 Reverse Strike Coprecipitation Synthesis

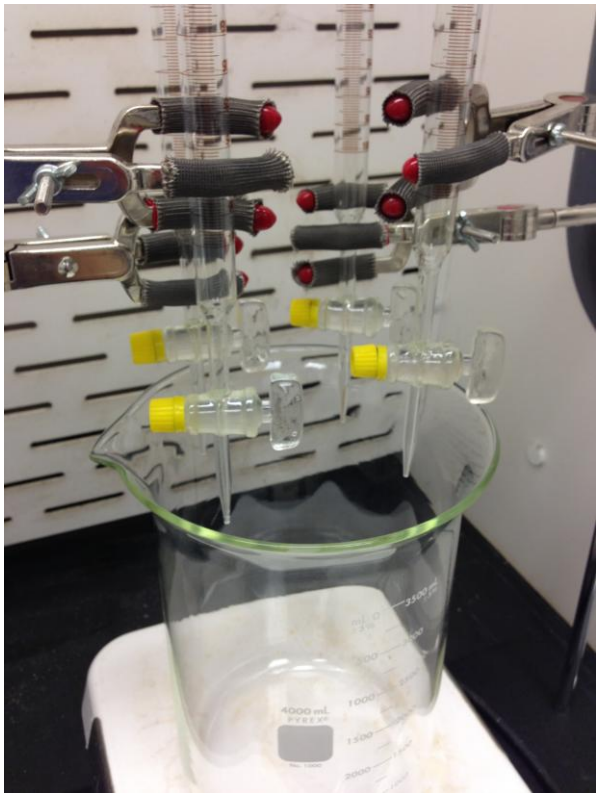

Figure 2.1.1: High throughput set up for coprecipitation synthesis where the acid solution containing the metal precursors (less the tungsten precursor) are loaded into the burets and are added into the base solution stirring in the beaker.

To make nano-sized powder reverse strike coprecipitation (CP) was employed to maintain pH above 10 and prevent the formation of $BiONO_3$ (56). To make ESB, DGSB and DCSB via co-precipitation, stoichiometric amounts of $Bi(NO_3)_3 \cdot xH_2O$, $Er(NO_3)_3 \cdot 5H_2O$, or $Dy(NO_3)_3 \cdot 5H_2O$, and either $Gd(NO_3)_3 \cdot xH_2O$ or $Ce(NO_3)_3 \cdot 6H_2O$ (Alfa Aesar) were dissolved in 100 mL of HNO_3 with a metal ion concentration of 0.5M. This acid solution is added to a stirring 500 mL of NH_4OH drop wise at a rate of 2 mL/min. In the case of DWSB, $(NH_4)_{10}W_{12}O_{41} \cdot 5H_2O$ (AMT, Alfa Aesar) was dissolved in the 500 mL of NH_4OH in the appropriate stoichiometric proportion with Dy^{3+} and Bi^{3+} ions due to AMT's incompatibility with the acid prior to acid solution addition. The precursor formed upon acid solution addition was rinsed and filtered

through a 220 nm nitrocellulose filter 3 times with DI H_2O and rinsed once more with isopropanol and dried at 100 °C. The precursor was milled with ethanol in a HDPE mill with 5 mm yttria-stabilized zirconia ball media for 24 hours. The powder was then calcined from 400 °C to 550 °C for up to 5 hours to achieve the appropriate phase. The calcined powder was milled again in ethanol for 24 hours and passed through a 325 mesh sieve.

2.1.3 Glycine Nitrate Combustion Synthesis

Another common ceramic synthesis technique for achieving nano-sized powder is the glycine nitrate process (GNP). This work utilizes this method for synthesis of bismuth oxide electrolyte materials, SOFC cathodes LSM/ESB and LSM/DWSB, and for the chlorination and synthesis of the lithium manganese oxide spinel with and without b-site dopant additions.

2.1.3.1 Electrolyte

Bismuth oxide electrolytes were also synthesized using GNP in addition to the previously discussed CP and SS methods. This method, like CP, is used to achieve nanoscale powders. To make ESB, DGSB and DCSB via glycine nitrate combustion, stoichiometric amounts of $Bi(NO_3)_3 \cdot xH_2O$, $Er(NO_3)_3 \cdot 5H_2O$, or $Dy(NO_3)_3 \cdot 5H_2O$, and either $Gd(NO_3)_3 \cdot xH_2O$ or $Ce(NO_3)_3 \cdot 6H_2O$ (Alfa Aesar) were dissolved in DI H_2O and 10 vol% HNO_3 to fully dissolve the bismuth nitrate. NH_2CH_2COOH (glycine) was added to and dissolved in the solution as a chelating agent with a glycine to metal ratio of 1:1. In the case of DWSB, the bismuth and dysprosium nitrates were treated like above, but $(NH_4)_{10}W_{12}O_{41} \cdot 5H_2O$ was dissolved in DI H_2O separately. The solution(s) were poured into a beaker already at 90 °C on a hot plate. The heat was

then set to 120 °C for evaporation. The remaining gel was then heated to 300 °C until auto-ignition occurs. Once the ash formed, it was collected and ground in a mortar and pestle. The ash was milled in a HDPE bottle in ethanol with 0.5 cm spherical YSZ milling media for 24 hours. The powder was dried at 80 °C and then calcined at 550 °C for 2 to 4 hours. Again the powder was milled in ethanol for 24 hours and dried at 80 °C.

2.1.3.2 SOFC Cathode

A cathode material was made with precursor bismuth oxide powder (in this work, CP ESB or GNP DWSB prior to calcination) by incorporating it into a composite cathode with $La_{0.80}Sr_{0.20}MnO_{3-\delta}$ (LSM). To achieve nano-scale mixing, the powders were combined by using the glycine-nitrate process to coat the ESB or DWSB with LSM. Stoichiometric amounts of $La(NO_3)_3 \cdot 6H_2O$, $Sr(NO_3)_2$, and $Mn(NO_3)_2 \cdot 5H_2O$ (Alfa Aesar) were dissolved in 5mL of DI H_2O. NH_2CH_2COOH (glycine) was added to and dissolved in the solution as a chelating agent with a glycine to metal ratio of 1.3:1. Bismuth oxide precursor powder was then stirred into this solution in a 50:50 mass ratio of LSM to DWSB or 30:70 mass ratio of LSM to ESB. The mixture was heated to 80 °C to evaporate the water while stirring. The mixture was heated further to 300 °C until the self-ignition occurs. The resulting ash was ground in a mortar and pestle and milled with ethanol in a HDPE mill with 5 mm zirconia ball media for 24 hours. The powder was collected and dried, and fired to 800 °C for 2 hours to calcine the LSM phase. The calcined powder was then milled again in ethanol for 24 hours.

2.1.3.3 Li-ion Battery Cathode

A glycine nitrate combustion method was used to synthesize lithium manganese oxide spinels with and without anion doping. B-site dopants to the AB_2O_4 structure were also added using this method when applicable. For no chlorine addition, stoichimetric amounts of $Li(NO_3)$ and $Mn(NO_3)_2{\cdot}4H_2O$ (Alfa Aesar) were mixed and dissolved in DI H_2O. When adding chlorine, stoichiometric amounts of $Li(NO_3)$, $MnCl_2{\bullet}4H_2O$ and $Mn(NO_3)_2{\cdot}4H_2O$ (Alfa Aesar) were mixed and dissolved in DI H_2O. For iron and chlorine, stoichiometric amounts of $Li(NO_3)$ and $Mn(NO_3)_2{\cdot}4H_2O$ (Alfa Aesar) with $FeCl_3$ were mixed and dissolved in DI H_2O. And finally for the addition of nickel, stoichiometric amounts of $Li(NO_3)$, $MnCl_2{\bullet}4H_2O$, $Ni(NO_3)_2{\bullet}6H_2O$ and $Mn(NO_3)_2{\cdot}4H_2O$ (Alfa Aesar) were mixed and dissolved in DI H_2O. NH_2CH_2COOH (glycine, Alfa Aesar) was dissolved into the aqueous solution as a chelating agent in a 1:1 metal ion to glycine ratio. The solution was heated to 80 °C until the water fully evaporated and a gel was formed. The gel was heated further to 250 °C when auto ignition occurs and formed a black ash. The ash was collected and ground in a mortar and pestle and fired at 600 °C for two to ten hours to achieve the desired phase.

2.2 X-ray Diffraction

All powders were ground in mortar and pestle in order to achieve fine particles for the measurement. Powders were mounted in either a polymer or silicon sample holder and a glass slide is used to gently press the powder flat. Samples were analyzed with a Bruker D8 Advance, Cu K_α either at the X-ray Crystallographic Center at the University of Maryland or at the Army Power Division facility.

2.3 Neutron Diffraction

Solid state DWSB powders were first synthesized according to section 2.1.1. 10g of powder were then pressed into two pellets using a Carver uniaxial pellet press and Carver 1.25" diameter die. The pellets were sintered at 890 °C for 16 hours in an alumina crucible and quenched in air to room temperature. One of these pellets was then ground in a mortar and pestle and is referred to as 0 hrs annealing. The remaining pellet was annealed in an alumina crucible at 500 °C for 100 hours. This pellet was ground into powder in a mortar and pestle. 0 hrs and 100 hrs powders are taken to the National Institute of Standards and Technology. Neutron powder diffraction data were collected using the BT-1 32 detector neutron powder diffractometer at the NCNR, NBSR. A Cu(311) monochromator with a 90° take-off angle, *lambda* = 1.5398(2) Å, and in-pile collimation of 60 minutes of arc were used. Data were collected over the range of 3-168° *2-Theta* with a step size of 0.05°. The instrument is described in the NCNR WWW site (http://www.ncnr.nist.gov/). The sample was loaded in a vanadium can sample container of length 50 mm and diameter 9.2 mm. Data were collected under ambient conditions. Refinement of the diffraction data, both Rietveld and Le Bail, were performed with the TOPAS software suite (Bruker AXS, Karlsruhe, Germany) (24-25).

2.4 BET Measurement

Powders were loaded into glass bulb sample containers to a mass of 0.5g to 1g using aluminum foil covering to minimize static along the neck of the sample tube. A glass filler rod was added to the sample container to minimize empty volume. A fritted gas-tight cap with rubber ball control was added to the top of the sample

container. The container was loaded onto a degas channel of a Micromeritics ASAP 2020 in the University of Maryland Nanocenter FabLab. For bismuth oxide or LSM-bismuth oxide powders, degas pressure was maintained above 30 mmHg and temperature never exceeded 100 °C due to its susceptibility to reduction in low ρO_2. For lithium battery cathodes, the degas conditions allowed 5 mmHg and 150 °C during evaporation phase. After degas, the sample was loaded onto the testing setup with a liquid nitrogen bath and porous polymer sleeve on the sample container to act as a wick. An 80-point measurement was performed with a dosing of 0.1 cm^2/g of N_2. The instrument software created a report that provided key information, namely the BET specific surface area, pore size, and average particle size.

2.5 Dynamic Light Scattering

DWSB powder was sonicated in DI H_2O. Using a Horiba LA-910 at the U.S. Army Research Laboratory, a quartz cell was blanked and then the appropriate amount of powder dispersion was added to the cell with a stir bar. The measurement was performed with a refractive index of 2.2 for bismuth oxide at the wavelength of the red laser (57). Using the Brownian motion of the particles as they move within the measurement laser, the intensity of their Rayleigh scattering will fluctuate over time. From this time information a correlation can be made to the particle's size, and a particle size distribution was generated.

2.6 X-ray Fluorescence (XRF)

A Bruker S2 Ranger with a palladium source at the Army Power Division facility was used for determining chemical constituents of the powders. The powder

was loaded into a polymer sample holder. The sample was loaded into the measurement chamber and pulled to a vacuum for analysis. The metal experimental file was used for calculating the mol % of each metal constituent using the peaks generated from the measurement.

2.7 Thermogravimetric Analysis

Thermogravitmetric analysis (TGA, Perkin Elmer Pyris 1) was performed from 30 °C to 750 °C at a ramp rate of 10°C per minute in flowing air on the lithium spinel cathode precursor ash material prior to firing in a Pt boat to confirm calcination is complete at 600 °C. The sample is held at 750 °C for 30 minutes and then cooled at 20 °C per minute down to room temperature.

2.8 SEM and EDS

An aluminum sample holder was used for all SEM use. For powder imaging, double sided carbon tape was placed onto the sample holder and the powder was smeared onto the exposed tape. For dense part imaging, the surface was placed face-up on top of the sample holder or for cross-sectional images, was carbon-taped to the side of the sample holder. The carbon tape was added to the imaging surface to attempt to minimize charging of the non conductive species.

A Hitachi SU-70 in the NISP Lab in the Nanocenter at the University of Maryland was used. For SEM imaging, 2.0 keV was used as the accelerating voltage. Secondary electron images were captured with either mixed or lower detectors for topographical resolution and perception. For ease of visually determining separate

chemical components, the upper detector in back-scattered mode with H.A. 100 condition.

EDS was performed with the Bruker silicon drift detector attachment on the Hitachi SU-70. Samples were measured with 20-30 keV accelerating voltage at a working distance of approximately 15 mm.

2.9 TEM Preparation

LSMESB and LSMDWSB powders were mixed with isopropanol. Using a pipette, the powders were dropped onto a lacey carbon TEM substrate. With the assistance of Larry Lai at the NISP Facility at the University of Maryland, the materials were imaged on a JEOL 2100F and the attached EDS system was used to create area maps of the particles.

2.10 Symmetric Cell Fabrication

Symmetric cells are used when determining the conductivity of electrolyte materials and area-specific resistance (ASR) of cathode materials using electrochemical impedance spectroscopy (EIS), which is discussed later. In this work, symmetric cells are electrolyte-supported cells with symmetric configuration with either a current collector only on both sides or with a cathode and current collector on both sides.

2.10.1 Bismuth Oxide Electrolyte

Pellets were pressed from bismuth oxide powders as synthesized in section 2.1. A uniaxial Carver press was used with a 10 mm die to 830 kPa and approximately 0.7 to 1.0 g of powder was used. Pellets made using solid state

powder were fired at 890 °C for 10 to 16 hours. Pellets made from either CP or GNP methods were fired at 750 °C to 800 °C for 4 hours due to the higher surface area that allows for lower temperature sintering. After sintering, pellets were ground to 1-2 mm in thickness. Pellets were painted with platinum paste (Heraeus) and dried at 100 °C on both sides as current collectors. An actual symmetric cell is shown below in Figure 2.10.1.

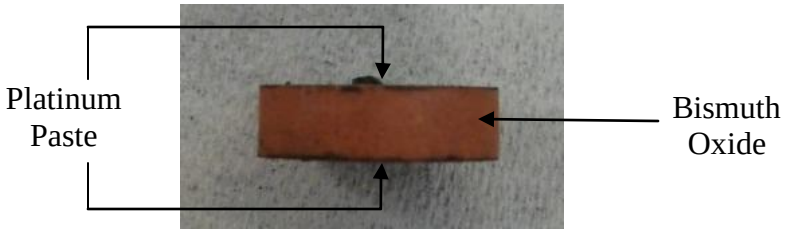

Figure 2.10.1 Design of the symmetric cell

2.10.2 LSM/Bismuth Oxide Cathode

SS powders were used for making the electrolyte substrate for symmetric cells designed for cathode analysis. As described in the previous section, between 0.7 g to 1.0 g of powder was pressed in a 10 mm die to 830 kPa. Pellets were fired at 890 °C for 10 to 16 hours and ground to about 1-2 mm thick.

LSMESB and LSMDWSB as synthesized in section 2.1 were milled in ethanol in a 125 mL HDPE bottle with 0.5 cm spherical YSZ milling media for 24 hours. The solution was dumped into a THINKY compatible LDPE cup. A THINKY ARE-310 was used with 1500 rpm for both the mixing and de-airing cycles. The solution was continuously mixed until most of the ethanol has evaporated. Prior to full ethanol evaporation, ESL 441 vehicle (Electroscience Lab) was added to achieve the appropriate viscosity. The mixture was mixed again in the THINKY until all of the ethanol was evaporated. More ESL 441 may be added if the mixture is too

thick for the appropriate elasticity. The resulting ink was applied with a paint brush to the surface of the sintered SS pellet and allowed to dry at 100 °C for about 30 minutes. A second coat was applied in the same way and again dried at 100 °C for 30 minutes. This double-coating was repeated on the second side of the pellet. Then platinum paste (Heraeus) was applied to each side and dried at 100 °C. Figure 2.10.1 is similar to this cell with the only difference being the cathode layer is underneath the platinum paste. The thickness of the cathode is on the order of 30 μm and is not resolvable from the cross section with the naked eye.

2.11 SOFC Button Cell Fabrication

Button cells are full cells consisting of a supportive anode with an applied anode functional layer (AFL), a thin electrolyte, and a cathode. These button cells are approximately 1" in diameter and less than 1 mm thick. In this work they were used for studying the electrochemical performance of the electrolyte and cathode via galvanodynamic measurements and EIS. Figure 2.11.1a shows a schematic of a typical button cell with a top view of an actual cell in Figure 2.11.1b. Gadolinia-doped cerium oxide (GDC) is an ionic conductor used as an electrolyte and also incorporated into the anode and anode functional layer with nickel oxide (NiO). These components and their fabrication methods are described in the following sections.

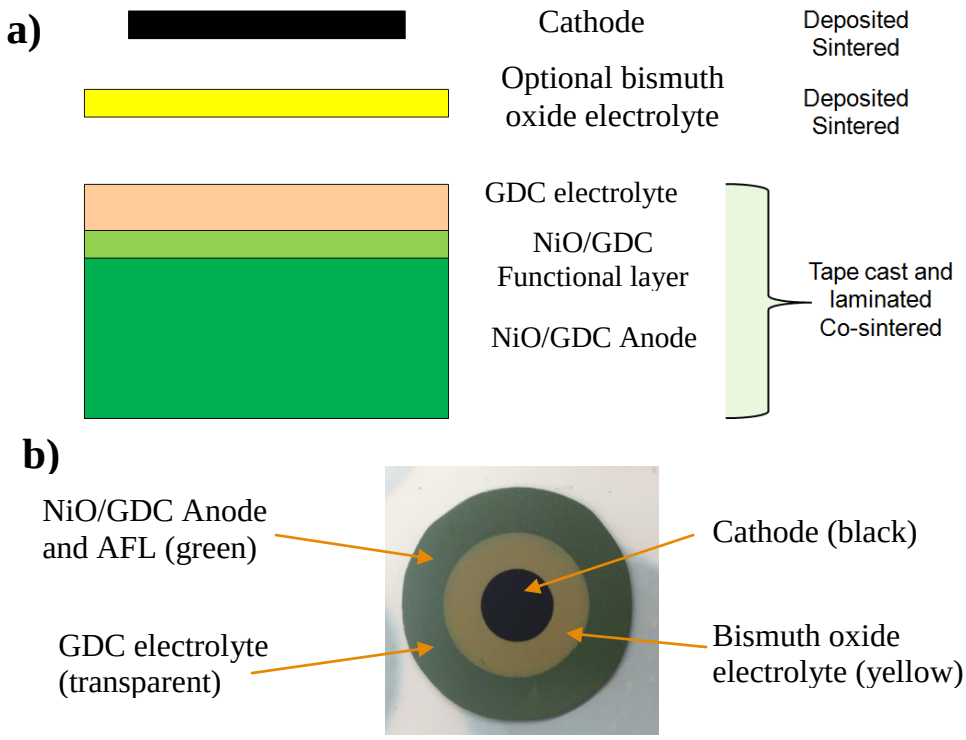

Figure 2.11.1 a) Schematic of the cross-section of a button cell and b) top view image of a button cell prior to testing

2.11.1 Tape Casting and Lamination

Tape casting was used for making the anode, AFL, and GDC electrolyte. For the anode, NiO (Alfa Aesar) and $Ce_{0.9}Gd_{0.1}O_2$ (NexTech Materials) were made into a slurry. For the AFL, the same NiO was used but a finer particle size $Ce_{0.9}Gd_{0.1}O_2$ (JT Baker) was used to make the slurry. The design of the AFL is discussed in more detail in Chapter 3. And for the GDC only slurry, $Ce_{0.9}Gd_{0.1}O_2$ (NexTech Materials) was used without other active material contributions. Solvents toluene and ethanol were placed into a 500 mL HDPE mill with cylindrical 1 cm YSZ milling media with menhaden fish oil (Tape Casting Warehouse) and milled until the fish oil is dissolved for about five minutes. An appropriate ratio of NiO to GDC is added to the mill and milled for 24 hours. Polyvinyl butyral (PVB, Tape Casting Warehouse) was added as a binder. Butyl benzyl phthalate (BBP) was added as a plasticizer. The slurry was

milled another 24 hours. The mill was dumped into a beaker and de-airing was performed under constant stirring in a vacuum-sealed desiccator with excess ethanol to prevent skin formation on the surface of the slurry. The slurry was then poured into a doctor blade set on a mylar film pulled tape caster (Procast) bed set to 120 °C with silicon coated mylar tape substrate (Tape Casting Warehouse). Once the slurry was exhausted, the tape was allowed to dry on the bed at 120 °C.

The three components (anode, AFL, and GDC electrolyte) are laminated in a heated platen Carver press at 180 psi and 180 °F until the lamination is adequately complete. The laminated tapes were then pre-sintered about 900 °C for 2 hours and then fully sintered at 1450 °C for 4 hours. From these sintered bodies, 1" circles are cut out for button cell testing using a diamond scribe and grinding wheel (LECO).

2.11.2 Bismuth Oxide Deposition

2.11.2.1 Drop Coating

For very thin ESB layer deposition, an ESB slurry was synthesized. Solsperse® was dissolved in ethanol in a 125 mL HDPE bottle with 5 mm spherical YSZ milling media. ESB powder was added to the mill along with polyvinyl butyral as a binder and dibutyl phthalate as a plasticizer. This was allowed to mill for extended time greater than 2 weeks. This slurry was then drop coated onto the 1" circles made in the previous section with a Scotch tape mask to keep the droplet from the edges of the cell. The excess from the droplet was simply absorbed with a kim wipe and the remaining was allowed to dry for a few seconds. This was repeated to achieve varying thicknesses of ESB with a maximum of 15 coats, the equivalent of

about 3 μm. The tape was removed and the cell was fired at 800 °C for 2 hours to sinter the ESB.

2.11.2.2 Ink Preparation and Deposition

The desired bismuth oxide powder was added with ethanol in a 125 mL HDPE bottle with 5 mm spherical YSZ milling media and was milled for 24 hours. The solution was poured into a THINKY compatible LDPE container and using 1500 rpm for both mixing and de-airing the ethanol was slowly evaporated in the THINKY mixer (ARE-310). Prior to the full evaporation of the ethanol, a suitable amount of ESL 441 vehicle (Electroscience Labs) was added. The remaining ethanol was evaporated in the THINKY. More ESL 441 was often added to achieve the appropriate viscosity.

The ink was deposited onto the anode, AFL, and GDC 1" button cell substrate with a Scotch tape mask. The thickness of the ink was controlled with the number of layers of tape used to make the mask. A blade was used to deposit a flat and homogenous layer. The tape mask was removed and the ink was allowed to dry at 100 °C for about 3 hours. The cell was then fired at 775 - 830 °C for 2 to 4 hours depending upon the bismuth oxide selected.

2.11.3 Cathode Application

The cathode is synthesized as described in Section 2.9.2. Then two pieces of tape were used as a mask and a 5/16" hole was punched into the tape. The tape was placed onto the GDC electrolyte (stop here if testing single layer GDC only) or already deposited bismuth oxide electrolyte (for bilayer cell testing). The cathode ink was then blade coated over the tape mask. The tape was removed and the cell was

allowed to dry at 80 °C for about 3 hours. The ink was then sintered at 775 °C to 800 °C for 2 hours. A bilayer cell was shown in Figure 2.10.1 after cathode sintering.

2.12 Li-ion Button Cell Fabrication

Cathode materials were synthesized as described in Section 2.1.3.3 and were confirmed for phase purity and chemical composition using XRD and XRF. The active cathode material was then mixed with carbon black and polytetrafluoroethylene in a 85:10:5 weight percent ratio, respectively. This mixture was ground in a mortar and pestle with isopropanol until a dough was formed. The dough was pressed to 0.4 mm thick and 13 mm diameter circles were punched out. An aluminum mesh was spot welded to 2025 steel cans and the cathode circles were pressed into the mesh. Nickel mesh was spot welded onto the lids of the 2025 cans and 13 mm circles were punched from 0.05" thick lithium foil (Alfa Aesar) and pressed into the nickel mesh. The cathode was soaked with 1 molar $LiPF_6$ electrolyte in proportional mixtures of diethyl carbonate, dimethyl carbonate, and ethylene carbonate. Nonwoven glass separator was added and also soaked in the electrolyte and 2025 gaskets were inserted into the can. The lids containing the lithium were crimped onto the cans containing the cathode, electrolyte, gasket, and separator. The crimped cells were cleaned of excess electrolyte with isopropanol and tabs were welded onto the anode and cathode sides for analysis.

2.13 Galvanodynamic Testing of SOFC Button Cell

Button cells were synthesized according to Section 2.10 and loaded onto a homemade reactor. The reactor set-up is shown in Figure 2.13.1. NiO (Alfa Aesar)

was made into a paste using the ESL441 methods described for the bismuth oxide paste in Section 2.10.2. NiO paste was applied to the anode side of the button cell and to Ag mesh located inside a 1" alumina tube (sealed for containing the H_2 environment) and were adhered together. The Ag mesh is connected to two Pt lead wires which in turn are connected to Au lead wires that lead out of the furnace for external measurement connections. Once the NiO paste on the cell and Ag mesh were touching, the cell was held to the end of the alumina tube while a ceramic sealant (Ceramabond) was applied to adhere the cell and prevent leaking of the H_2 from the alumina tube. Once the sealant has dried at room temperature for 2 hours, platinum paste (Heraeus) was painted onto the cathode and a second Ag mesh. The Ag mesh was put into contact with the cathode using the paste. This cathode side Ag is connected to two Pt leads which are in turn connected to Au leads that run down the length of the outside of the alumina tube for external measurement connections.

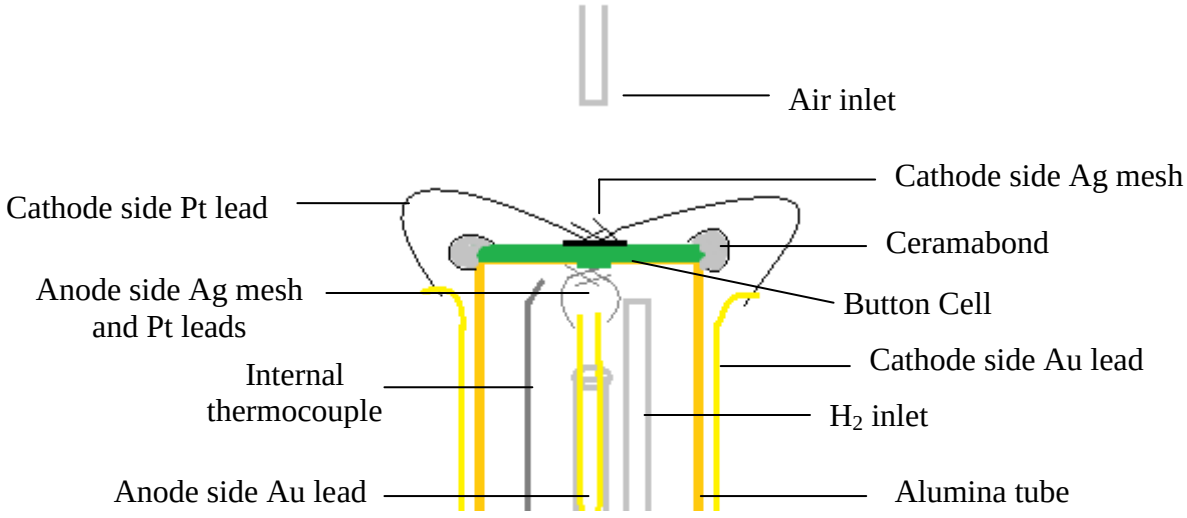

Figure 2.13.1 Schematic of button cell reactor close to the button cell

The entire reactor was placed into a clamshell furnace opposite the air inlet tube. The full set up is shown in Figure 2.13.2. The two anode side Au leads were

connected as working (WE) and sensing (SE) electrodes. The two cathode side Au leads are connected as the counter (CE) and reference (RE) electrodes. The wires were run to a Solartron 1400 cell test system to perform galvanostatic measurements and the temperature at the cell was monitored from the thermocouple fixed to the reactor. The reactor was fired at 94 °C for 2 hours and then 265 °C for 2 hours to cure the sealant. Using Multistat software, the cell open circuit voltage (OCV) was monitored after the 265 °C hold as the air and H_2 is introduced at 5 SCCM up to 650 °C. The cell was held at temperature for 1-2 hours to allow for platinum paste sintering and to fully reduce the anode while the flow of air and H_2 is slowly increased to 200 SCCM. Galvanostatic measurements were then performed at 650 °C and then 600, 550, and 500 °C when applicable. Galvanostatic measurements may be performed up to 100 hours at 650 °C for samples where stability testing may be of interest.

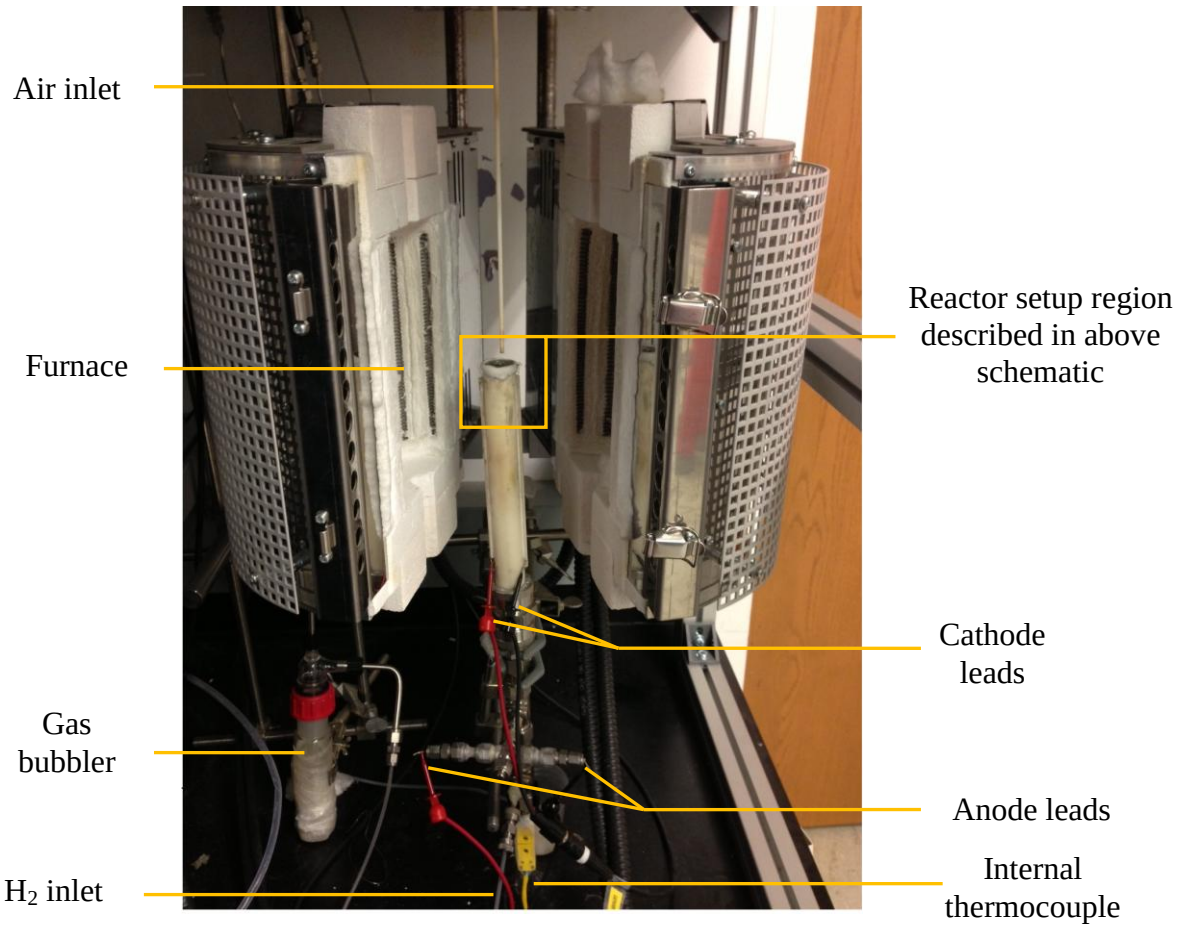

Figure 2.13.2: Actual reactor set up for button cell EIS and IV testing. Anode and cathode leads run back to the Solartron 1400 Cell Test System.

2.14 Electrochemical Impedance Spectroscopy

2.14.1 SOFC Symmetric Cell

After making the symmetric cell as described in Section 2.10.1, the platinum paste is also painted onto two Ag meshes with attached Pt leads. The two meshes are adhered to each side of the symmetric cell and sandwiched in a quartz clamp. The Pt leads were then connected to Au leads on a quartz reactor. The Au leads extend to outside of the reactor for connection with a Solartron 1260 impedance analyzer. A schematic of the reactor set up is shown in Figure 2.14.1 and is adapted from Oh (10). The measurement is taken using Zplot software from 0.1MHz to 0.1Hz with

amplitude of the excitation voltage of 50 mV. Due to the small sample impedances, inductive responses of the leads can add to the impedance of the material we are testing. Impedance of the leads and mesh without a sample was measured and then subtracted from the sample measurements. Treatment of the resulting measurements for electrolyte conductivity and cathode area specific resistance (ASR) is described in Appendix B.

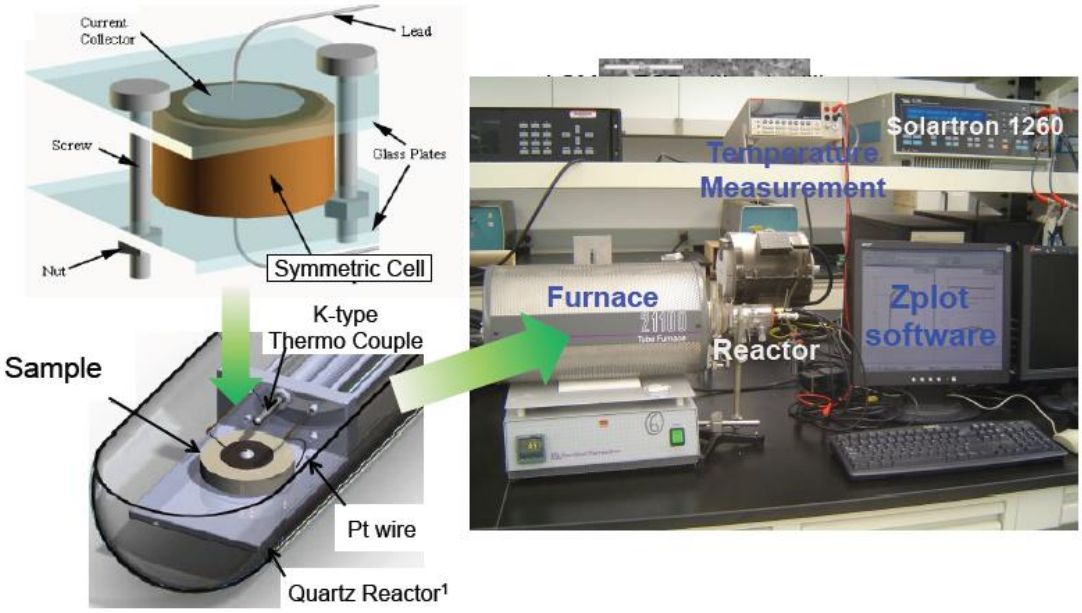

Figure 2.14.3: Symmetric cell testing set up(10)

2.14.2 SOFC Button Cell

The button cell is loaded to the reactor and Solartron 1400 Cell Test System as described in Section 2.13. The Solartron 1400 was used in combination with the Solartron 1470E Frequency Response Analyzer. Using the Multistat software, EIS measurements are performed from 0.1 MHz to 0.1 Hz with an excitation voltage amplitude of 50 mV and the data was observed using the ZView software. EIS measurements were performed 30 seconds apart from the galvanostatic IV measurement. Therefore the measurements were taken at 650, 600, 550, and 500 °C

and for up to 100 hours at 650 °C depending upon the desired information from the sample.

2.15 Oxygen Isotope Exchange

In order to explain ASR results here with previous work on LSM-ESB, oxygen isotope exchange switching experiments were conducted in a two flow lines reactor system on solid state ESB and DWSB materials. Gas is flowed through the powder sample, supported by quartz frit. Furnace temperature was controlled by thermocouple connected to Eurotherm temperature controller. Gas was fed into the reactor from top, leaving from bottom where its composition was sampled with Extrel QMS quadropole mass spectrometer. The monitored masses were 16, 18, 28, 32, 34, 36 and 40, where mass 40 corresponds to Ar gas tracer. Each sample size was adjusted such that the total surface area was 0.1 m^2. After the sample was loaded into the reactor it was pretreated with $^{16}O_2$ for 30 min at 700 °C in order to remove absorbed water and CO_2, following cooling to 50 °C at a rate of 5 °C/min. The pretreatment temperature was chosen 100 °C lower than the calcination temperature in order to prevent microstructural changes to the powder. The reactor was equilibrated for 30 minutes at 50 °C before data collection. Then a $^{16}O_2$+He stream was switched to $^{18}O_2$+He (>97 atom%, Sigma Aldrich) keeping the same O_2 flow rate, and the temperature was ramped to 750 °C at 30 °C/min, while recording the composition. By switching $^{16}O_2$ to labeled $^{18}O_2$ we can monitor the oxygen exchange and its kinetics. Tracking the concentration of different oxygen species (masses 32, 34, 36) we can gain understanding on the abilities of the material to exchange oxygen between the gas phase and the lattice.

2.16 Voltage Cycling of Li-ion Button Cell

After the button cell has been tabbed, the button cell was hooked up to an ARBIN MSTAT 4 battery cycler system controlled by MITS pro software. The cell was charged to the high voltage maximum at either 1 or 2 mA/cm^2 and data collection is performed in 10 mV increments. Typical voltage maxima were 4.5 V, 4.75 V, or 5.0 V depending upon the cell chemistry. 4.5 V was used for chlorinated spinels only and for iron-doped spinels. The 4.75 V maximum was used briefly for the iron-doped spinel but only to verify no iron redox activity is shown at that potential. 5.0 V was used for the nickel-doped cells. For regular discharge, the voltage minimum was set to 3.5 V. For testing the lower voltage performance, the minimum voltage was set to either 2.25 V or 2.0 V. Each measurement was performed until 10 cycles are completed or if the cell begins to fail. Upon successful completion of 10 cycles, additional cycling continues in 10 cycle increments until the cell fails.

Chapter 3: Double Doped Bismuth Oxides

3.1 Introduction

A critical limitation to the commercialization of SOFCs is their high temperature operation. A lower operating temperature would allow for the use of less expensive interconnect materials, reduction of the start-up time, and longer mechanical and chemical stability which could reduce the total system cost. However, lowering the operation temperature of SOFCs is not trivial due to ionic conductivity limitations of electrolyte materials below 700°C. Recent developments in materials research have brought forth new options for ionic conductors with higher conductivity at reduced temperatures. It has been demonstrated that erbium stabilized bismuth oxide (ESB) has one to two orders of magnitude higher ionic conductivity than conventional yttria-stabilized zirconia (YSZ) from 500 °C to 700 °C due to ESB's high oxygen vacancy concentration (1). Furthermore, the ionic conductivity of ESB in this temperature range is also ten times greater than that of gadolinia-doped ceria (GDC) (1).

In order to achieve even higher performance with bismuth oxide, we have taken a double-doping approach to reduce the total doping amount and increase the entropy of the system. Lower total doping reduces the probability of dopant association that can cause conductivity degradation (26, 42, 44). Additionally, the use of two highly polarizable ions improves the mobility of the O^{2-} ion through the material (1, 7, 58). Our previous work uses this rationale for the development of dysprosium tungsten doped bismuth oxide (DWSB) which has an even higher conductivity and stability at lower temperatures as compared to ESB due to lower total doping (1, 44). Others have similarly demonstrated the benefit of adding more than one dopant to the system. Meng et al. also demonstrated that the addition of two dopants from Gd, Nb, Sm, or Pr can stabilize the fluorite structure at lower doping concentration than the single dopant (59). In the case of Pb and Ca dopants, Drache et al. shows that the ternary phase diagram does not allow for formation of the fluorite phase with either Bi_2O_3-CaO or Bi2O3-PbO binary systems, but instead both dopants must be added to reach the fluorite phase region (60).

Based on the success with DWSB, other metals can be substituted into the $Bi_{1-x-y}Dy_xM_yO_{1.5}$ system for enhancing the ionic conductivity of bismuth oxide. Gadolinium is also a highly polarizable ion that has a smaller ionic radius than bismuth. Cerium is another candidate having a larger ionic radius than bismuth, but also has been previously demonstrated by Huang et al. to enhance the structural stability in yttria-doped bismuth oxide at 650°C (61). In this study, the authors synthesize three double doped bismuth oxide materials for measuring ionic conductivity and current-voltage performance: dysprosium tungsten stabilized

bismuth oxide (DWSB), dysprosium gadolinium stabilized bismuth oxide (DGSB), and dysprosium cerium stabilized bismuth oxide (DCSB).

Selected doping levels for ESB and DWSB are 20 mol% Er for ESB and 8 mol% Dy and 4 mol% W for DWSB based on highest conductivity from previous work (26). In this work, DCSB and DGSB are made using three different doping levels and are referred to as 10D5CSB and 10D5GSB, 8D4CSB and 8D4GSB, and 6D3CSB and 6D3GSB where the nomenclature indicates mol% doping of Dy and Gd or Ce. In Chapter 2, the synthesis of the materials is described for three methods used for their synthesis: solid state (SS), coprecipitation (CP), and glycine nitrate combustion process (GNP).

3.2 Results and Discussion

3.2.1 Phase Formation

The results of x-ray diffraction of the solid state and the wet chemical powders synthesized are shown in Figure 3.2.1. ESB formed the desired fluorite phase for both the CP and SS methods as expected from our previous works (23, 30). In the case of DWSB, both wet processing methods yield the formation of the orthorhombic second phase with the cubic phase, however this phase is far less pronounced in the glycine nitrate route. Similarly, a tetragonal phase can be observed in the CP 10D5CSB and SS 6D3CSB while the other three methods and compositions calcined into the desired fluorite phase. It is possible that during the CP synthesis some precursors formed that do not calcine into the appropriate phase if the pH control was not well maintained. In the case of DGSB, all attempted methods yielded the appropriate fluorite phase. Because the SS 6D3GSB achieved a fluorite structure

while the SS 6D3CSB material did not, this indicates with just 9 mol% total doping, the ionic radius of the dopant is critical. In this lattice, Bi^{3+} has an ionic radius of 0.111 nm while Dy^{3+}, Ce^{3+} , and Gd^{3+} have a radius of 0.1025 nm, 0.114 nm, and 0.106 nm, respectively (62). In DCSB and DGSB, the Dy^{3+} dopant is smaller than the Bi^{3+}, which is ideal for stabilization of the structure. The double doping strategy utilizes entropy to reduce the total quantity of dopants, as evidenced by these low doping levels in Figure 3.2.1 while the lowest single doping case (ESB) requires an even smaller ionic radius in Er (0.100 nm) with 20 mol% doping (7, 26, 39, 44). On this lower bound of stability, it is clear that using mixed doping of higher and lower ionic radius in the case of DCSB is not sufficient for stabilizing the lattice and higher doping levels must be used. However for DGSB, because Gd^{3+} has a smaller ionic radius than Ce^{3+} and perhaps also importantly Bi^{3+}, this phase can be stabilized with just 9 mol% total doping.

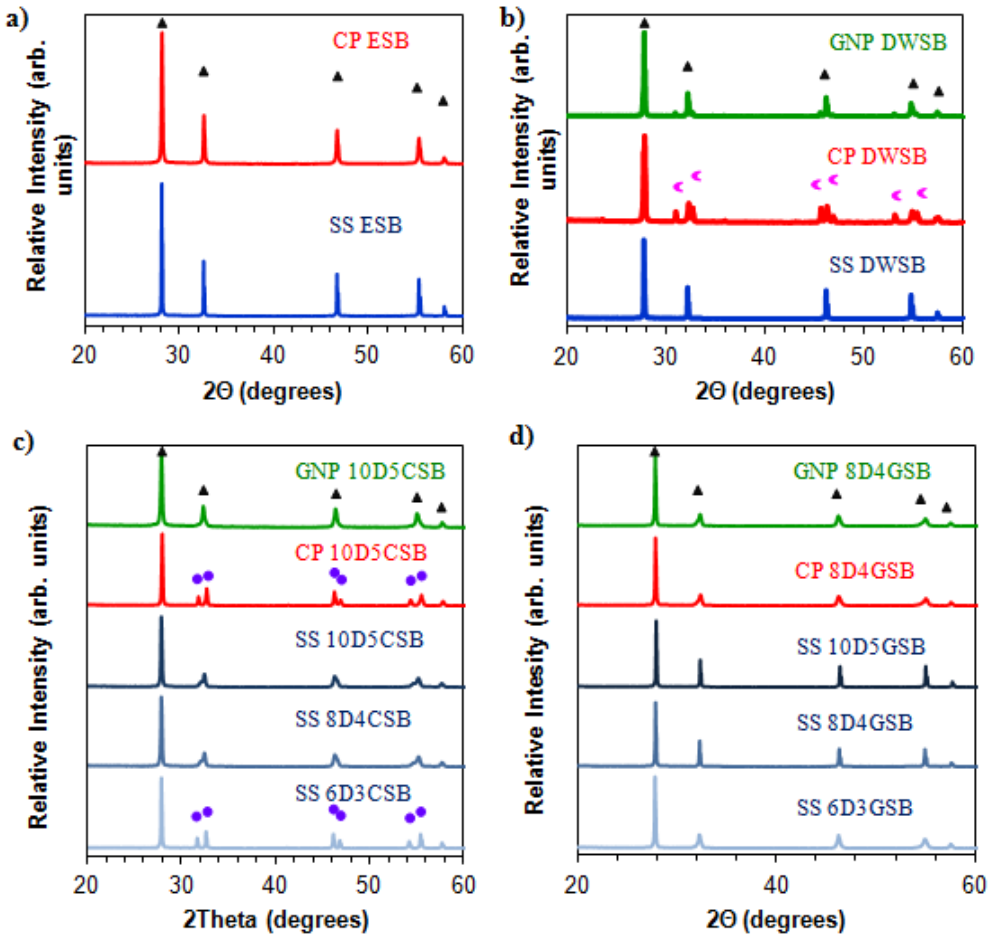

Figure 3.2.1: X-ray diffraction results of synthesized a) ESB, b) DWSB, c) DCSB, and d) DGSB. Triangles (▲) are the desired peaks cubic fluorite phase, crescents (◖) represent orthorhombic peaks, and circles (●) respresent tetragonal peaks.

3.2.2 Electrochemical Impedance Spectroscopy

Ionic conductivity results of powders measured via EIS are shown in Figure 3.2.2a-d with a summary of the best performing cells from each composition in Figure 3.2.2e. In the case of all three dual-dopant chemistries, they each exceed the ionic conductivity of ESB above 450°C, demonstrating the benefit of the strategy for lowering the total doping needed for stability through increased entropy. The only exclusion is the performance of GNP 10D5CSB. This pellet was not able to sinter to greater than 95% theoretical density as required of the other samples. In fact this

composition/synthesis method combination remained openly porous with less than 90% theoretical density over several sintering attempts. The material could have been over sintered, but lower sintering temperatures were not attempted due to the requirements for firing current collectors and cathodes for full cell testing. Perhaps the most promising of the synthesized chemistries is DGSB which shows the highest conductivity but only for the solid state synthesis method. When using a nanoscale synthesis, DGSB has similar performance to DCSB and DWSB, demonstrating little correlation among second dopant options thus far based on this result alone. One phenomena that is interesting is how the different synthesis methods can change the location of the change in slope, which is correlated to activation energy. We have previously studied ESB and determined the change in activation energy at 600 °C can be attributed to the order/disorder transition of the material (38, 43, 63-64). In the disordered state at higher temperatures, the oxygen vacancies can occupy any of the 8 lattice sites and can move from one site to the other very easily, yielding an effective vacancy occupancy of 1/4 at each lattice site. However below the transition, the oxygen vacancies order along the <111> direction, limiting their mobility and therefore increasing the activation energy required for conductivity. In the double-doped bismuth oxides, this transition temperature has shifted down to 550 °C or even 500 °C, demonstrating their potential for incorporation into lower operation temperature SOFCs in the future.

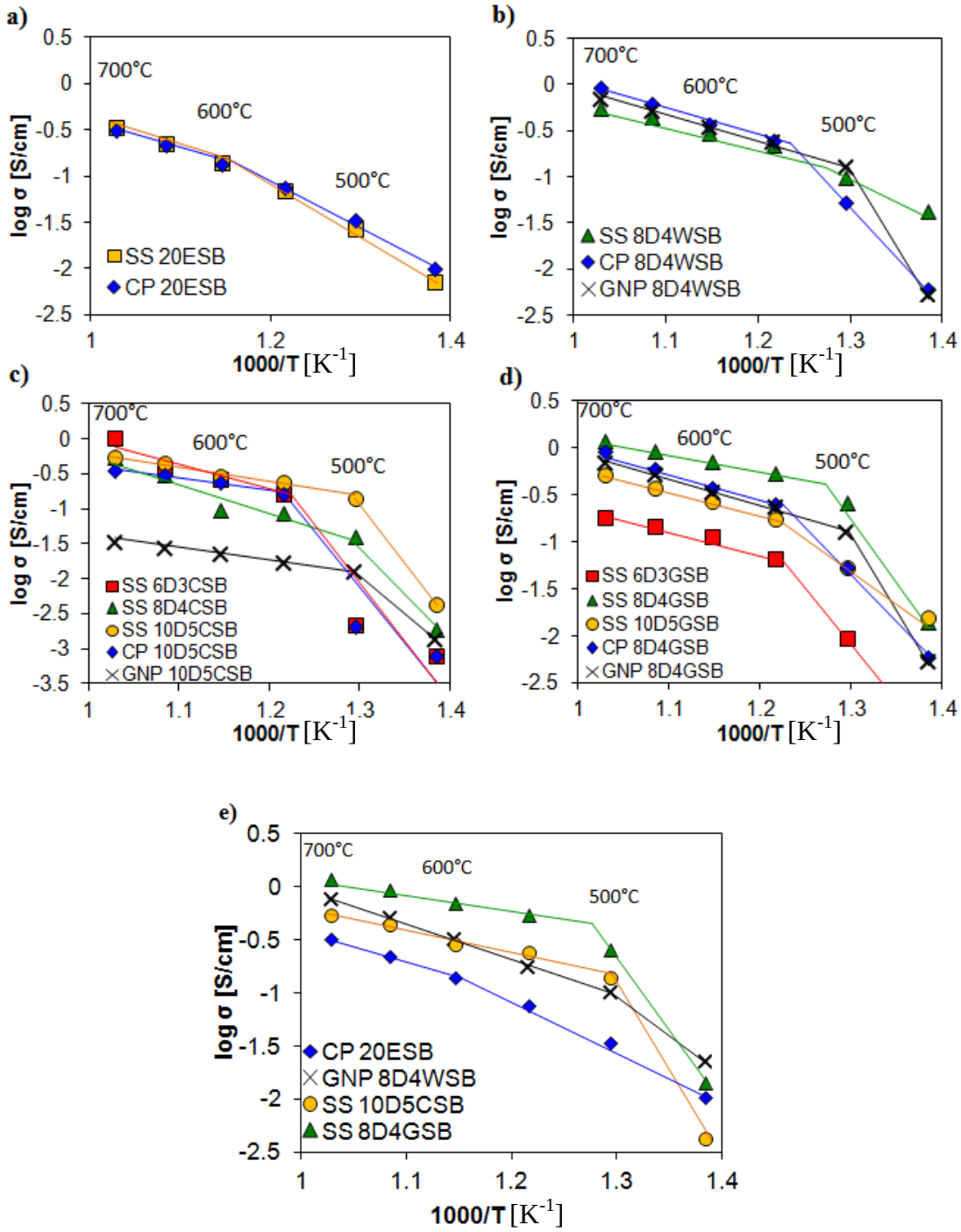

Figure 3.2.2: Arrhenius plots of symmetric cell conductivity for all synthesis methods for a) ESB, b) DWSB, c) DCSB, and d) DGSB and e) a summary of the highest performances. SS indicates solid state, CP indicates coprecipitation synthesis, and GNP indicates glycine nitrate process synthesis and lines are drawn as a guide for observing activation energy changes.

3.2.3 Layer Formation

The best performing materials from each composition demonstrated in Figure 3.2.2e were selected for full cell incorporation to demonstrate the benefit of a higher conductivity electrolyte material. Materials must be prepared into an ink and sintered into a dense layer. SEM images taken after testing (Figure 3.2.3a-d) confirm the formation of a dense layer on top of the existing 18.6 μm GDC electrolyte to form the bilayer structure required for testing. Bismuth oxide layer thicknesses varied from 2.54 to 3.49 μm. The variance is due to the simple blade coating method and differences in the vicosities of the inks, while the GDC layer thickness is controlled on these substrates as they are cut from the same larger substrate, eliminating batch variation.

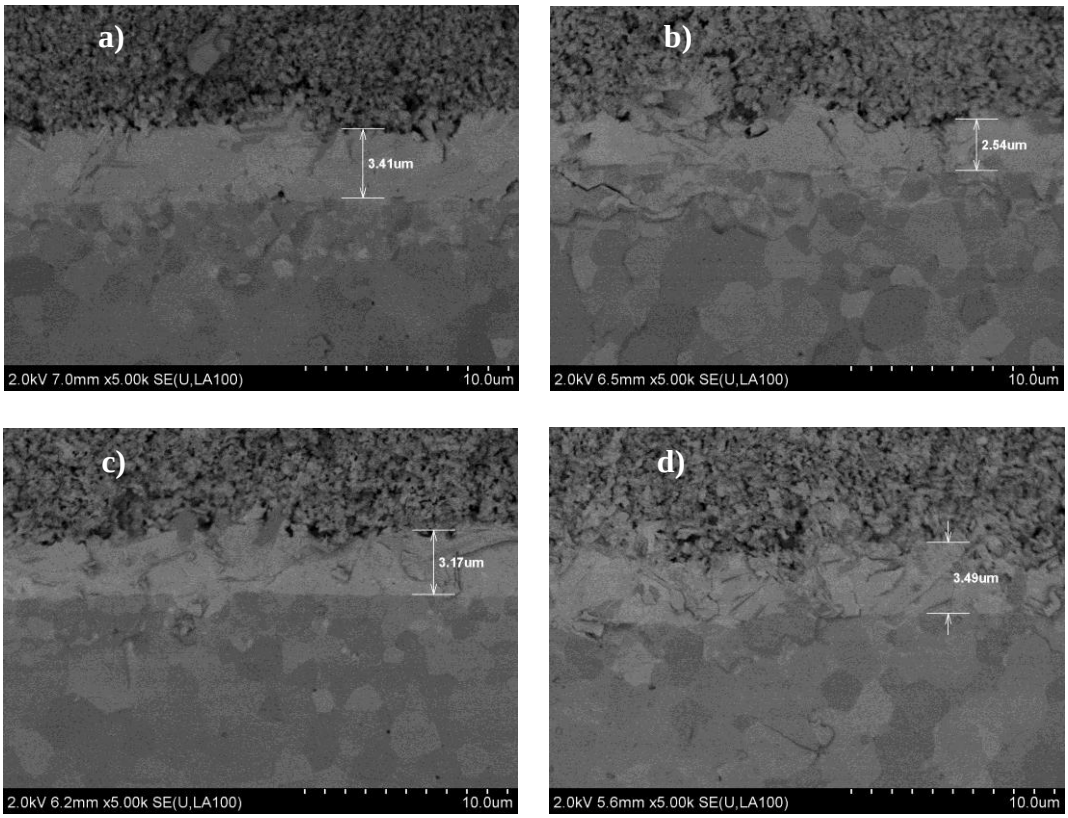

Figure 3.2.3: Back scattered SEM micrographs of bilayer electrolytes a) ESB , b) DWSB, c) DCSB, and d) DGSB on GDC electrolyte (bottom of images) with a porous LSMESB cathode on top. Images taken after testing.

3.2.4 Button Cell Performance

A set of results from IV and EIS measurements of the four chemistries with the same LSM-ESB cathode are shown in Figures 3.2.4a and 3.2.4b, respectively. In Figure 3.2.4a, the maximum power density (MPD) reaches 0.95 W/cm^2 for DGSB, 0.91 W/cm^2 for DWSB, and 0.77 W/cm^2 for DCSB while ESB is able to achieve 0.60 W/cm^2. Our group has previously demonstrated the benefit of the bilayer structure with ESB (1). Bare GDC single layer electrolyte results are not shown in order to maintain the same cathode for this study, as an LSM-ESB cathode would not be an ideal selection for GDC (MPD for GDC with an LSM-ESB cathode on these same

substrates is just 0.42 W/cm^2). But the incorporation of these higher conductivity materials allows us to achieve an even higher power density when comparing among themselves. In the nyquist plots in Figure 3.2.4b, one can see that the total resistance (low frequency or right-most intercept) is highest in the ESB case. Conversely, the DGSB has the lowest total resistance and shares a low ohmic resistance (high frequency or left-most intercept) with DWSB. This is expected as both DWSB and DGSB have the two highest ionic conductivies at 650 °C of the four materials studied. The correlation between the total ASR from these measurements with the conductivity determined in symmetric cell testing is shown in Figure 3.2.5. One might expect that DGSB should have the lowest ohmic resistance due to its symmetric cell performance, and we expect the DWSB data point to be higher in Figure 3.2.5. However while the cells were fabricated for approximately the same bismuth oxide layer thickness, there were slight inhomogeneities in this layer as shown in the SEM images. Because the DWSB electrolyte layer (2.54 μm thick) and the DGSB layer (3.49 μm thick) are on opposite bounds of the layer thicknesses, this can account for the fact that the DWSB resistance was lower than expected as it exhibited the thinnest layer of the four measured cells on identical GDC substrates.

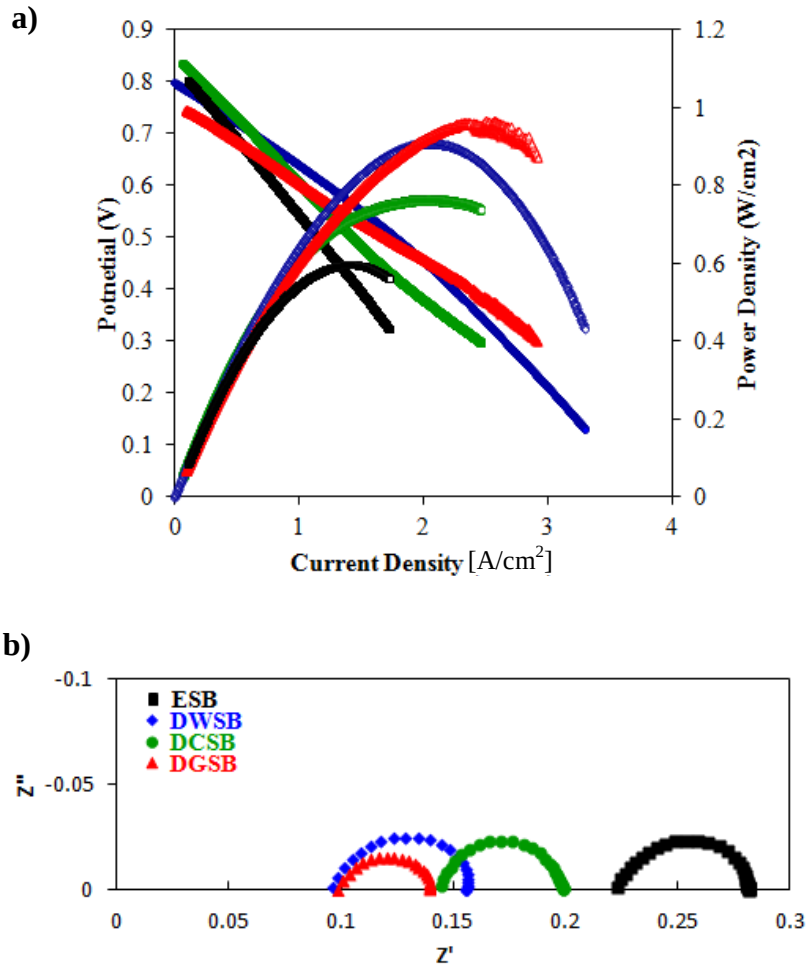

Figure 3.2.4: a) IV curves with power density and b) Nyquist plots for bilayer cells of NiO-GDC anode/ NiO-GDC functional layer/ GDC electrolyte/ ESB, DWSB, DCSB, or DGSB electrolyte/ LSM-ESB cathode at 650°C.

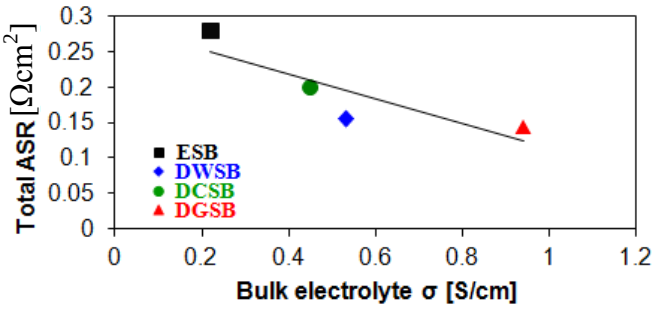

Figure 3.2.5: Correlation between the total ASR from the button cell testing and the bulk electrolyte conductivity as determined by symmetric cell testing at 650 °C.

3.2.5 Button Cell ASR Degradation

A set of results from long term EIS measurements is shown in Figure 3.2.6 as the initial ASR over the ASR at time *t* to demonstrate the relative change in both the ohmic contribution to the ASR and total ASR. DCSB exhibits the fastest degradation in ASR which may be attributed back to the limited stability of the lattice due to the two dopants having one higher and one lower ionic radius than Bi^{3+}. ESB is known to have degradation over extended time but was included for completeness. Both of the higher performing materials DGSB and DWSB also have the best stability with both ohmic ASRs remaining constant from 10 to 65 hours and the total ASR for DGSB remaining constant from 20 up to 100 hours. These results in combination with the high performance make for promising SOFC bilayer electrolytes.

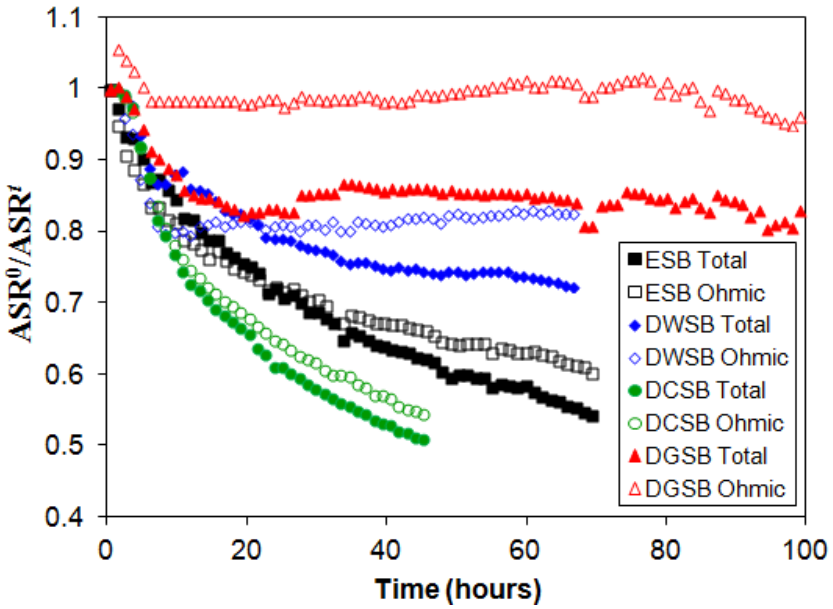

Figure 3.2.6: Initial ASR over ASR at time *t*, showing the degradation of the total and ohmic contribution to the ASR over time of button cells at 650 °C.

3.3 Conclusions

Higher conductivity bismuth oxide materials have been demonstrated utilizing a double-doping strategy for lowering the total dopant concentration. All three materials, DWSB, DGSB, and DCSB, have shown an improvement in conductivity over the more commonly studied ESB. Furthermore, DWSB, DCSB, and DGSB incorporated into full button cells have demonstrated this improvement and its impact on cell performance by reducing the slope of the IV curve to achieve a higher power density with lower total ASR than ESB. In order to further reduce the interfacial polarization, these materials will be incorporated into a cathode material that will be specifically tuned for the electrolyte it interfaces with. With further work, DGSB and DWSB have the potential for being excellent electrolyte materials. In this study, DGSB achieved the highest conductivity of 0.94 S/cm which led to the highest MPD of 0.95 W/cm^2 at 650 °C. To our knowledge this conductivity is the highest reported solid oxide electrolyte conductivity. Additionally, DGSB had the most stable ASR up to 100 hours. DWSB also had figures of merit with a conductivity of 0.53 S/cm and MPD of 0.91 W/cm^2 at 650 °C with good ASR stability. While DCSB did not achieve better stability over ESB, the double doping strategy was successful for improving the conductivity over ESB and resulted in an improvement in full cell performance. With the combined demonstration of improved conductivity in both testing configurations coupled with stability implications and a reduction in transition temperature to 500 °C, DGSB and DWSB are excellent candidates for future SOFC applications.

Chapter 4: A Study of ESB and GDC Layer Thicknesses in Bilayer SOFCs and the Influence on Open Circuit Voltage

4.1 Introduction

4.1.1 General Introduction

Solid oxide fuel cells have been studied recently for their suitability as gateway solutions for sustainable energy generation due to their high performance and fuel flexibility. However the limiting factor continues to be the high operating temperatures needed for conventional materials like yttria-stabilized zirconia (YSZ). By selecting materials with higher conductivity at lower temperatures (≤ 650 °C) we can bring down the operating temperatures of SOFCs for an improved performance at lower temperatures.

In order to ultimately improve the performance of SOFCs, one must optimize the open circuit voltage (OCV) and minimize the total area-specific resistance. Our group has previously developed a bilayer ESB/GDC electrolyte, shown schematically in Figure 4.1.1, that demonstrates improved OCV and conductivity over the GDC only electrolyte (2, 65-67). GDC has a low transference number relative to ESB, whose transference number is approximately equal to unity (0.99 at 650 °C at 1 atm) (1, 68-69). By incorporating the ESB layer, one can effectively block the leakage current as a result of the mixed ionic-electronic conducting properties of the GDC at

low P_{O2}, which exists in the reducing fuel atmosphere. Additionally this provides the advantage of utilizing a material with an order of magnitude improvement in conductivity. However while ESB seemingly has superior properties, it cannot be used as a single layer electrolyte due to its instability in low P_{O2} and will reduce to bismuth metal. Though future fuel solutions may be able to offer high enough P_{O2} particularly at lower temperatures, at present the GDC layer is necessary for preventing the formation of the metal.

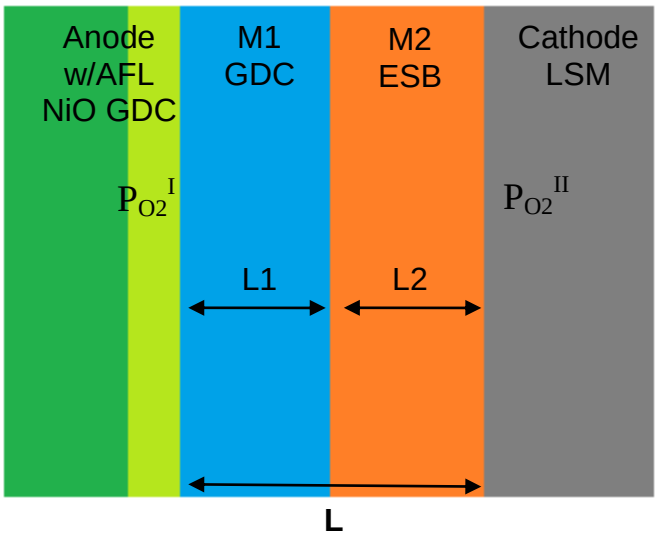

Figure 4.1.1: Schematic of an ESB/GDC bilayer SOFC

4.1.2 Theoretical open circuit voltage dependence

Other groups have studied the optimal L1 and L2 through thermodynamic calculations of bilayer SOFCs, but most focus on zirconium-based oxides like Y-stabilized zirconia (YSZ) in addition to doped-cerias, like Sm-doped ceria (SDC) and GDC (70-74). However we are not interested in zirconia-based oxides due to their even lower conductivity than GDC. But Shen et al.'s model has proven sound when compared with experimental results and could be applicable to other material systems. The OCV is determined thermodynamically from the treatment of the

Nernst equation discussed in Appendix A and is dependent upon the ratio of the oxygen partial pressure between the two electrodes:

$$E = \frac{RT}{2F} \ln \left(\frac{(P_{O2})^{1/2}_{cathode}}{(P_{O2})^{1/2}_{anode}} \right) \quad \textit{(Eq. 4.1)}$$

where R is the universal gas constant, F is Faraday's constant, and T is temperature. The total thickness (L = L1+L2) of the electrolyte has an impact on OCV as the integration of the current density from 0 to L is dependent upon the oxygen partial pressure from 0 to L. From this, Shen et al. calculate the OCV dependence on L as follows (71):

$$V_{OC} = V_{th} - \frac{j_{O^{2-}}}{\sigma^{eq}_{O^{2-}}} L \quad \textit{(Eq. 4.2)}$$

where V_{OC} is the open circuit voltage, V_{th} is the theoretical potential, j_{O2-} is the ionic current density, and σ_{O2-}^{eq} is the equivalent ionic conductivity. Experimentally, varying total thicknesses of the electrolyte is therefore expected to show a clear positive linear correlation between the OCV and the total thickness.

The ratio of the two electrolyte thicknesses is also an important consideration for its impact on the OCV. Their relationship is nonlinear and complex and is expressed as (70):

$$\exp\left[\frac{-q}{k_B T}(V_{th} - V_{OC})(1-\kappa)\right]\left[(P^{I}_{O2})^{-1/4} + \frac{\sigma^{1}_{O2-}}{\sigma^{1,0}_{e}}\right] - \exp\left[\frac{q}{k_B T}(V_{th} - V_{OC})\kappa\right]\left[(P^{II}_{O2})^{-1/4} + \frac{\sigma^{2}_{O2-}}{\sigma^{2,0}_{e}}\right] = \frac{\sigma^{1}_{O2-}}{\sigma^{1,0}_{e}} - \frac{\sigma^{2}_{O2-}}{\sigma^{2,0}_{e}} \quad \textit{(Eq. 4.3)}$$

where $\kappa = 1/(r_s(\sigma^2_{O2-}/\sigma^1_{O2-}) + 1)$ and r_s is the ratio of the anode side electrolyte thickness to cathode side electrolyte thickness, or L1/L2 (equivalent to

1/(ESB/GDC) ratio for our purposes). q is the charge, k_B is Boltzmann's constant, T is the temperature, σ_{O2-}^{1} and σ_{O2-}^{2} are the ionic conductivity of the anode-side layer and cathode-side layer (M1 and M2 in Figure 1) and $\sigma_e^{1,0}$ and $\sigma_e^{2,0}$ is the temperature-dependant electronic conductivity coefficient that is independent of oxygen partial pressure for M1 and M2, respectively. In this work we will compare the expected OCV to experimental results with varying ESB/GDC ratios in addition to confirming a linear correlation between OCV and total thickness.

4.2 Results and Discussion

4.2.1 Microstructural Observations

After observing the cells under the SEM, the thicknesses of each layer was used for analysis and is presented in the list of sample results shown in Table 4.2.1. The layers varied from 8.33 μm total thickness to 49.63 μm and ESB/GDC ratios of close to 0 (no ESB layer added) to 1.76. First, it was important that the layers were densified completely to prevent any leaking across the electrolyte. A collection of representative SEM images are presented in Figure 4.2.1 showing the ability to synthesize dense layers and control the layer thicknesses. These images are taken in back-scattering mode such that the ESB is noticeably lighter than the GDC layer. On the top of the images is the LSMESB cathode, then the ESB layer (if present), then the GDC layer, and the AFL and anode is at the bottom of the images. When looking at Figure 4.2.1a specifically, one may notice some lighter regions at the interface between the GDC and the LSMESB. In Figure 4.2.1i, there is a close-up view of the interface between the LSMESB and the GDC layer showing the ESB has wetability

on the surface and formed a ~100 nm layer. This was observed previously on YSZ (30) and 100 nm is considered for L2 in the cases where there was no ESB deposited onto the sample.

Table 4.2.1: Summary of sample parameters and measured open circuit voltage at 650 °C, 600 °C, and 550 °C. CP and SS are coprecipitated and solid state ESB made in house. TT and Sig represent ESB powders made by Trans Tech Products and Sigma Aldrich, respectively.

Sample	GDC Thickness L1 (µm)	ESB Thickness L2 (µm)	ESB/GDC $1/r_s$	Total Thickness (µm)	OCV 650 °C (V)	OCV 600 °C (V)	OCV 550 °C (V)	ESB Origin
1	6.15	2.18	0.35	8.33	0.776	0.831	0.883	CP
2	6.70	4.37	0.65	11.07	0.762	0.831	0.923	Sig
3	4.96	8.73	1.76	13.69	0.767	0.737	0.785	TT
4	12.40	6.00	0.48	18.40	0.842	0.898	0.945	SS
5	12.80	5.50	0.43	18.30	0.827	0.885	0.933	SS
6	11.70	7.34	0.63	19.04	0.844	0.906	0.961	SS
7	12.00	12.90	1.08	24.90	0.809	0.843	0.87	SS
8	19.10	0.10	0.01	19.20	0.792			
9	20.10	0.10	0.00	20.20	0.8			
10	20.50	0.10	0.00	20.60	0.8	0.83	0.863	
11	21.80	0.10	0.00	21.90	0.761	0.793	0.817	
12	23.00	0.10	0.00	23.10	0.814	0.853	0.889	
13	18.00	2.08	0.12	20.08	0.803			CP
14	20.20	2.51	0.12	22.71	0.818	0.85	0.865	TT
15	26.10	3.27	0.13	29.37	0.842	0.882	0.916	Sig
16	18.90	3.41	0.18	22.31	0.82	0.855		SS
17	20.80	3.77	0.18	24.57	0.824			SS
18	16.80	3.81	0.23	20.61	0.8			SS
19	19.00	3.87	0.20	22.87	0.823			CP
20	21.60	4.96	0.23	26.56	0.815	0.852	0.889	TT
21	20.40	7.34	0.36	27.74	0.809	0.833	0.867	CP
22	21.20	8.93	0.42	30.13	0.846	0.873		SS
23	22.90	9.92	0.43	32.82	0.845	0.887	0.919	Sig
24	23.10	10.00	0.43	33.10	0.835	0.88	0.913	Sig
25	23.60	12.80	0.54	36.40	0.84	0.886	0.926	Sig
26	20.20	13.70	0.68	33.90	0.826	0.865	0.891	CP
27	22.20	14.70	0.66	36.90	0.854	0.911	0.955	Sig
28	20.30	24.10	1.19	44.40	0.861	0.914	0.956	Sig
29	42.90	6.35	0.15	49.25	0.883	0.912		SS
30	41.30	8.33	0.20	49.63	0.889	0.937	0.977	SS

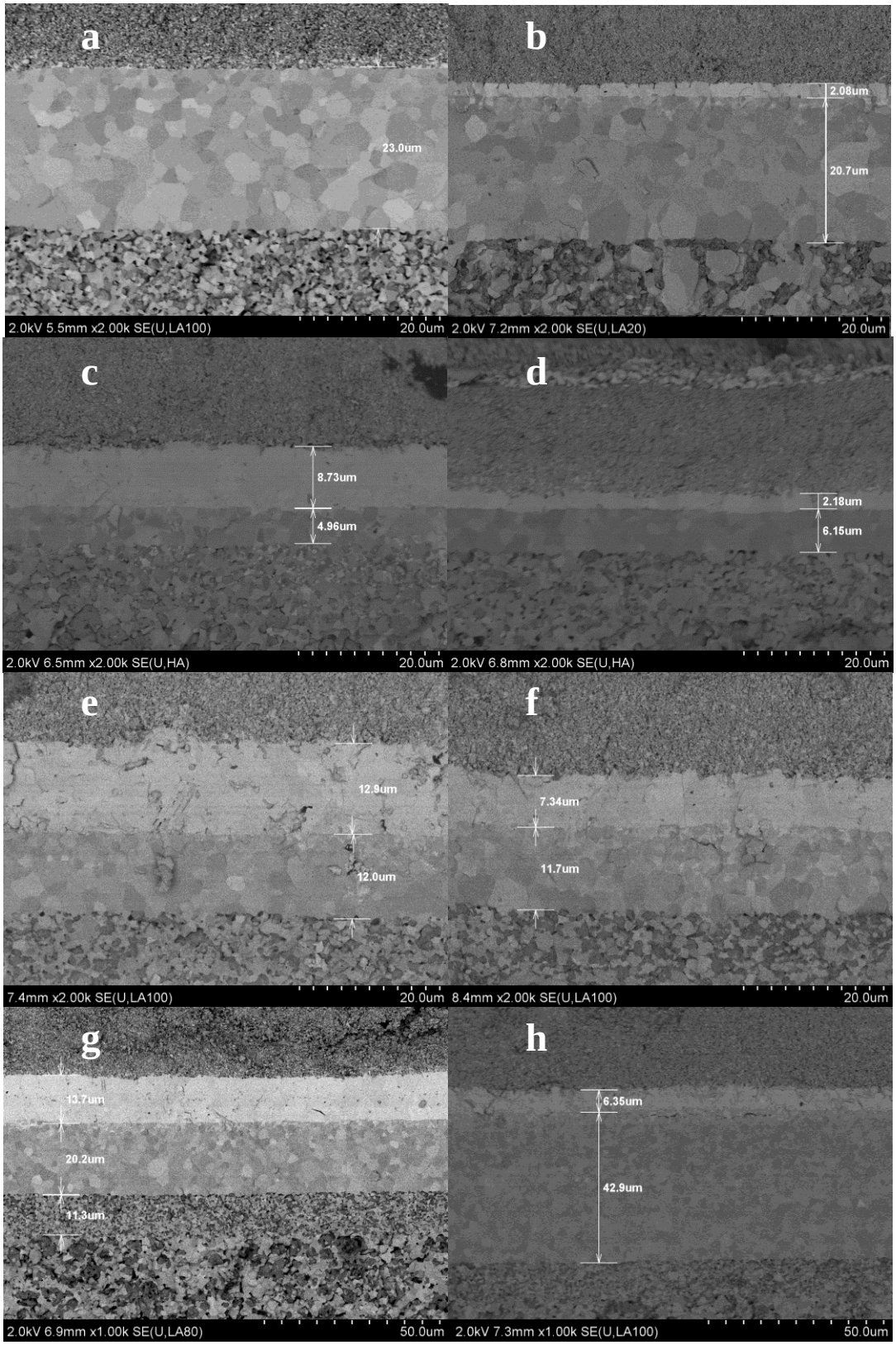

Figure 4.2.1: SEM images of samples 12 (a), 13, (b), 3 (c), 1 (d), 7 (e), 6 (f), 27 (g), and 29 (h). Figure 4.2.1i (high magnification of sample 12) is continued on the next page.

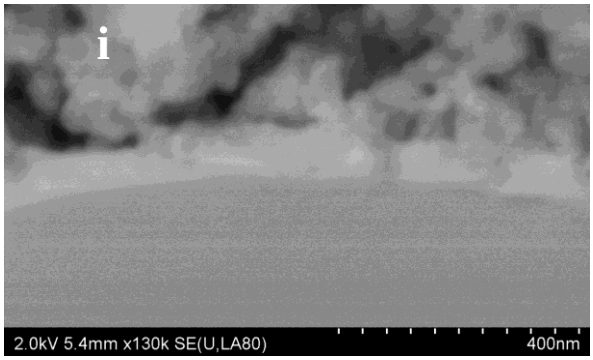

Figure 4.2.1 (continued): High magnification of sample 12 (i).

4.2.2 Total Thickness and OCV

In order to visualize the OCV results, a scatter plot was created for 650 °C, 600 °C, and 550 °C against the total thickness and is displayed in Figure 4.2.2. At 650 °C, data from our previous work is included to demonstrate that it fits well with the samples presented here (1). From inspection, there is a positive linear relationship between the OCV and the total thickness as expected from Eq. 4.2. However, the relationship is not necessarily obvious due to variability in the data. In order to confirm the correlation is real, for sample size *n*, the Pearson product moment correlation coefficient, *r*, is calculated with our data set and the four additional points from Wachsman et al. (1, 75):

$$r = \frac{n\sum LV_{OC} - (\sum L)(\sum V_{OC})}{\sqrt{\left[n\sum L^2 - (\sum L)^2\right]\left[n\sum V_{OC}^2 - (\sum V_{OC})^2\right]}} \qquad \textit{(Eq. 4.4)}$$

r is 0.84, 0.58, and 0.57 for 650 °C, 600 °C, and 550 °C, respectively. The Pearson coefficient is positive, demonstrating the positive correlation expected. In general, a higher value shows a stronger correlation of the data, meaning the 650 °C data had a the strongest correlation and least scatter of the three. This was likely due to greater sample size for the OCV at 650 °C. To ensure that *r* is high enough, the coefficient is

tested against the mutually exclusive hypothesis such that a probability that any random set of data of a particular sample size would show this correlation by chance can be determined. When compared against critical values of *r* for the appropriate sample size, each value in fact has a less than 1% probability of this correlation being by chance. The parameters for this test are shown in Table 4.2.2.

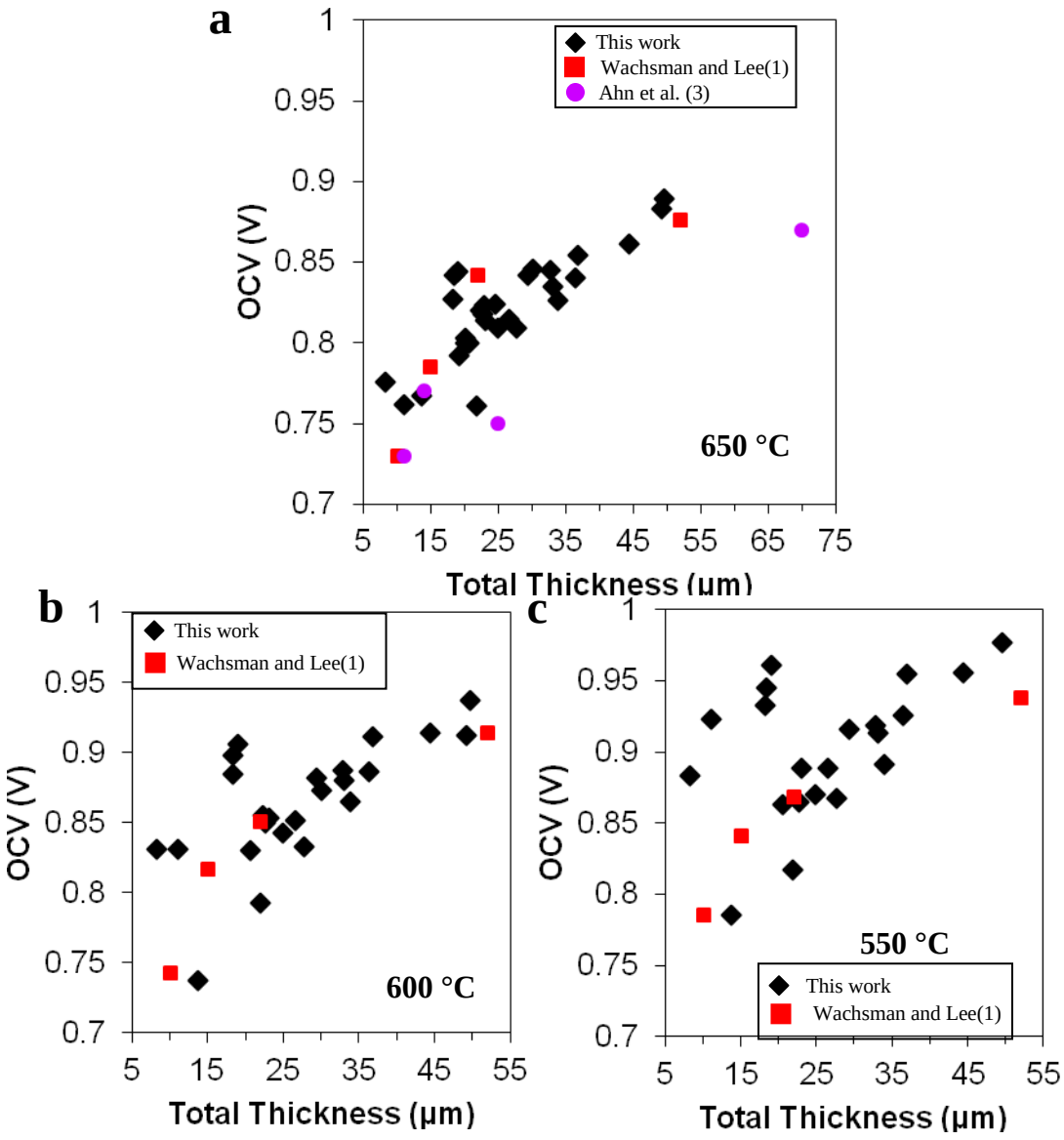

Figure 4.2.2: Summary of OCV results versus total electrolyte thickness at 650 °C (a), 600 °C (b), and 550 °C (c) including previous work from Wachsman and Lee and Ahn et al. (1, 3).

Table 4.2.2: Summary of statistical values for correlation between total thickness and OCV

Temperature (°C)	n	Σ L (μm)	Σ V_{OC} (V)	Σ V_{OC} * L (Vμm)	Σ L^2 ($μm^2$)	Σ V_{OC}^2 (V^2)	r	r for 0.01 Significance
650	34	881.2	27.9	732.9	26847	22.9	0.84	0.44
600	29	753.7	24.1	659.1	24115	20.8	0.57	0.47
550	26	652.0	22.4	592.0	20284	20.1	0.54	0.50

In order to see if this effect of total thickness remains for much smaller aspect ratios of ESB/doped cerias, the results from electrolyte supported bilayer cells with Sm-doped ceria (SDC) on the order of mm from our previous work by Park et al. was added to the 650 °C data in Figure 4.2.3 (2). As one can see, the scatter is great in the added data set with respect to total thickness. This implies that for such extreme aspect ratios, there must be some other critical phenomena governing the open circuit voltage. Park et al. already demonstrated that this scatter does have a correlation with the ESB/SDC ratio, and is shown in Figure 4.2.4 that with more ESB, the open circuit voltage is enhanced.

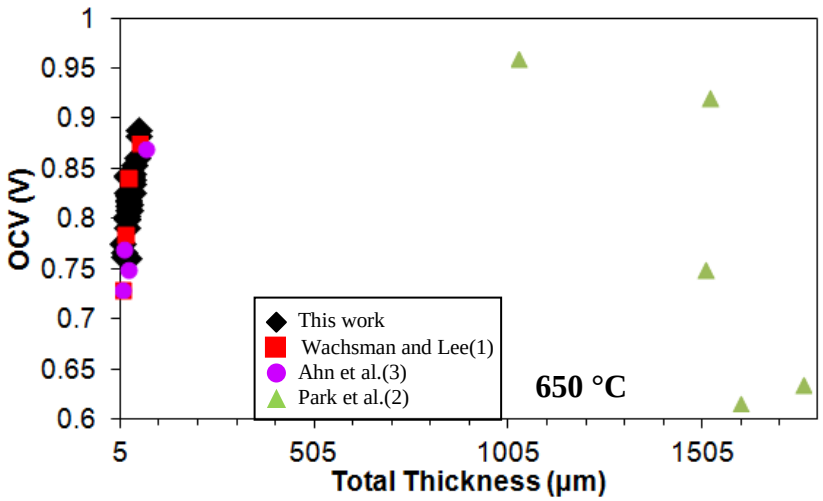

Figure 4.2.3: Addition of Park et al. previous work to Figure 4.2.2a (1-3)

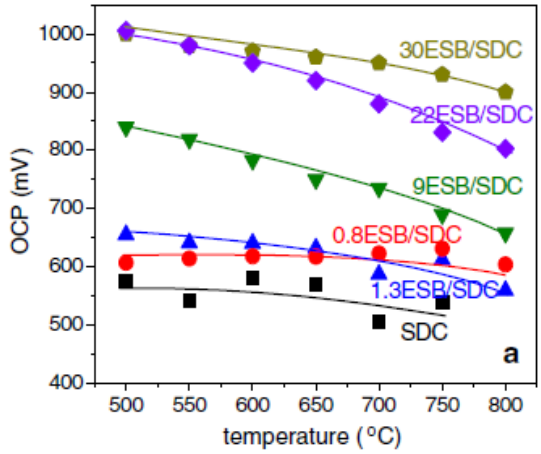

Figure 4.2.4: Open circuit potential of SDC and ESB/SDC electrolytes (2)

In order to determine if either of the two components of the bilayer might have an impact on the OCV through the total thickness, the OCV is plotted against both GDC thickness and ESB thickness at 650 °C in Figure 4.2.5. While both exhibit a positive correlation that is statistically significant according to the determination of the Pearson correlation coefficient in Table 4.2.3, this correlation is much stronger in the case of GDC ($r = 0.70$) than ESB ($r = 0.53$). This indicates that at the thicknesses in this sample set, the open circuit voltage dependence on electrolyte thickness is more strongly linked to the GDC thickness, but both are important and do have an impact.

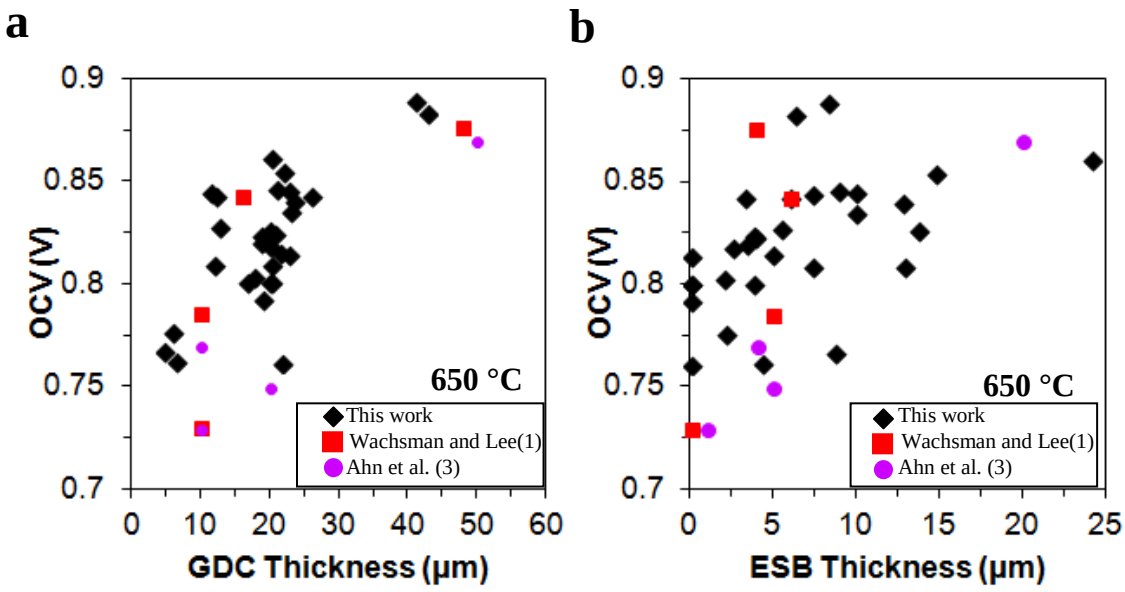

Figure 4.2.5: Open circuit voltage plotted against a) GDC thickness and b) ESB thickness at 650 °C including previous work (1, 3)

Table 4.2.3: Summary of statistical values for correlation between GDC and ESB thickness and OCV at 650 °C for this work and previous work (1, 3)

Layer	n	Σ L (µm)	Σ V_{OC} (V)	Σ V_{OC} * L (Vµm)	Σ L^2 ($µm^2$)	Σ V_{OC}^2 (V^2)	r	r for 0.01 Significance
GDC	38	764.7	31.0	634.3	19412	25.3	0.70	0.43
ESB	38	236.5	31.0	197.1	2597	25.3	0.53	0.43

4.2.3 OCV Dependence on ESB/GDC Ratio

In addition to the total thickness and its impact on OCV, the ratio of the ESB layer thickness to GDC layer thickness plays a role is the expected open circuit voltage as described in Eq. 4.3. Our group previously developed the bilayer structure as a way to mitigate the partial electronic conductivity of the GDC and the decomposition of ESB at low P_{O2}. However the ideal ratio has not yet been determined. In order to determine the expected outcome for our result, the V_{th}-V_{oc} was determined by selecting or calculating literature values of σ_{O2}^{GDC}, σ_{O2}^{ESB}, $\sigma_e^{GDC,0}$, and $\sigma_e^{ESB,0}$. The values for σ_{O2}^{GDC} and σ_{O2}^{ESB} can be selected directly from our previous work (1). The determination of the temperature dependent electronic

conductivity coefficient required calculation from literature values. For application in the equations used here originally from Shen et al., this coefficient is included as such (70-71, 74):

$$\sigma_e = \sigma_e^0 P_{O2}^{-1/4}$$

For GDC, the electronic conductivity is reported by Steele as (76):

$$\sigma T = 3.456 \times 10^9 \exp(-2.475/kT) P_{O2}^{-1/4} \qquad \textit{(Eq. 4.6)}$$

The value for $\sigma_e^{GDC,0}$ can be calculated for each temperature. According to the definition of $\sigma_e^{ESB,0}$, the value is able to be determined from the ionic transference number at standard pressure reported at each temperature for 20 at% ESB by Verkerk et al. determined to be 0.99 for each temperature (69). These values as well as the oxygen partial pressure at the anode and cathode are included in Table 4.2.4. From these, a relationship between the ESB/GDC ratio ($1/r_s$) and the difference between the OCV and theoretical voltage at each temperature can be obtained using Eq. 4.3 and is displayed in Figure 4.2.6. The inset focuses on the result for the ESB/GDC ratio less than 2, which is applicable to the data set in this work.

Table 4.2.4: Electrochemical parameters for GDC and ESB and anode and cathode oxygen partial pressures

Temperature (°C)	$\sigma_{O2\text{-}}^{GDC}$ (S cm^{-1})	$\sigma_e^{GDC,0}$ (S cm^{-1})	$\sigma_{O2\text{-}}^{ESB}$ (S cm^{-1})	$\sigma_e^{ESB,0}$ (S cm^{-1})	P_{O2}^{I} (atm)	P_{O2}^{II} (atm)
650	0.025	2.19×10^{-6}	0.223	2.25×10^{-3}	5.10×10^{-26}	0.21
600	0.016	5.43×10^{-7}	0.126	1.27×10^{-3}	1.27×10^{-27}	0.21
550	0.001	1.16×10^{-7}	0.061	6.15×10^{-4}	2.04×10^{-29}	0.21

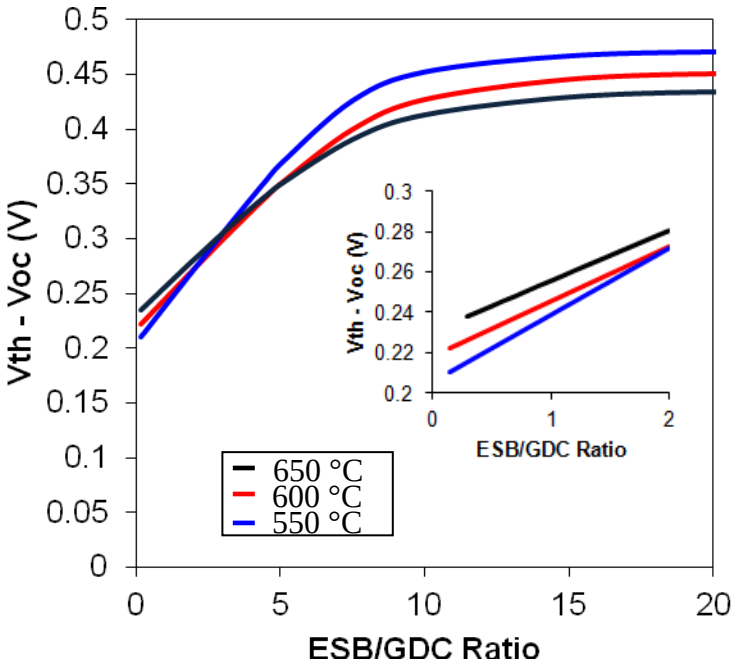

Figure 4.2.6: Calculated dependence of the difference in theoretical and open circuit voltages on ESB/GDC ratio.

From the calculated result shown in Figure 4.2.6, we overlay it onto the scattered result of the OCV dependence on ESB/GDC ratio from the sample set in this work. These results are displayed in Figure 4.2.7. In general, the data is highly scattered likely due to the strong dependence on total thickness demonstrated earlier. For 600 °C and 550 °C, the calculated result falls within the actual results from our sample set. However at 650 °C, the data set is consistently lower than the expected OCV. This could be due to a temperature dependence of which process is favored for determining the OCV, the ESB/GDC ratio or the total thickness. This is supported by the weaker correlation of OCV to total thickness at 600 °C and 550 °C.

Another consideration is at higher temperatures, any degradation is exacerbated and OCV values reflect a lower OCV than would be achieved should the anode reduce in a timely manner. Anode reduction typically takes 2 - 6 hours at 650 °C. In fact over time, at 650 °C the OCV does degrade at different rates and is

dependent upon the GDC thickness, as shown in Figure 4.2.8a. For GDC ~ 40 μm, 20 μm, 12 μm this rate is approximately 1.0 mV/hr, 2.0 mV/hr, and 7.5 mV/hr, respectively. At 5 μm the effect is difficult to measure and estimated to be greater than 50 mV/hr. The origin of this degradation is unknown, but there are a number of possible causes. First, there could be defects in the GDC layer that is more impactful at lower thicknesses. The 5μm GDC and anode substrates shrink less during the sintering step, so layer consistency may be a concern or the interface with the anode may be under stress. Another possible reason for degradation is during sintering of the ESB a diffusion layer forms between the GDC and ESB where the bismuth oxide appears to diffuse into the GDC. When attempting to eliminate additional sintering to reduce this effect (discussed in optimized cell later), while initially successful at fabricating a clean interface between GDC and ESB, testing at 650 °C for 80 hours still results in the diffusion phenomena. This can be seen in Figures 6b-c on a cell after 80 hours of testing. The GDC fracture surface exhibits intergranular fracture and smaller grain sizes near the ESB but further from the ESB become transgranular (with contrast as a result of grain orientation), indicating strong grain boundaries of the non-diffusion region with larger grains that are able to continue to coarsen at temperature. A third possible origin for the degradation could be in the cathode if mobility could lead to concentration polarization or if the current collector materials (Ag and Pt) are poisonous to the bismuth oxide at 650 °C resulting in extra phase formation. In that case, in the future we could test with a more inert current collector like Au.

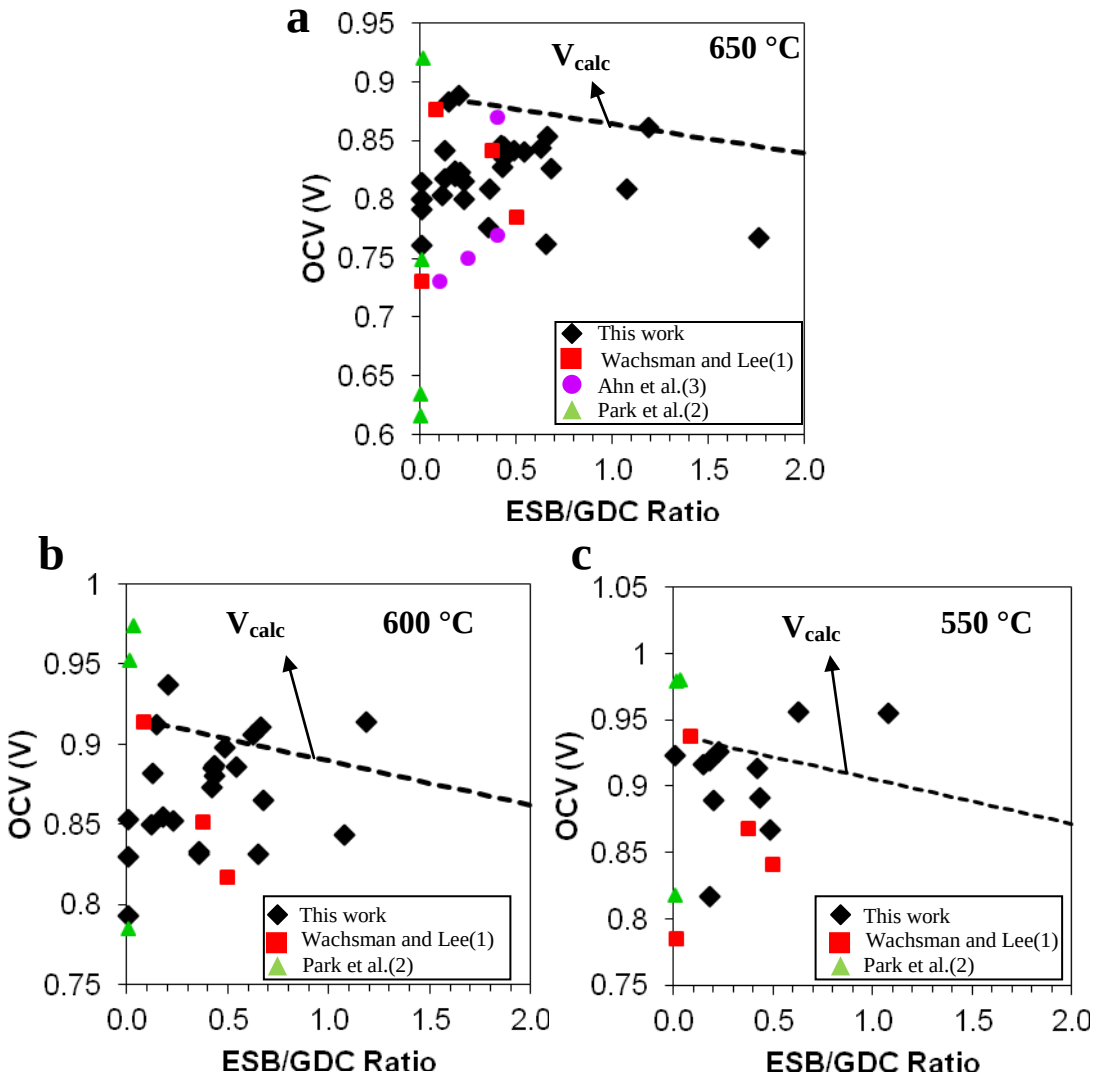

Figure 4.2.7: OCV results as compared with ESB/GDC ratio for 650 °C showing data from previous work with red squares (a) 600 °C (b), and 550 °C (1). Overlaid onto the plots are the calculated OCV (V_{calc}).

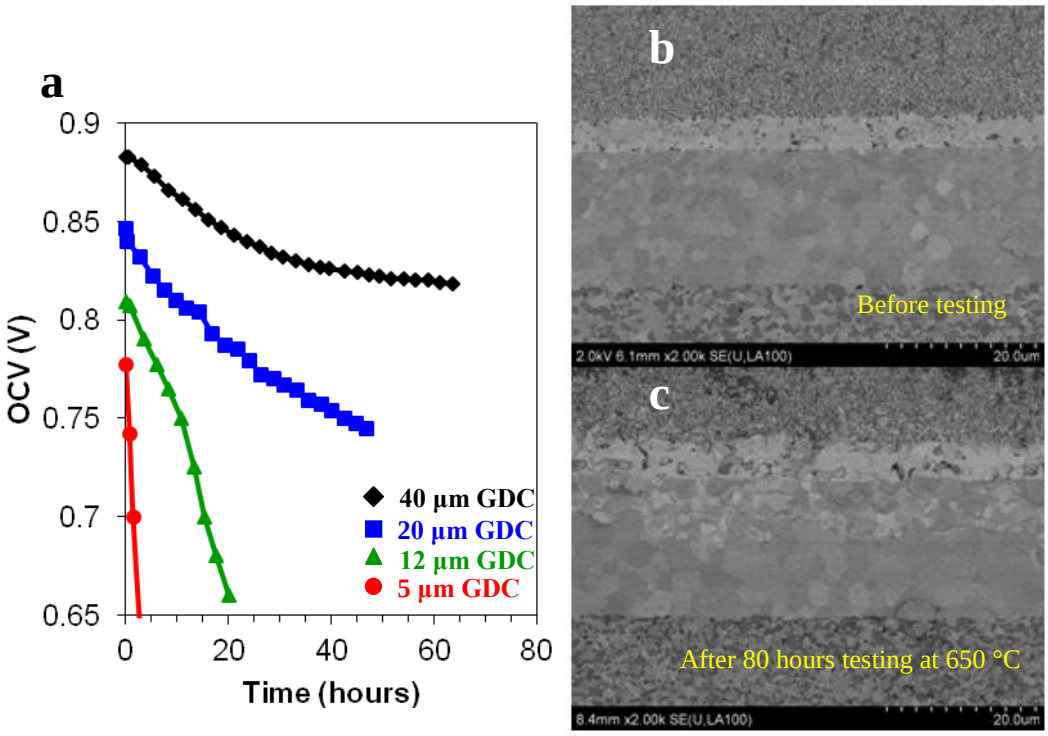

Figure 4.2.8: Representative OCV degradation over time of samples 1, 7, 22, and 30 (a), and SEM images of a cell with minimized sintering conditions after sintering (b) and after 80 hours of testing at 650 °C.

In the last column of Table 4.2.1 is a listing of the various sources of ESB that were used in this data set. There is a possibility that the correlations may be stronger in individual batches of cells, so cells measured on the ~12 µm and ~20 µm GDC at 650 °C are separated by the origin of the ESB with greater than 3 data points (thus excluding Trans Tech material) for both the total thickness (Figure 4.2.9a) and ESB/GDC ratio (Figure 4.2.9b). The total thickness correlation remains intact even in these subdivisions of sample batches. While the ESB/GDC ratio has a positive correlation in Sigma Aldrich and CP materials, the SS material with the largest sample size, appears to have the opposite correlation that more closely follows the slope of the calculated result shown in Figure 4.2.7a. These positive correlations happen to be coincidental. In the CP and Sig subsets the ESB/GDC ratio increases as

the total thickness increases purely by coincidence. We have already demonstrated that the primary driving factor for OCV in our data set is the total thickness, and therefore we do expect to see the OCV increase with increasing ESB/GDC ratio in these two subsets. Once enough data has been added to alleviate some of these correlations between ESB/GDC and the total thickness as a simple result of processing, the correlation appears to follow the expected calculated result for OCV dependence upon ESB/GDC ratio.

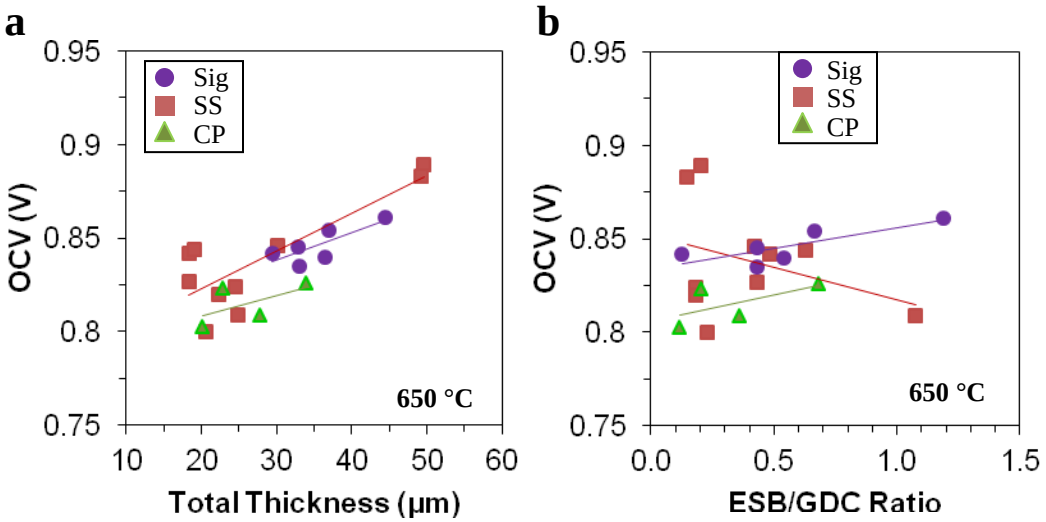

Figure 4.2.9: Separation of ESB origin subsets from Sigma Aldrich (Sig), solid state (SS), and coprecipitated (CP) powders for OCV versus a) total thickness and b) ESB/GDC ratio.

4.2.4 Critical ESB/GDC Ratio

An additional consideration is the thermodynamic limitation of ESB/GDC ratio due to the decomposition of the ESB. The decomposition partial pressure of oxygen for ESB is ~10^{-13} atm at 650 °C (67). A critical value for r_s can be calculated when (70):

$$r_s > \frac{\sigma_{O2-}^{GDC} ln\left[\left(P_{O2}^{I}\right)^{-1/4} + \sigma_{O2-}^{GDC}/\sigma_e^{GDC,0}\right] - ln\left[\left(P_{O2}^{dec}\right)^{-1/4} + \sigma_{O2-}^{GDC}/\sigma_e^{GDC,0}\right]}{\sigma_{O2-}^{ESB} ln\left[\left(P_{O2}^{dec}\right)^{-1/4} + \sigma_{O2-}^{ESB}/\sigma_e^{ESB,0}\right] - ln\left[\left(P_{O2}^{II}\right)^{-1/4} + \sigma_{O2-}^{ESB}/\sigma_e^{ESB,0}\right]} \qquad \textit{(Eq. 4.7)}$$

At 650 °C, 600 °C, and 550 °C the inverse of this critical value (ESB/GDC ratio) is 0.31, 0.36, and 0.37 respectively. These values are smaller than much of our sample set, meaning subsequent degradation is likely over time as a result of the decomposition of the ESB in those samples. However these results can assist with the strategic design of an ideal cell.

In revisiting the data presented in Figure 4.2.2a, there is a reasonable number of samples in the 18 μm to 24 μm total thickness range which are expected to have similar values yet they vary greatly. This may be an ideal thickness range due to smaller thickness which would result in a lower ASR, but is thick enough that defects in the layers may not be detrimental to performance through degradation. When looking in this similar total thickness range, we can plot these data points alone as a function of the ESB/GDC ratio. This is shown is Figure 4.2.10 along with the calculation for expected open circuit voltage given the ESB/GDC ratio. An interesting correlation arises, and trend lines are drawn as a guide to the eye. The open circuit voltage appears to increase up to about an ESB/GDC ratio of 0.3, which corresponds to the critical ratio for degradation. Then beyond that, instead of continuing to approach theoretical values, the OCV plateaus likely due to decomposition of the ESB that occurs above the critical thickness ratio. However a cell was not fabricated that can fill in the gap between 0.2 and 0.4 ESB/GDC thickness. This would be the optimal OCV for this thickness range as the trend in increased OCV from the sample set increases up to this value. A potential reason for the deviation from the calculated OCV could be defects in the thin ESB layer. Between ESB/GDC ratio 0 to 0.2, the ESB layer is less than 4 μm in thickness. There

could be large features or inhomogeneities present but simply not present in the particular cross section we observed in the SEM. The smaller this layer thickness, chances are greater a defect would impact the entire thickness of this layer and potentially create a pathway from the GDC to the cathode and allow some leakage current to pass through. At a ratio of 0.3, we can hope to minimize this effect but still be below the critical thickness ratio that would result in decomposition.

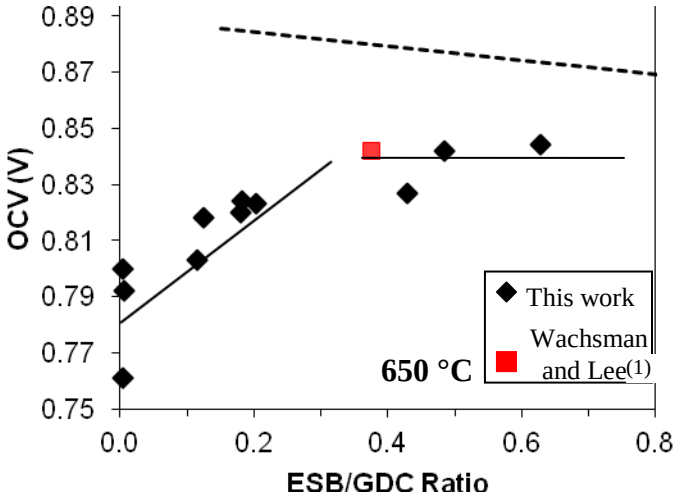

Figure 4.2.10: Sample cells in the 18 to 24 µm total thickness range plotted against ESB/GDC ratio at 650 °C inclusive of a sample from Wachsman and Lee (1). The calculated OCV is shown as a dashed line. Solid lines are drawn as a guide to the eye.

4.2.5 Cell Optimization

A new cell was synthesized matching these parameters with ESB thickness of 5 µm and GDC thickness of 18 µm, achieving an ESB/GDC ratio of 2.8, comfortably below but near the decomposition ratio. However to avoid any possible degradation during sintering, the ESB and LSMESB layers were applied and co-fired onto the GDC surface in just one sintering step. This cell's OCV at 650 °C was 0.873 V, very close to the calculated value of 0.881 V. The galvanostatic and EIS results are shown below in Figure 4.2.11. This cell achieved 1.4 W/cm^2, 0.96 W/cm^2, and 0.51 W/cm^2

at 650 °C, 600 °C, and 550 °C, respectively, which is among the highest reported values for a bilayer SOFC using simple, cost effective and scalable synthesis techniques.

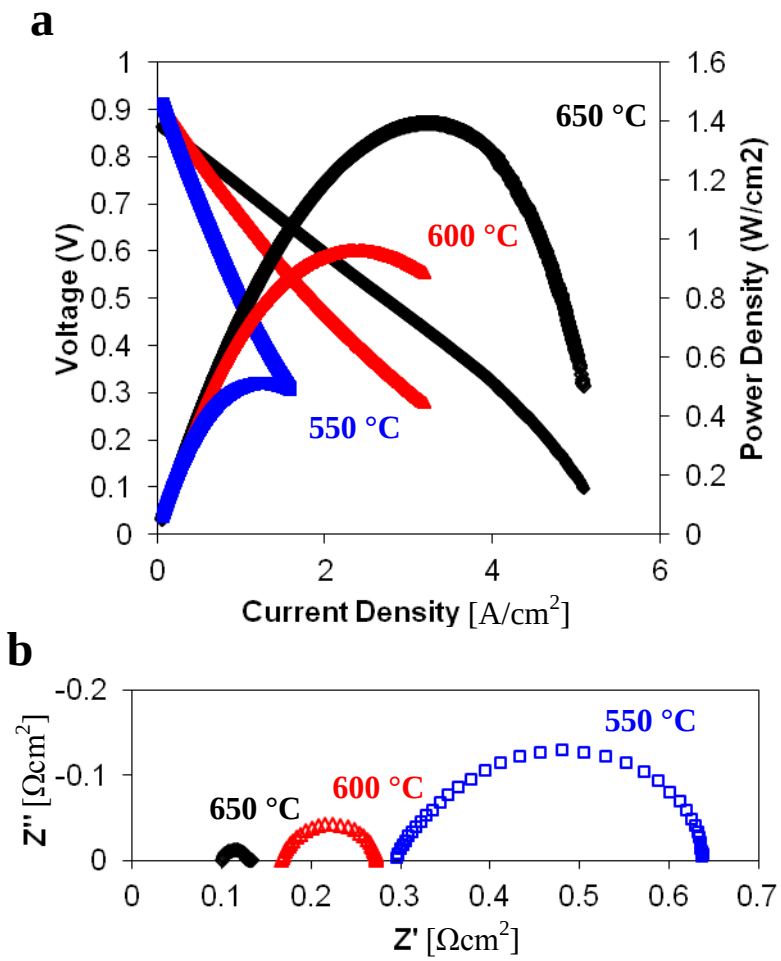

Figure 4.2.11: Electrochemical performance of strategically designed cell: IV measurement (a) and EIS result (b).

4.3 Conclusions

4.3.1 Summary

The sample set adequately demonstrated a strong positive linear correlation of OCV with total thickness as mathematically predicted. However while the ESB/GDC ratio did not show a clear relationship to OCV, calculated values fit reasonably well

with the 600 °C and 550 °C data set. Upon further investigation into a subset of samples of approximately 20 μm, there was in fact a correlation at 650 °C that approached the theoretical value for OCV predicted by mathematics. Critical ESB/GDC ratios were calculated for the degradation of ESB and imply the ESB/GDC ratio should be less than or equal to 0.31, 0.36, and 0.37 at 650 °C, 600 °C, and 550 °C respectively. A high performance cell was synthesized based upon the optimization of OCV near the degradation limit of ESB/GDC ratio less than 0.3 in the ~20 μm total thickness range and yielded some of the highest reported values for maximum power density reported for cells synthesized through facile and cost effective routes. This demonstrates that strategic design of bilayer cells based upon thermodynamic principles can result in optimal performance, and more cells can be synthesized having an understanding of the total thickness and ESB/GDC ratio impacts on the open circuit voltage.

Chapter 5: Rational Design of SOFC Cathodes Via Nanotailoring of Co-Assembled Composite Structures

5.1 Introduction

Solid oxide fuel cells (SOFCs) have tremendous potential due to having the highest fuel to electricity conversion efficiency (1) as well as unique fuel flexibility,(77-81) allowing the use of various types of hydrocarbon fuels (including biomass) and hydrogen, and thus providing a critical energy solution (82). Lowering the SOFC operating temperature below 800 °C is critical to reduce the system costs and performance degradation rates, enhance the durability and thermal cycling as well as shorten the start-up time, resulting in new opportunities in personal power and transportation markets (1). Achieving high performance SOFCs at reduced temperature is impeded primarily by increased cathode polarization resistance due to the thermally activated nature of the oxygen reduction reaction (ORR) (83).

Recently cobaltite-based perovskite materials (e.g., $Ba_{1-x}Sr_xCo_{1-y}Fe_yO_3$ (BSCF)) (17) have been highlighted due to their mixed ionic and electronic conducting (MIEC) character and oxygen reduction reaction (ORR) activity at

reduced temperature (12, 14, 16-17, 84) . However, their practical applications are limited by reactivity with the most widely used yttria stabilized zirconia (YSZ) electrolytes (85-86) and questionable long-term stability due to CO2 poisoning and Sr segregation (87-88). In contrast, at reduced temperature (<800 °C) conventional $La_{1-x}Sr_xMnO_3$ (LSM) demonstrates high stability during long-term operation and compatibility with most SOFC electrolytes including YSZ,(29, 89) but has low electrocatalytic activity due to negligible oxygen ion conductivity. Recent oxygen in situ isotope exchange (IIE) studies of LSM show that there is no energy barrier for dissociative adsorption of oxygen on the surface, as evident by the apparent negative activation energy for oxygen exchange (90-91).

Stabilized bismuth oxides in the fluorite structure have exceptionally high ionic conductivity and ORR rate. For example, the oxygen ion conductivity of 20 mol%-doped erbia-stabilized bismuth oxide (ESB) at 500 °C (0.0268 Scm^{-1}) is 30 times greater than that of YSZ (0.0009 Scm^{-1}) (92-93). Moreover, bismuth oxides have a remarkably high oxygen surface exchange coefficient (k_s), which is much higher (by a factor of 10^3 at 700 °C) than that of YSZ (94) and even competitive with that of the highest performance cobaltite-based perovskite cathodes (95). Although the ORR involves multiple mechanistic steps from oxygen adsorption to incorporation into the electrolyte lattice at electrochemically active triple-phase boundaries (TPBs), it can be more simply described by two major rate limiting steps as follows: (96-98)

$$\text{Step 1 : Dissociated adsorption : } O_2(g) + 2S \underset{k_{-1}}{\overset{k_1}{\leftrightarrow}} 2O_{ad}$$

$$\text{Step 2 : Oxygen incorporation : } O_{ads} + V_o \underset{k_{-2}}{\overset{k_2}{\leftrightarrow}} O_o + S$$

where O_{ads} is a surface adsorbed oxygen, O_o a lattice oxygen in the surface layer, V_o a surface oxygen vacancy (empty), and S a surface site. k_1 , k_{-1}, k_2, and k_{-2} are reaction-rate constants.

Thus, toward a rational design of SOFC cathodes we integrated the superior dissociative adsorption (step 1) property of LSM surfaces with the superior oxygen incorporation (step 2) of highly conductive stabilized bismuth oxides (34) by a co-assembled ESB-LSM nanocomposite particle, as illustrated in Figure 5.1.1a. Moreover, this well-tailored nanostructure results in highly extended electrochemically active TPBs in the 3D porous cathode bulk. However, the development of dual-phase nanocomposite particles comprised of multicomponent ceramics, is extremely challenging due to their high surface area (thus, high surface energy), leading to micron-size agglomeration of each phase's particles in the initial stage of mixing combined with intercomponent reaction during sintering at high temperature. Therefore, we developed an in situ co-assembly process for the nanocomposite $La_{0.8}Sr_{0.2}MnO_3$ (LSM)-$Bi_{1.6}Er_{0.4}O_3$ (ESB) through uniquely conjugated reverse-strike coprecipitation and glycine-nitrate combustion process (GNP) at extremely low temperature (<300 °C).

A conceptual process diagram is shown in Figure 5.1.1b–d and a more in-depth experimental description is discussed is included in Chapter 2. To preclude intercomponent reactions between LSM and ESB (e.g., Sr^{3+} and Bi^{3+}) during the synthesis process, “flower-like” high surface area nanoESB precursor precipitates (Figure 5.1.2) of $Bi(OH)_3$ and $Er(OH)_3$ confining Bi^{3+} and Er^{3+} were performed by the CP method discussed in Chapter 2.

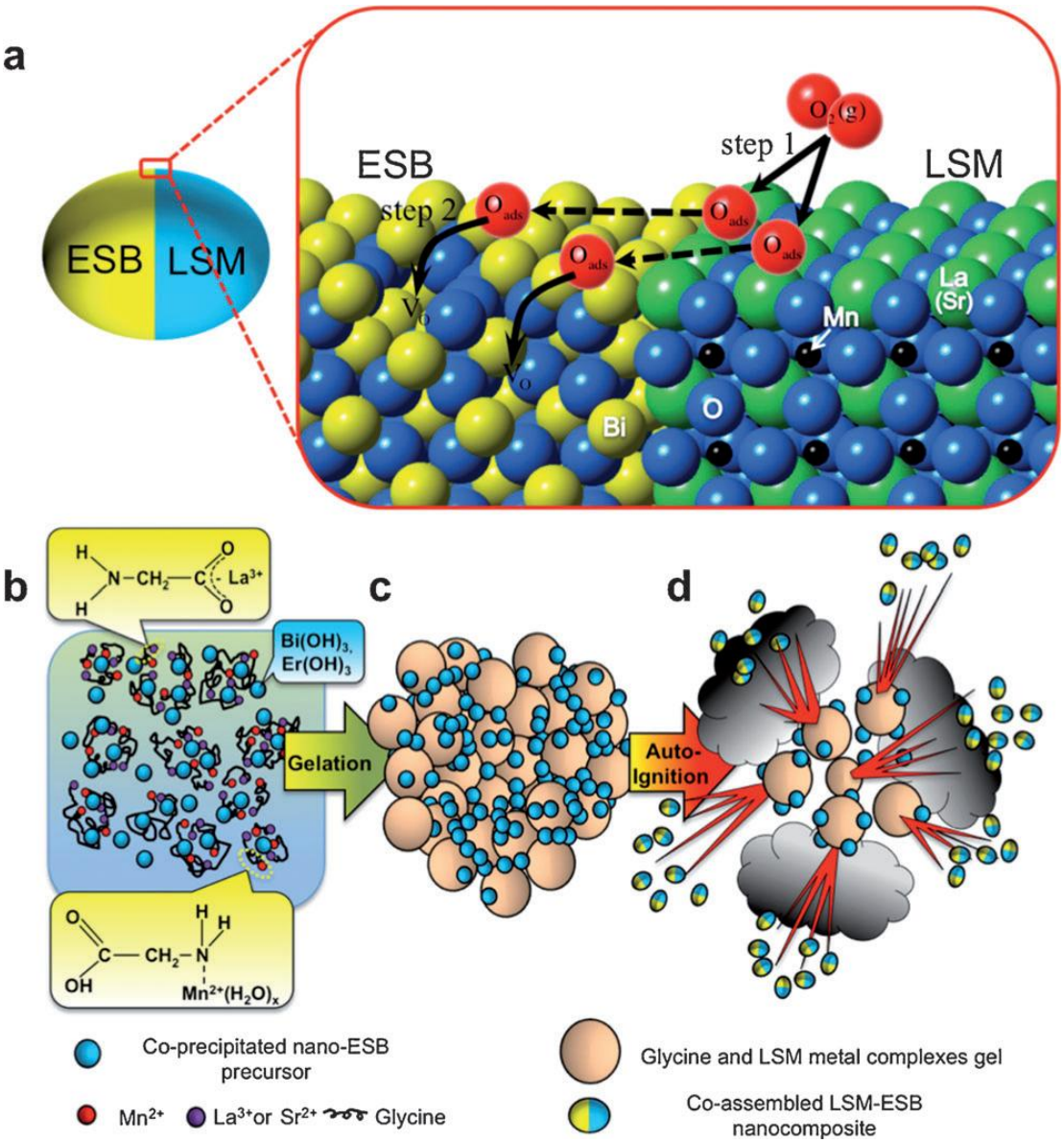

Figure 5.1.1: a) Proposed rational design of a SOFC cathode nanocomposite particle consisting of a half ESB phase and a half LSM phase (left) and illustration of the two-step ORR mechanism with superior oxygen dissociative adsorption on LSM surface and fast oxygen incorporation into ESB phase (right). Color code: red, O ions from air; blue, lattice O ions; yellow, Bi ions; black, Mn ions; green, La (or Sr) ions. The dotted arrows indicate oxygen ion diffusion on the nanoparticle surface. Conceptual diagram of the novel in situ co-assembled nanocomposite process: b) molecular level mixing of the coprecipitated ESB precursors consisting of $Bi(OH)_3$ and $Er(OH)_3$ with glycine and LSM–metal complexes; c) water drying and gelation; d) auto-ignition by glycine–nitrate combustion.

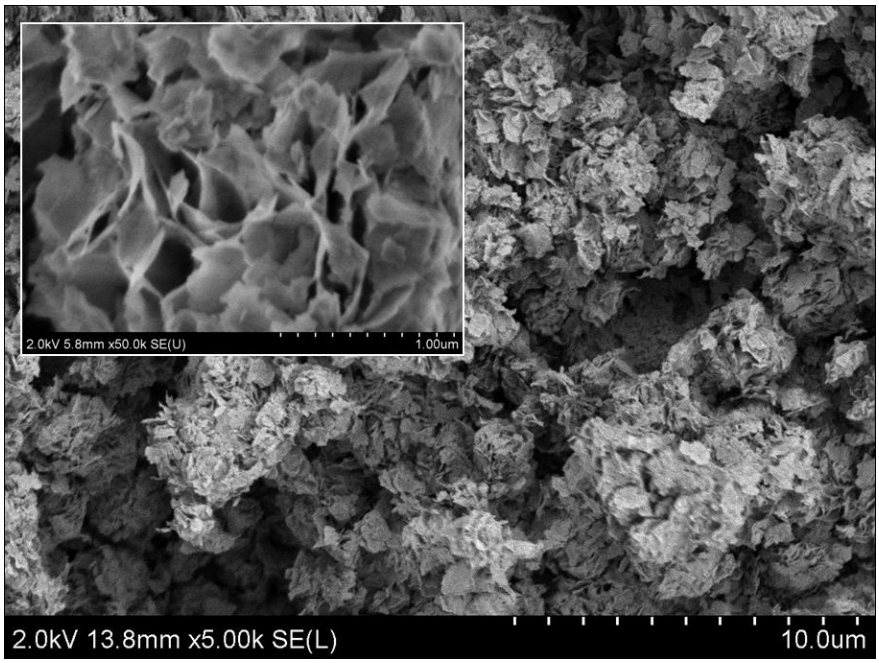

Figure 5.1.2: SEM image of as-synthesized CP ESB precursor material with higher magnification in inset.

5.2 Results and Discussion

5.2.1 Structural Analysis

X-ray diffraction (XRD) analysis (upper spectrum in Figure 5.2.1a) reveals that the as-synthesized powders are fully crystallized for both LSM and ESB phases with minor peaks of unreacted $Bi(OH)_3$. Moreover, there is no evidence for any inter-reaction between the two phases, indicating successful in situ crystallization of selective components for dual-phase formation. On the basis of the propellant chemistry (99) the stoichiometric redox reaction between the oxidizer (LSM metal nitrates) and fuel (glycine), which is responsible for the crystallization of LSM, was calculated. We started the process with a G/N ratio of 0.54, which is close to the stoichiometric ratio (0.56). In situ crystallization of the ESB phase is attributed to the short range atomic movement within ESB precursors through fast calcination (< 3 s) due to the adiabatic flame heat from the GNP reaction, which effectively prevents any

inter reaction with the LSM components. We further annealed the as synthesized LSM–ESB up to 800 °C to simulate actual SOFC operating conditions (≤750 °C) and confirmed the compatibility and stability of both phases (middle spectrum in Figure 2a), demonstrating the suitability for SOFC applications. However, without glycine the auto-ignition did not occur and we observed secondary phase formation between Bi^{3+} and Sr^{2+} ($SrBi_4O_7$) as shown in the lower spectrum in Figure 5.2.1a, indicating that the auto-ignition step plays a critical role for in situ crystallization of multicomponent, dual-phase composites.

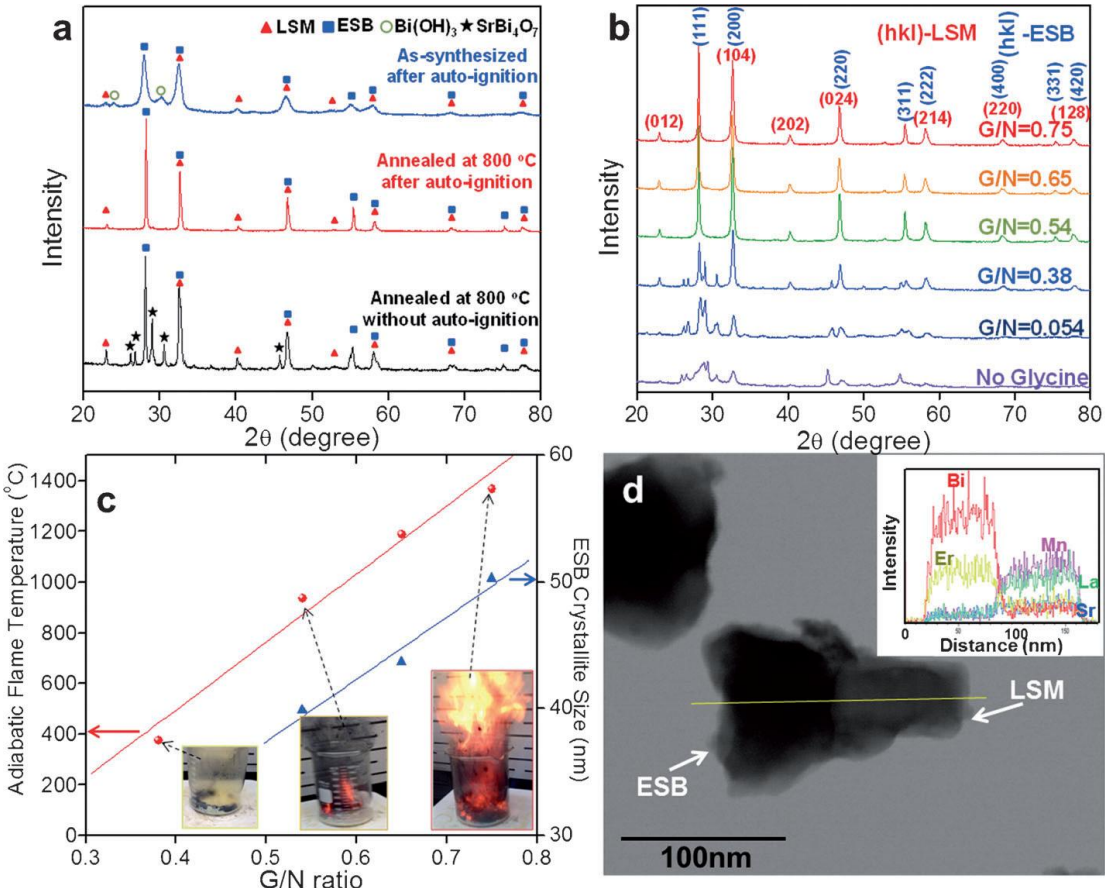

Figure 5.2.1: a) X-ray diffractograms of as-synthesized (upper), annealed at 800 °C with auto-ignition (middle), and annealed at 8008C without auto-ignition (lower) of icn-LSMESB powders. b) X-ray diffractograms of icn-LSMESB powders with various G/N ratios after annealing at 800 °C with autoignition. c) Adiabatic flame temperature (left Y-axis) and ESB crystallite size (right Y-axis) as a function of G/N ratio. Insets are still frames of highest fire flame during the process. d) TEM micrograph of icn-LSMESB particles with a G/N ratio of 0.54 after annealing at 800 °C. Inset is EDS line scan spectra along the yellow line in the TEM image.

5.2.2 Impacts of Glycine to Nitrate Ratio

Figure 5.2.1b shows the XRD patterns of LSM–ESB samples with different G/N ratios after annealing at 800 °C. The results indicate that a G/N ratio of ≥ 0.54 produces enough thermal energy both to oxidize LSM nitrates and to crystallize ESB precursors. Based on the redox reactions with various G/N ratios, the effect of the glycine amount (i.e., G/N ratio) was estimated from the enthalpy of combustion and the corresponding adiabatic flame temperature and the results are plotted in Figure 5.2.1c. It is noted that the actual flame temperature values are expected to be somewhat lower than the calculated ones due to radiative heat losses and incomplete redox reactions. Nevertheless, actual experimental combustion photos of the highest flame for each G/N ratio (insets of Figure 5.2.1c) visually confirm how the glycine amount impacts the adiabatic flame temperature. Moreover, this result is in good agreement with the recently reported minimum calcination temperatures of nanoESB obtained by co-precipitation (~500 °C) (34).

The crystallite size (L) of the ESB phases with various G/N ratios was estimated (Figure 5.2.1c) from the highest intensity (111) peaks from XRD patterns in Figure 5.2.1b by the Scherrer equation, (23) clearly indicating a strong dependence of the ESB crystallite size on the G/N ratio. Thus, the above results demonstrate that the glycine–metal complexes act as “nanofurnaces” for the in situ calcination of ESB and the final product size is precisely controlled by the fuel (glycine) amount.

Figure 5.2.2 shows the impact of the G/N ratio on ASR when incorporated into icn-LSMESB/ESB/icn-LSMESB symmetric cells for EIS analysis. Across all temperatures, the optimal performance is achieved with G/N = 0.54, and this ratio is selected for further testing. This result is expected because this ratio has the smallest

particle size due to the lower adiabatic flame temperature but still yields the appropriate LSMESB phase.

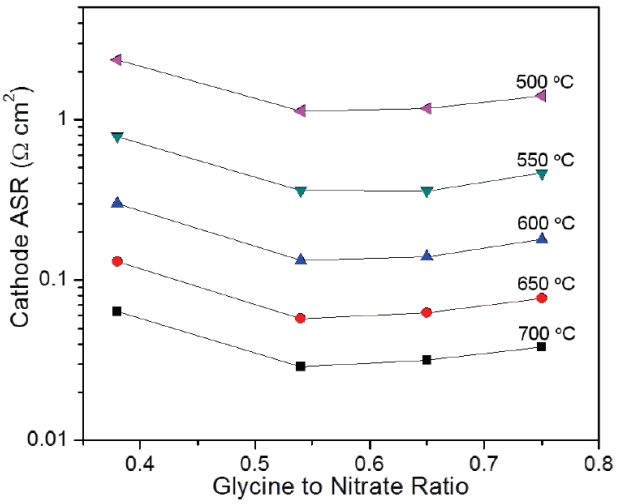

Figure 5.2.2: Cathode ASR of icn-LSMESB as a function of G/N ratio from 500 to 700 °C.

5.2.3 Morphology

Figure 2d shows the representative structure of nanocomposite LSM–ESB particles synthesized with a G/N ratio=0.54 obtained using transmission electron microscopy (TEM), which are very similar to the schematic diagram of the proposed co-assembled nanoparticle in Figure 1a. It is impressive that even after heat treatment at 800 °C, a nanoscale primary particle size was maintained at ca. 150 nm.

Moreover, we observed that these particles were dual-phase LSM and ESB nanoparticles without intermixing. Energy dispersive X-ray (EDX) line-scan analysis in scanning TEM (STEM) mode (upper inset in Figure 5.2.1d) clearly shows that the ESB and LSM are seamlessly co-assembled without any interaction. The particle size of the co-assembled ESB phase estimated from the TEM observation was ca. 70 nm, which is comparable to the value of ESB crystallite size (~44 nm) from the XRD result in Figure 5.2.1c. Although the in-depth coassembly mechanism is not yet

conclusive, we believe that self-assembling between adjacent LSM and ESB particles involves an excess exothermic energy from the adiabatic flame temperature just after crystallization of each phase in the initial GNP step.

5.2.4 Electrochemical Performance

The polarization resistance of the icn-LSMESB cathode at reduced temperature was evaluated with icn-LSMESB/ESB/icn- LSMESB symmetric cells by electrochemical impedance spectroscopy (EIS). Figure 5.2.3 a shows the Nyquist plots of the cells with the icn-LSMESB cathodes with the optimum G/N ratio of 0.54 and 37 vol% LSM content (Figure 5.2.2) from 500 to 677 °C. For direct comparison, all impedance spectra were ohmic-resistance-subtracted. The corresponding cathode area specific resistance (ASR) of icn-LSMESB was extremely low (e.g., 0.078 Wcm^2 at 600 °C), drastically reducing ASR by more than 140 times compared to conventional LSM–YSZ cathodes (e.g., 11.37 Wcm^2 at 600 °C;(11) (Figure 5.2.3b) and the lowest ASR reported to date for any LSM-based cathode with any microstructure (Figure 5.2.4).

Moreover, the performance of icn-LSMESB is superior to that of many cobaltite based high performance cathodes (e.g., 0.078 Wcm^{-2} for icn-LSMESB versus 0.27 Wcm^{-2} for $La_{1-x}Sr_xCo_{1-y}Fe_yO_3$–$Sm_{1-x}Sr_xCoO_3$ (LSCF–SSC) at 600 °C (16) and essentially identical to the state-of-the-art benchmark cathode, BSCF (17) (Figure 5.2.3b). This result clearly demonstrates that our rational cathode design, based on co-assembled nanostructures of locally confined desired surface properties, dramatically enhances the ORR rate not only due to greatly extended electrochemically active TPB sites of a highly percolated dual-phase nanonetwork, but also due to the synergy between enhanced dissociative adsorption of oxygen by

isolated LSM surface integrated with fast oxygen incorporation kinetics into ESB lattice as shown conceptually in Figure 5.1.1a.

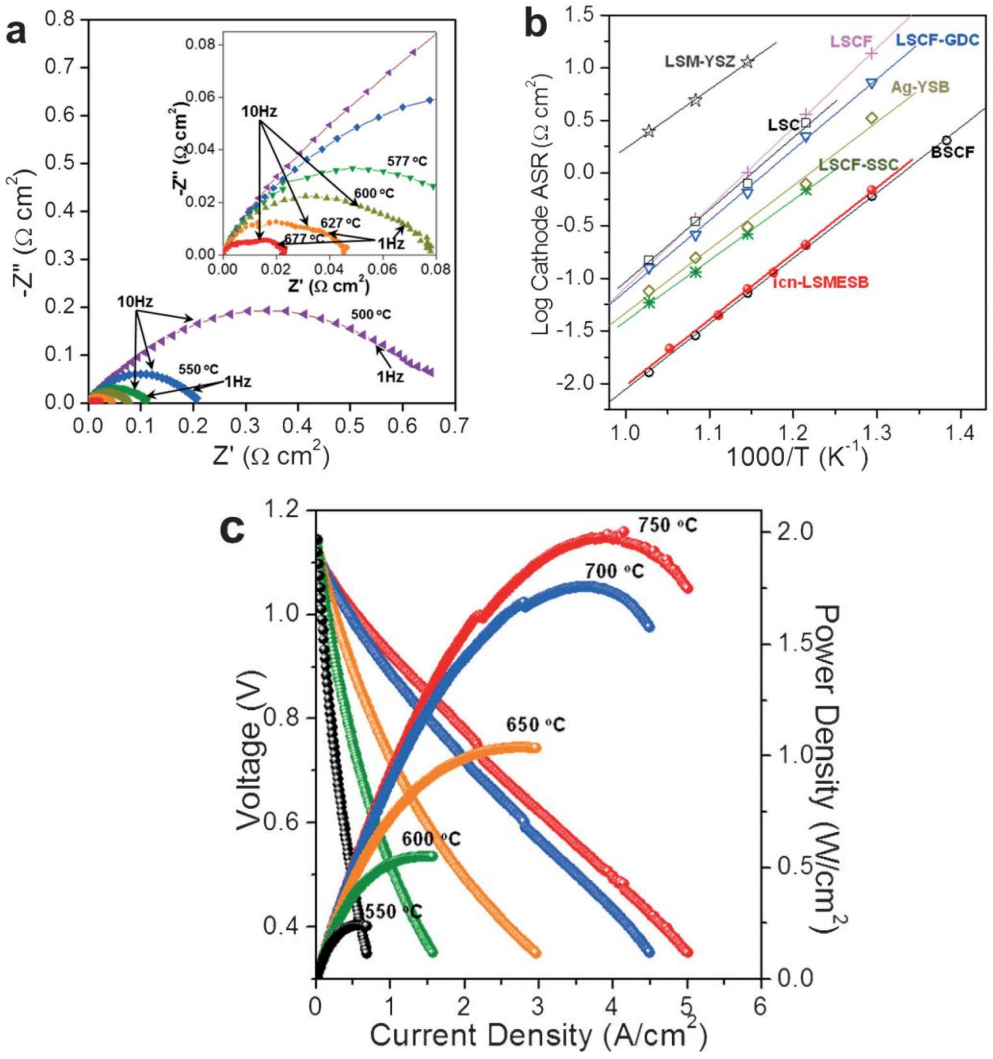

Figure 5.2.3: a) Nyquist plots of an icn-LSMESB/ESB/icn-LSMESB symmetric cell at the temperature range from 500 to 677 °C. b) Arrhenius plots of conductivity of icn-LSMESB compared with the conventional $La_{0.8}Sr_{0.2}MnO_3$ (LSM)–YSZ cathodes (11) and the state-of-the-art high performance cathodes including $La_{0.6}Sr_{0.4}Co_{0.5}Fe_{0.5}O_{3-d}$ (LSCF) (12), $La_{0.58}Sr_{0.40}CoO_{3-d}$ (LSC) (13), $La_{0.6}Sr_{0.4}Co_{0.5}Fe_{0.5}O_{3-d}$–$Gd_{0.2}Ce_{0.8}O_{3-d}$ (LSCF–GDC) (14), Ag–$Y_{0.25}Bi_{0.75}O_{1.5}$ (Ag–YSB) (15), $La_{0.6}Sr_{0.4}Co_{0.5}Fe_{0.5}O_{3-d}$ –$Sm_{0.5}Sr_{0.5}CoO_{3-d}$ (LSCF–SSC)(16), and $Ba_{0.5}Sr_{0.5}Co_{0.8}Fe_{0.2}O_{3-d}$ (BSCF)(17) at reduced temperature. c) Current–voltage (I–V) characterization of the SOFC with icn-LSMESB(cathode)/YSZ(electrolyte)/NiO-YSZ(anode) structure at the temperature range from 550 to 750 °C.

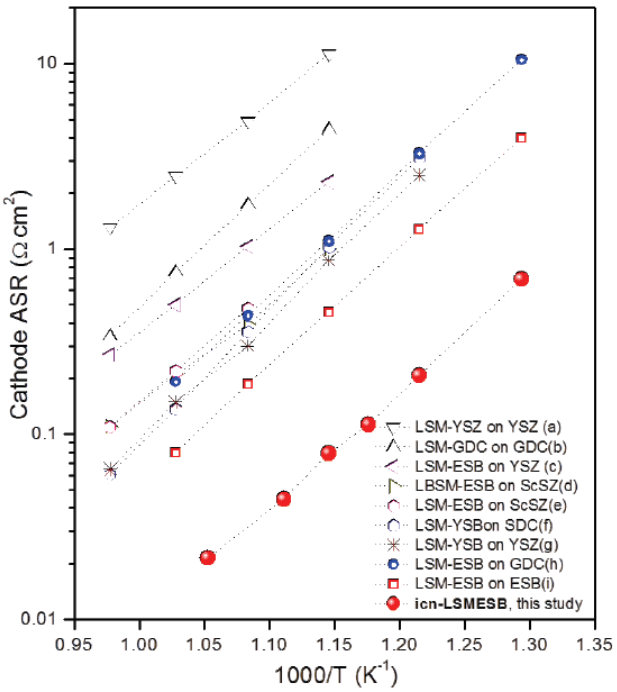

Figure 5.2.4: Arrhenius plots of the cathode ASR of icn-LSMESB cathode compared to various LSM-based cathodes including (a) $La_{0.8}Sr_{0.2}MnO_3$ -$Y_{0.16}Zr_{0.92}O_{2.08}$ (LSM-YSZ) (11), (b) $La_{0.8}Sr_{0.2}MnO_3$ -$Gd_{0.2}Ce_{0.8}O_{3-d}$ (LSM-GDC) (11), (c) $La_{0.8}Sr_{0.2}MnO_3$ - $Er_{0.4}Bi_{1.6}O_3$ (LSM-ESB) (18), (d) $La_{0.74}Bi_{0.1}Sr_{0.16}MnO_3$ - $Er_{0.6}Bi_{1.4}O_3$ (LBSM-ESB) (19), (e) $La_{0.84}Sr_{0.16}$ MnO_{3-d} - $Er_{0.6}Bi_{1.4}O_3$ (LSM-ESB) (20), (f-g) $(La_{0.85}Sr_{0.15})_{0.9}$ MnO_{3-d} - $Y_{0.5}Bi_{1.5}O_3$ (LSM-YSB) (21-22), (h-i) $La_{0.84}Sr_{0.16}$ MnO_{3-d} - $Er_{0.4}Bi_{1.6}O_3$ (LSM-ESB) (23). Also, ScSZ, SSZ, and SDC represent Sc-stabilized zirconia, $Sc_{0.1}Ce_{0.01}Zr_{0.89}O_{1.95}$ and $Sm_{0.2}Ce_{0.8}O_{1.9}$ electrolytes, respectively.

Figure 5.2.3c shows the current–voltage (I–V) characterization of the icn-LSMESB cathode on a full-structured SOFC from 550 to 750 °C, yielding exceptionally high performance in peak power density at reduced temperature (2.0 Wcm^{-2} at 750 °C and 1.8 Wcm^{-2} at 700 °C) compared to the recently reported YSZ-based SOFC performance (e.g., <1Wcm^{-2} at 700 °C)(100) with similar electrolyte and anode architectures. Further reduction of the SOFC operation temperature with even higher output power density is achievable if the icn- LSMESB is combined with other advanced SOFC components (e.g., highly conductive, functionally graded ceria/bismuth oxide bilayered electrolytes, (1) ultrathin (>100 nm) YSZ electrolytes obtained by chemical solution deposition (101), or bimodally integrated anode functional layers (102)).

Figure 5.2.5 shows scanning electron microscopy (SEM) micrographs of the SOFC with Ni–YSZ / YSZ /icn-LSMESB multilayers after I–V testing. As shown in Figure 5.2.3a, all layers are well-established with a dense YSZ electrolyte (ca. 7 mm) responsible for the high open-circuit voltage (OCV; Figure 5.2.3c). However, the exceptionally high power densities should be attributed primarily to the co-assembled nanostructural features of the ca. 30 mm thick icn-LSMESB cathode. Magnified SEM morphology of the icn-LSMESB in backscattered mode (Figure 5.2.6b) shows that both LSM and ESB phases are homogeneously intermixed with high 3D connectivity of each phase and the average particle size is less than 200 nm, similar to the primary particle size (150 nm) shown in Figure 5.2.1d, indicating that the co-assembled dual phase composite structure effectively prevents grain growth of the other phase during sintering. This observed nanostructure of the icn-LSMESB justifies the extremely low ASRs (Figure 5.2.3b) and the ORR enhancement mechanism, as explained above, as well as the resulting high power density of the SOFC (Figure 5.2.3 c).

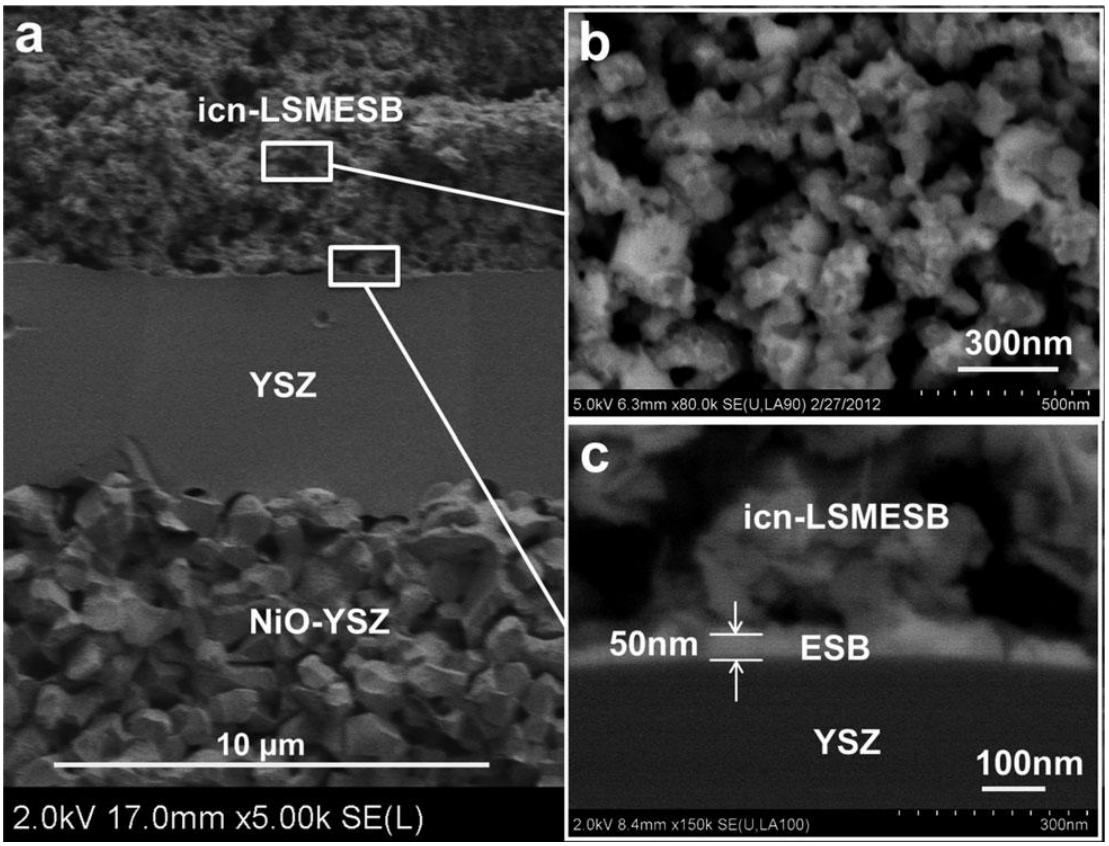

Figure 5.2.5: SEM images of a) icn-LSMESB-(cathode) / YSZ(electrolyte) / NiO-YSZ(anode) structures, and magnified images of b) icn-LSMESB cathode and c) cathode/electrolyte interface.

Moreover, we observed another striking feature of the icn-LSMESB cathode on the YSZ electrolyte: the self assembly of a continuous nanoscale ESB layer (~50 nm thick) at the cathode/electrolyte interface shown in Figure 5.2.5c. EDX analysis performed at this interface on the SEM at 150,000x magnification (Figure 5.2.6) demonstrated the ESB layer exists without mixing of YSZ electrolyte or LSM in the cathode. The formation of the extremely thin ESB layer can be explained by the high wettability and greater mobility by surface and lattice diffusion due to the lower melting temperature of bismuth oxide (~827 °C) as compared to the melting temperature of LSM and YSZ (>2000 °C). We believe this self-assembled nanoESB layer acts as an ESB/YSZ bilayered electrolyte, significantly improving the SOFC

performance due to enhanced oxygen incorporation at the icn-LSMESB/ESB interface as recently demonstrated (23).

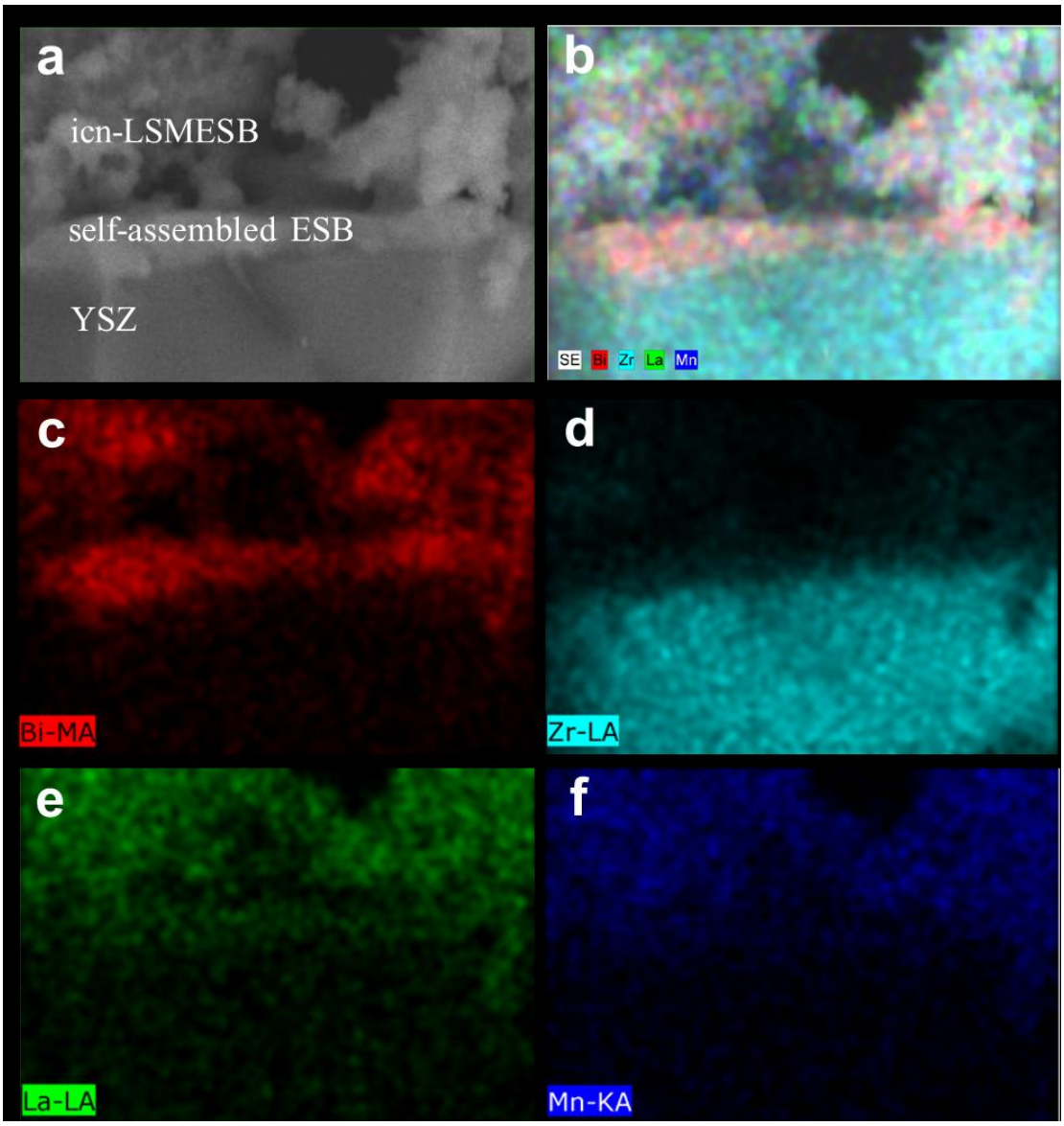

Figure 5.2.6: (a) SEM micrograph and (b) EDX mapping of the cross-section of an SOFC consisting of icn-LSMESB cathode and YSZ electrolyte, followed by individual element analysis of (c) Bi, (d) Zr, (e) La, and (f) Mn. This result clearly shows a self-assembled ESB layer on YSZ as well as no interfacial diffusion between the icn-LSMESB cathode and the YSZ electrolyte.

5.3 Conclusion

In summary, in order to achieve a rationally designed low temperature SOFC cathode based on desired ORR material properties, we developed a novel in situ co-assembly of multicomponent, dual-phase nanocomposites by uniquely conjugated wet chemical processes. Through nanoengineering, the desired surface properties of both phases were successfully isolated in the nanoregime (<80 nm), resulting in outstanding SOFC cathode performance at lower temperatures. Thus, we believe this intelligent nanoarchitecture is promising for electrochemical performance enhancement of composite electrodes with broad applications in energy storage and conversion devices.

Chapter 6: DWSB Synthesis and Conductivity Characterization and Application in LSM/DWSB Cathode

6.1 Introduction

A critical hurdle to the commercialization of SOFCs is the ability to reduce system cost. Lower operating temperature would allow for the use of less expensive interconnect materials, reduction of the start-up time, longer mechanical and chemical stability, thus reducing total system cost. However, lowering the operation temperature of SOFCs is difficult due to ionic conductivity limitations of electrolyte materials below 700°C. Recent developments in materials research have brought forth new options for ionic conductors with high conductivity at reduced temperatures. It has been demonstrated that erbium stabilized bismuth oxide (ESB) has one to two orders of magnitude higher ionic conductivity than conventional yttria-stabilized zirconia (YSZ) from 500 °C to 700 °C due to ESB's high oxygen vacancy concentration (1). Furthermore, the ionic conductivity of ESB in this temperature range is also ten times greater than that of gadolinia-doped ceria (GDC) (1).

$La_{0.8}Sr_{0.2}MnO_{3-\delta}$ (LSM) is an attractive solid oxide fuel cell cathode due to its reasonable electronic conductivity, high stability, and good compatibility with solid oxide fuel cell electrolytes. Previously we showed that LSM is also compatible with

bismuth oxide ionic conductors (23). However, this material is limited to operation at higher temperatures (greater than 800 °C) due to the high activation energy for oxygen reduction reactions. This has been addressed by several researchers by incorporating LSM into a composite electrode with an ionic conductor (26-29, 103). They have demonstrated that the homogenous mixing of the two phases yielded an extended triple phase boundary to allow for more sites for oxygen incorporation. The objective of this work is to further increase the triple phase boundary by incorporating a higher surface area ionic conducting species and achieve mixing with LSM at the nanoscale. Furthermore, by selecting a material with higher conductivity than conventional ionic conductors like gadolinia doped ceria (GDC) or yttria stabilized zirconia (YSZ), one can expect an improvement in interfacial polarization based on material selection as well.

6.1.2.Double Doping

In order to achieve even higher performance with bismuth oxide, we have taken a double-doping approach to reduce the total doping amount and increase the entropy of the system. Lower total doping reduces the probability of dopant association that can cause conductivity degradation (39, 44). Additionally, the use of two highly polarizable ions, like Dy^{3+} and W^{6+}, improves the mobility of the O^{2-} ion through the material (1, 7, 46). Our previous work uses this rationale for the development of dysprosium-tungsten doped bismuth oxide (DWSB) which has an even higher conductivity and stability at lower temperatures as compared to ESB (1, 44). The previous study used DWSB made through a solid state synthesis route to generate micron-sized particles. These materials will be produced again but to study

the change in activation energy in the conductivity results between 600 °C and 500 °C.

This work will also focus on the synthesis of DWSB through a wet chemical processing method. The objective of this synthesis is to reduce the particle size of the DWSB powder for its use in a solid oxide fuel cell cathode and utilize the material in place of conventional ionic conductors.

6.2 Results and Discussion

6.2.1 DWSB Characterization

CP DWSB powder and SS DWSB powder prepared as described in Chapter 2 was characterized and compared to observe the effect of synthesis method on particle size while still maintaining the appropriate crystalline phase. Figure 6.2.1 shows the comparison between the calcined CP and SS powder x-ray diffraction patterns. Both powders achieved phase purity after calcination, confirming the formation of the desired crystal structure using the CP method. Figure 6.2.1b shows the peak broadening of the CP powder diffraction peaks when compared to the SS material. According to the Scherrer equation, the approximate crystallite size was calculated from the diffraction peaks to be 21.2 nm and 53.9 nm for CP and SS powders respectively. This pattern is continued when measuring the particle size using dynamic light scattering and calculating particle size from the result of BET surface area analysis shown in Table 6.2.1. In all cases, the crystal size and particle sizes are consistently smaller for the CP powder than for the SS powder, as indicated in the particle size distribution in Figure 6.2.2. Microstructural images from SEM confirm

these results, showing a clear distinction in particle size between the two powders in Figure 6.2.3.

TABLE 6.2.1. **Summary of crystal and particle size measurements using various analysis techniques.**

Analysis Technique	CP DWSB size (nm)	SS DWSB size (nm)
Scherrer's Formula	21.2	53.9
Dynamic Light Scattering	247	1315
BET surface area analysis	69	854

Additionally, the BET surface area used to generate equivalent particle sizes reported in Table 6.2.1 is ten times greater for the CP powder (9.76 m^2/g) than with the SS powder (1.03 m^2/g). By enhancing the surface area available for the oxygen reduction reactions (ORR), there is a decrease in the polarization resistance. Also, this higher surface area is expected to help improve the sinterability of the powder when used as a thin layer electrolyte (23).

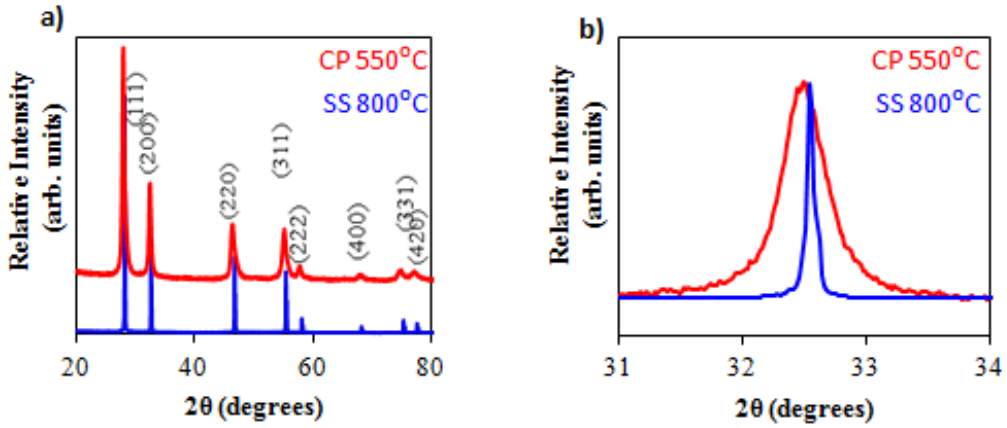

Figure 6.2.1: a) X-ray diffraction patterns for the CP (upper) and SS (lower) DWSB powders are shown. b) A closer look at the (200) peak showing the CP DWSB powder has broader peaks indicating smaller particle size.

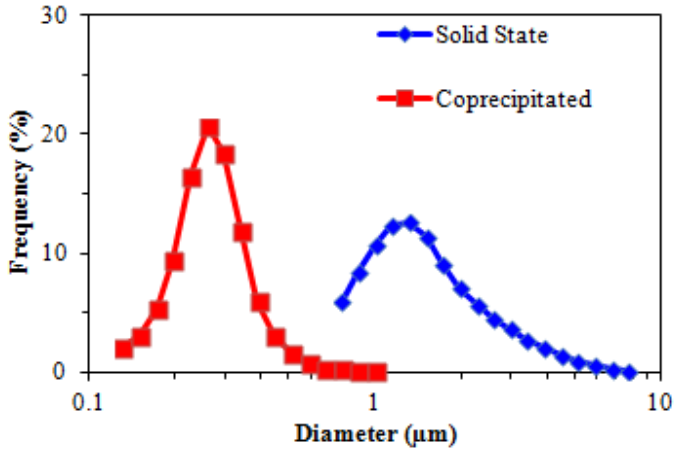

Figure 6.2.2: Particle size distribution of the calcined solid state and coprecipitated DWSB powders.

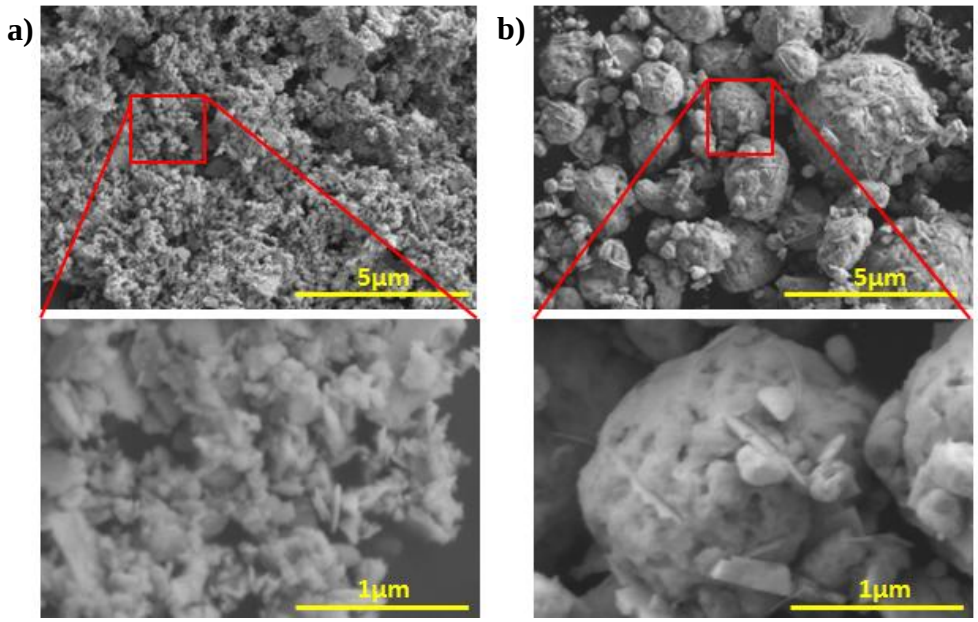

Figure 6.2.3 SEM micrographs of the calcined a) coprecipitated and b) solid state powders

6.2.2 DWSB Conductivity

Both the CP and SS powders were compared using EIS to ensure similar performance of the two materials in Figure 6.2.4. The CP powder actually achieves even higher ionic conductivity than the SS powder. The major impact of sintering nanopowder is the lower sintering temperature and the smaller size of the grains. We

know the grain boundary conductivity of ESB is high, so there may be a benefit to having more grain boundaries in the material. This is promising for incorporating the nano-sized CP powder into the cathode. SS ESB and its known activation energy change (change in slope) at 600 °C is also shown in Figure 6.2.4 as a reference. The change in slope for the DWSB materials has shifted to about 550 °C, indicating that the order/disorder transition may have been pushed to a lower temperature or possibly even avoided. The slope has a much more drastic change, so the nature of this activation energy change might be different.

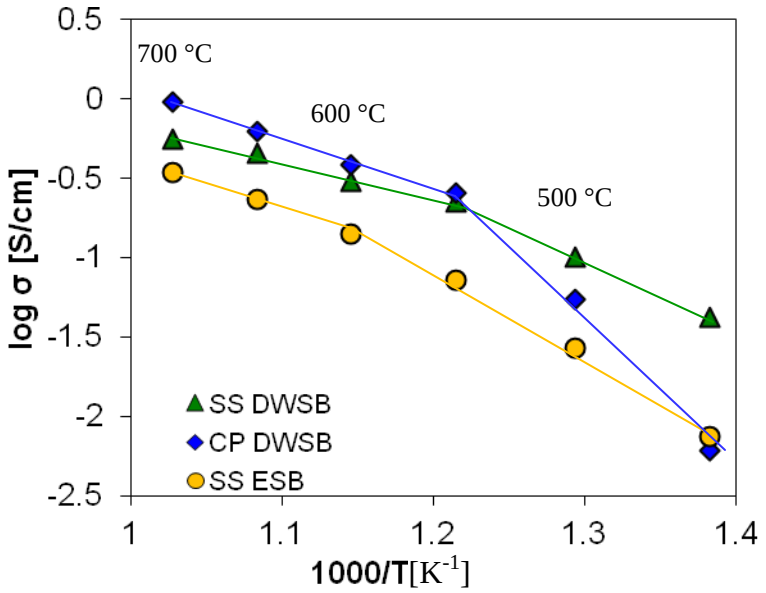

Figure 6.2.4: Symmetric cell conductivity from 700 °C to 450 °C of CP and SS DWSB powders as compared with SS ESB.

6.2.3 Change in Activation Energy

In order to learn the nature of this change in activation energy, neutron diffraction was utilized to observe the changes in the lattice. The results are shown in Figures 6.2.5a-b and Table 6.2.2 with Rietveld refinement and Le Bail fitting (24-25). In the unaged as-sintered sample, the ratio of the values for the 8c and 32f occupancy

of the oxygen atoms (0.7) is similar to that of Dy-stabilized bismuth oxide (DSB) with a 25 mol% Dy (0.77) studied previously by Boyapati et al. (63). Unfortunately, there was a phase change after the 500 °C anneal that eliminated the possibility of observing any changes specifically in the oxygen positions. However this indicates that the activation energy change in conductivity might be due to the phase change rather than the order/disorder transition. More studies performed at an anneal temperature closer to 550 °C could help determine if there is in fact an order/disorder transition that is masked by the phase transition from the cubic to monoclinic phase. Additionally, higher doping levels would stabilize the phase to lower temperatures, so neutron diffraction studies could be performed on higher doping levels to more effectively probe this possibility of the order/disorder transition. From the comparison of the fitting parameters, the annealed sample has a slightly smaller volume than the as-sintered sample which could impede ionic mobility. This combined with the more anisotropy in the structure explains the higher activation energy for conductivity at lower temperatures. Figure 6.2.4 shows a very dramatic change in activation energy for DWSB but a much more gradual one in ESB, which is already known to be a result of the order/disorder transition (38, 63-64). This supports that the phase transition is responsible for this change in activation energy in DWSB at 550 °C.

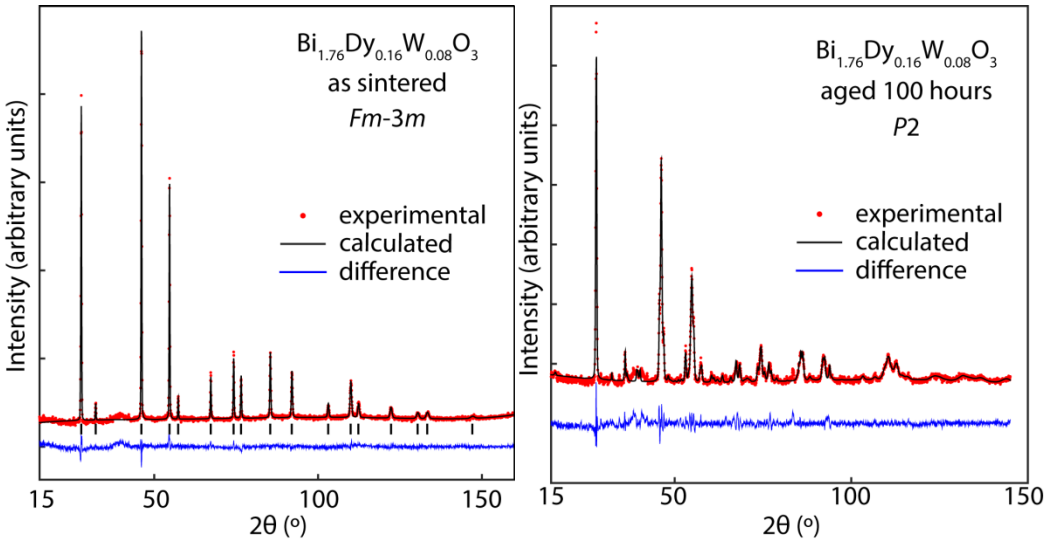

Figure 6.2.5: a) Rietveld refinement of neutron powder diffraction data for the as sintered DWSB material (24). The red dots represent the observed data. The solid black line represents the calculated pattern. The blue line represents the difference between the observed and calculated patterns. The black tick marks below the pattern represent the positions of the allowed reflections in the *Fm*-3*m* space group. b) Le Bail refinement of neutron powder diffraction data for a sample aged 100 hours at 500°C (25). The red dots represent the observed data. The solid black line represents the calculated pattern. The blue line represents the difference between the observed and calculated patterns. The monoclinic space group *P*2 was used to extract the lattice parameters from the pattern.

Table 6.2.2: Summary of parameters for the a) Rietveld refinement on the as-sintered sample and b) Le Bail fitting of the 100 hr 500 °C annealed sample

a)

As Sintered	
Space Group	Fm-3m
R_{wp}	4.54549
a (Å)	5.5618(1)
B_{eq} metal	2.75(3)
B_{eq} oxygen	6.2(2)
O x-coordinate	0.314(2)
O occ. 8c	1.24(6)
O occ. 32f	1.76(6)
Cell Volume (Å^3)	172.05(1)

b)

100 hr Anneal	
Crystal System	Monoclinic
a (Å)	5.5553(4)
b (Å)	5.6628(5)
c (Å)	5.4573(4)
beta (°)	89.478(6)
Cell Volume (Å^3)	171.67(2)

6.2.2 LSM/DWSB Characterization

The CP DWSB powder was incorporated into a composite cathode with LSM via the in-situ glycine nitrate method discussed in Chapter 2. X-ray diffraction confirms compatibility in Figure 6.2.6 where the composite material mixed at the

nano-scale and calcined to yield the two distinct phases of LSM and DWSB without the presence of impurity peaks.

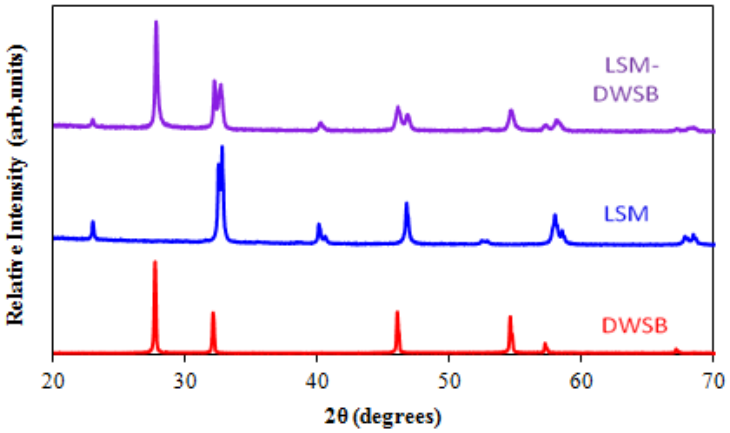

Figure 6.2.6. XRD spectra for DWSB, LSM, and the mixed composite LSM-DWSB

The nano-scale mixing is evident in the images shown in Figure 6.2.7 and Figure 6.2.8 from TEM and SEM observations. Using elemental mapping of a calcined particle on the TEM, there are regions that favor the existence of DWSB (shown with Bi mapping) with an LSM (shown with Mn mapping) coating all over. The bismuth-rich regions correspond with the darker regions in the TEM image showing crystals less than 100nm in diameter that are mixed on the nano-scale with LSM. In the back-scattered condition on the SEM image of the sintered cathode, the light phase corresponds to the DWSB and the darker gray phase represents the LSM. The LSM coats the nano-scale DWSB material which has formed a well sintered network for the LSM particles to adhere to. This supports the theory that the LSM has coated the DWSB on the nano-scale as observed in the TEM.

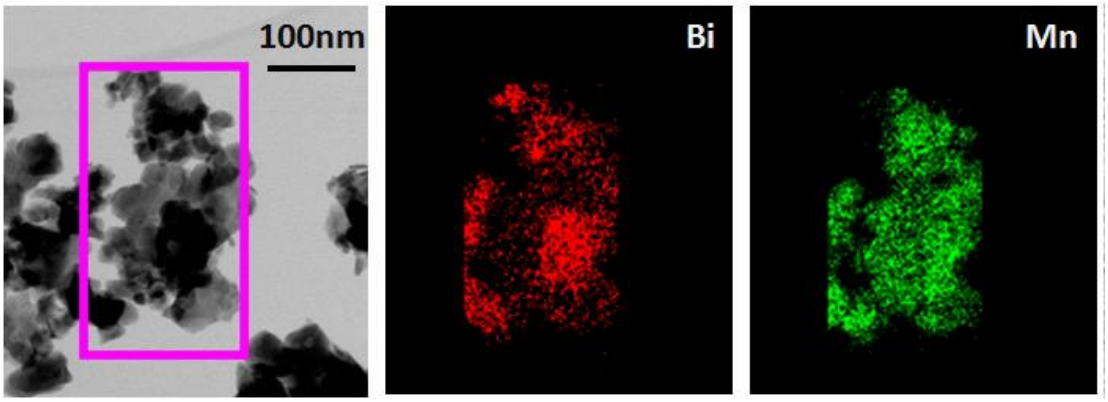

Figure 6.2.7. TEM micrograph and elemental mapping for the presence of bismuth and manganese of the calcined LSM-DWSB powder.

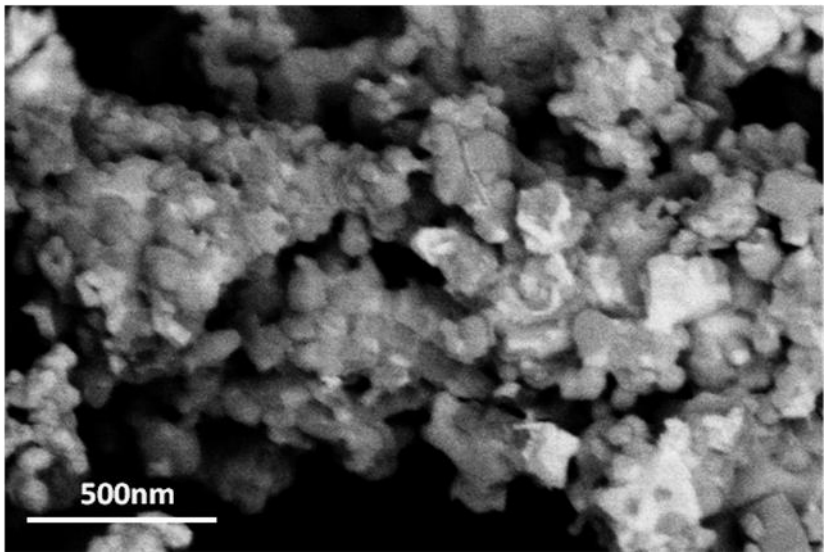

Figure 6.2.8. Back-scattered electron image in the SEM of a sintered LSM-DWSB cathode. The white-gray regions correspond to the DWSB phase and the dark gray regions represent the LSM phase.

6.2.3 EIS Performance

In order to observe the electrochemical performance of these cathodes, symmetric cells prepared as discussed in Chapter 2 were measured in air using electrochemical impedance spectroscopy between the frequencies 0.1 MHz to 0.1 Hz. The results of this measurement are reported as area-specific resistance (ASR) values in Figure 6.2.9 as compared with literature values for LSM and LSM mixed with

other ionic conductors and their improvements by mixing at the nano-scale. Figure 6.2.9 shows the improvement upon our existing work with micron-scale mixed LSM-DWSB using DWSB synthesized in the solid state. This work's ASR value is about a half order of magnitude lower than the solid state case. When observing at the reported values for LSM-GDC and LSM-YSZ in the literature, the same trend is evident: when the ionic conducting phase is on the nano-scale, the ASR value is about a half order of magnitude lower than when the ionic conductor is on the micron scale. This supports the logic that higher surface area cathodes will help increase the oxygen reduction reaction rate due to the extension of the triple phase boundary.

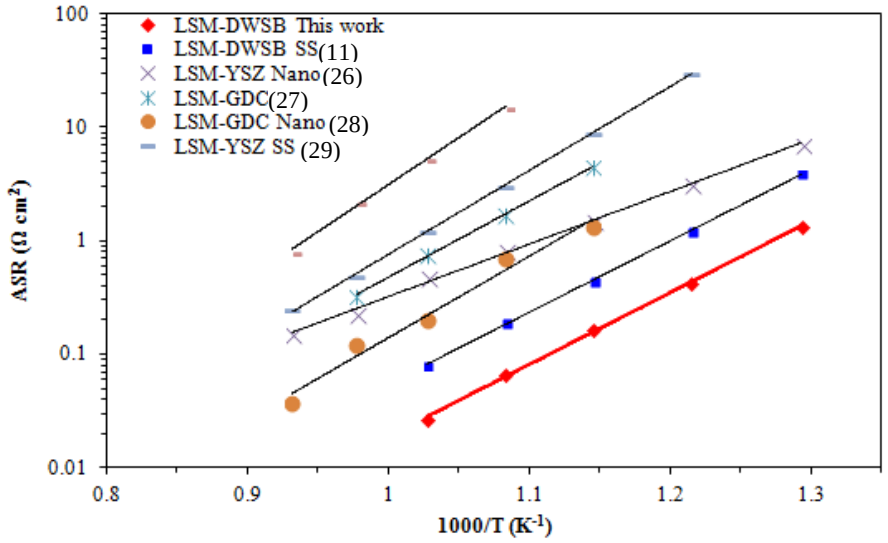

Figure 6.2.9. Comparison of the ASR values from EIS of this work and other LSM and ionic conductor composite cathodes reported in literature (11, 26-29).

The ionic conductivity of the phase incorporated into the LSM cathode also correlates with the ASR value observed. The lower ionic conductivity material at these temperatures reported in Figure 6.2.9 is YSZ, which has an ionic conductivity of 2.8×10^{-3} S/cm at 600 °C (23). When incorporated with LSM, this nano material

also yielded the highest ASR value of 1.5 Ωcm^2 at 600 °C among the three ionic conductors in this figure (26). Similarly, GDC has the next lowest ionic conductivity of $1.5x10^{-2}$ S/cm at 600 °C and DWSB has the highest conductivity of $2.5x10^{-1}$ S/cm at 600 °C (23). When incorporated with LSM, these nano materials yield ASR values of 1.3 Ωcm^2 and 0.17 Ωcm^2 at 600 °C respectively (103). Thus the LSM-DWSB material studied in this work has significantly improved performance over LSM composite cathodes using the conventional ionic conductors YSZ and GDC.

6.2.4 Comparison to LSM/ESB

These results are compared in Figure 6.2.10 with the results of LSM-ESB prepared using the same method in both the 50:50 wt% ratio of LSM to bismuth oxide, like LSM-DWSB synthesized in this work, and the 30:70 ratio recently published (30). Most notably the LSM-DWSB does not outperform the LSM-ESB material. Certainly the ratio of LSM to DWSB (50:50) has not yet been optimized as it was in the LSM-ESB (30:70) work. In Figure 6.2.10, the two cathodes with the 50:50 ratio of LSM to bismuth oxide exhibit very similar results. However, due to the higher conductivity of the ionic conducting species, we did expect to have an improvement over the LSM-ESB case with the same ratio. As demonstrated in previous work the high conductivity of DWSB may quickly degrade (26). Long term stability testing of both the LSM-ESB and LSM-DWSB cathodes may be necessary to determine if there may be underlying stability concerns that inhibit the performance of the LSM-DWSB. However another possibility is that while the ionic conductivity performance of the bismuth oxide used in the cathode may be higher, there may also

be a reduction in oxidation kinetics at the air electrode that could hinder any potential benefit from using a higher conductivity material.

These kinetics were probed using oxygen isotope exchange of both ESB and DWSB. We know LSM has great electronic conductivity but suffers from a high activation energy for the ORR, so the bismuth oxide species is responsible for lowering that activation energy and kinetic information about ESB and DWSB should point to differences in cathode performance. By maintaining the same surface area, we can attribute differences to being intrinsic to the material itself. In Figure 6.2.11, where solid lines represent DWSB curves and dashed lines represent ESB curves, we can see that the critical differences between the two materials arise precisely in the temperature range selected for the ASR measurement. The growing ^{16}O and $^{16}O+^{18}O$ signals demonstrate the exchange of the flowing ^{18}O with the lattice oxygen (^{16}O) as we approach a higher temperature. In comparing the value of these ^{16}O-containing signals in our temperature range, the kinetics are in fact much faster for ESB, indicating that the faster kinetics compensates for the lower ionic conductivity of the ESB. This results in roughly equivalent performance to the LSM-DWSB cathode in the same ratio of LSM to bismuth oxide.

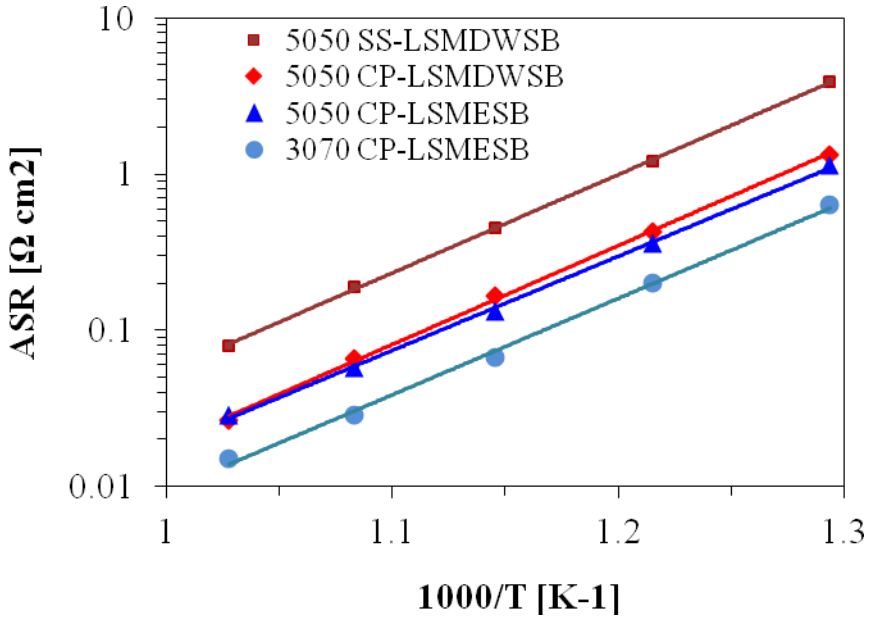

Figure 6.2.10: Comparison of the SS and CP LSM-DWSB materials with LSM-ESB materials with 50/50 wt% of LSM to bismuth oxide. The optimized 30/70 wt% LSM to ESB is included for reference (30).

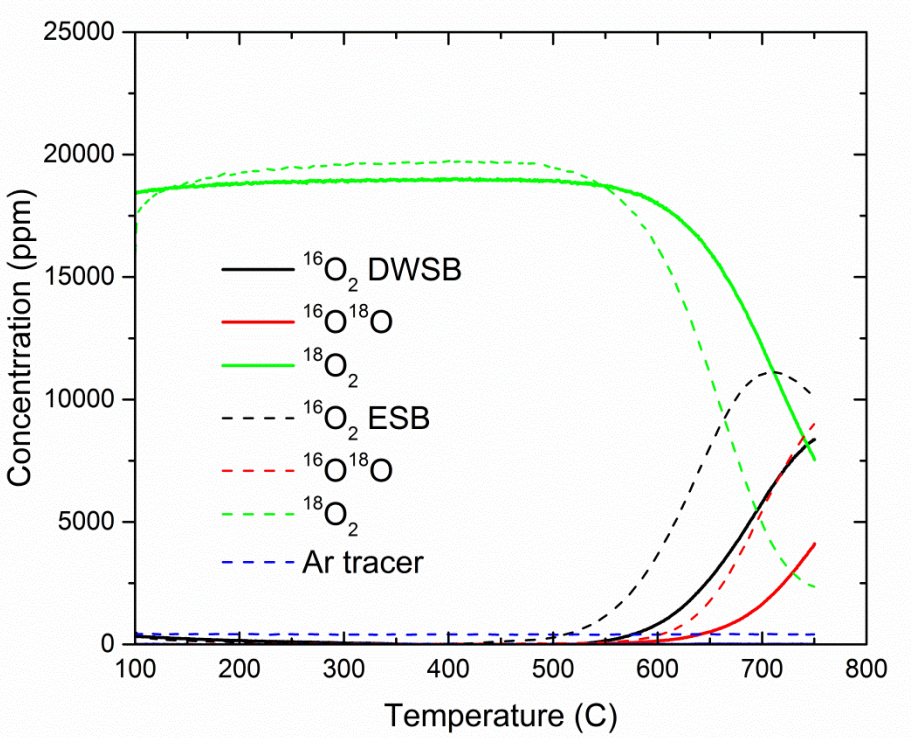

Figure 6.2.11: Results of the oxygen isotope exchange experiments on DWSB (solid lines) and ESB (dashed lines).

6.3 Conclusions

An observed change in activation energy in symmetric cell conductivity was linked to a phase transformation in the DWSB material from the cubic to a monoclinic phase. Any order/disorder transition was masked by this phase change so more work is needed to determined if this doping method may have effectively eliminated the order/disorder transition that plagues the bismuth oxides. Nano-sized DWSB powder was developed using a wet chemical processing method. This powder was the appropriate phase and agglomerates were observed to average 260 nm in diameter while crystal sizes were calculated to be 21.2 nm. Using the glycine-nitrate process, this nano-sized DWSB powder was coated by LSM nanopowder. Using the TEM with the EDS function and SEM under the back-scattered electron condition, the cathode material appears to be well mixed at the nano-scale with a highly desirable microstructure consisting of a DWSB scaffold coated with LSM. EIS measurements of this cathode on a DWSB electrolyte show a half order of magnitude lower ASR value over the solid state, micron-scale mixed cathode (26). Additionally, this LSM-DWSB cathode has much lower ASR value between 500 °C to 700 °C than LSM mixed with conventional YSZ and GDC ionic conductors even when mixed at the nano scale. While outperforming lower ionic conductivity materials incorporated with LSM, this work does not outperform the LSM-ESB synthesized in this same way (30). Oxygen exchange experiments demonstrated that DWSB has slower exchange kinetics than ESB across this temperature range and these kinetics offer reasoning for why the LSM-DWSB did not outperform the LSM-ESB as originally expected.

Chapter 7: Chlorinated Lithium Manganate Spinel

7.1 Introduction

Lithium manganese $AB_2O_{4-d}Cl_d$ materials were synthesized using a glycine nitrate combustion process and evaluated as a cathode for lithium and lithium-ion electrochemical systems. The general formula for the material is $Li_xMn_2O_{4-d}Cl_d$ where $x \approx 1$ and d ranges from 0.012 to 0.025. By incorporating the chlorine during the synthesis of the spinel and generating a high surface area material, the synthesis time can be significantly reduced. The material properties were verified with X-ray diffraction, X-ray fluorescence, Scanning electron microscopy, and Branaur-Emmett-Teller (BET) surface area analysis. Button cells were fabricated to evaluate the thermodynamic and kinetic properties of the $Li//Li_xMn_2O_{4-d}Cl_d$ electrochemical systems.

7.1.1 Spinel Doping Strategies

Lithium manganese oxide spinel is a potential candidate for the replacement of $LiCoO_2$ cathode materials in Li-ion batteries due to its low toxicity, comparable capacity, and low cost (48-50). However, it is plagued by capacity fading due fracturing of the spinel structure either through the Jahn-Teller distortion, loss of crystallinity, or alternative phase formation usually due to non-stoichiometry (52-53). Historically, spinel materials have been doped with b-site dopants of transition metals in order to improve cycle life (104-111). While this method has proven very

effective, this effort proposes to observe if similar benefits can occur from anion doping. Others have also incorporated chlorine, and far more commonly fluorine, and demonstrated positive impacts on performance (110-115). However most of these studies only focus on surface modification while few actually incorporate the halide into the lattice. Additionally, Amatucci et al. showed that capacity gains from $LiMn_2O_{4-d}F_d$ are beneficial but there was negligible impact on cycle life in his experiment (111). Son and Kim also showed that the fluorine doping of the pure spinel did improve the overall capacity, however the cycle life degraded below 87% of the highest capacity after only 20 cycles while the undoped material yielded 98% capacity retention (113). Liu et al. prepared a promising $LiMn_2O_{4-d}Cl_d$ material via a citrate gel method but only measured 10 charge/discharge cycles (112). The present study intends to look more into the cycle life benefits of the less-studied chlorine incorporation into the bulk of the spinel via in-situ combustion synthesis of the material.

7.1.2 Previous Work

Previously chlorine and fluorine were incorporated into the material using solid state processing methods (9). The doping level was varied from z = 0.0 to 0.1 and optimal results were achieved for z = 0.025. Fig. 1.2.1b shows the charge and discharge cycles of this material (reproduced below), which demonstrates the need to raise the charge potential from 4.25V to 4.75V to realize the full charge and discharge capacity (9, 116). Twenty cycles were successfully completed using this chemistry. Additionally, when discharged down to 2.0V, the cell can reversibly charge back up

to the maximum voltage through the two voltage plateaus at 4.1V and 3.0V. This property is of particular interest for military applications due to the possibility of a power need during emergency situations and this work hopes to demonstrate this same cyclability at both the higher and lower voltage regions.

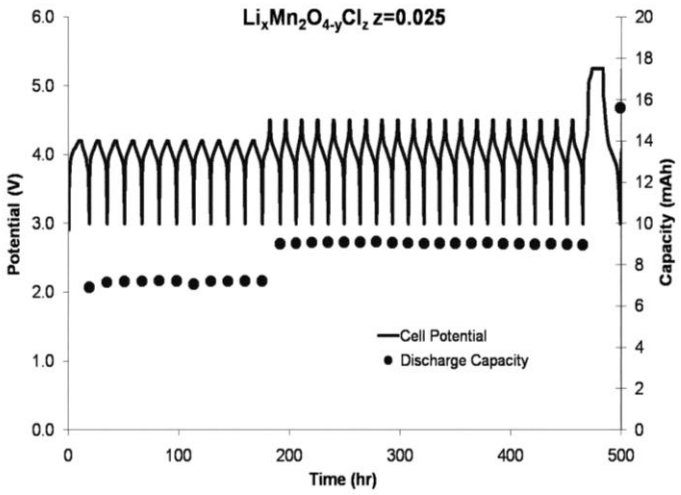

Figure 1.2.1b) Charge/discharge cycling of $Li_xMn_2O_{4-y}Cl_z$ (9),(116)

7.2 Results and Discussion

7.2.1 TGA

Precursor $Li_xMn_2O_{4-d}Cl_d$ (LMO-Cl) was synthesized using the glycine nitrate combustion method discussed in Chapter 2. TGA was performed on the un-fired precursor in air from 30 °C to 750 °C at rate of 10°C per minute to determine the appropriate temperature for calcination. Figure 7.2.1 shows the resultant change in weight percent versus temperature. The precursor material is noticeably hygroscopic when the sample is left at room temperature so a 2% mass increase is observed during the rest at 30 °C prior to measurement (not shown). Between 30 °C and 100 °C, the

mass loss can be attributed to the dehydration of the physically absorbed water molecules. From 200 °C to 300 °C a mass loss is observed and can be attributed to the melting and denitration of remaining nitrates in the precursor via NO_2 evolution. In the 300 °C to 425 °C range, the mass loss could be due to residual glycine decomposition into CO_2, N_2, and H_2O in combination with formation of the spinel (114, 117). Between 450 °C and 500 °C a mass increase occurs, likely due to oxidation. Above 500 °C, the mass loss is likely due to chlorine evolution as shown in the discrepancy between the before and after firing levels of chlorine discussed later.

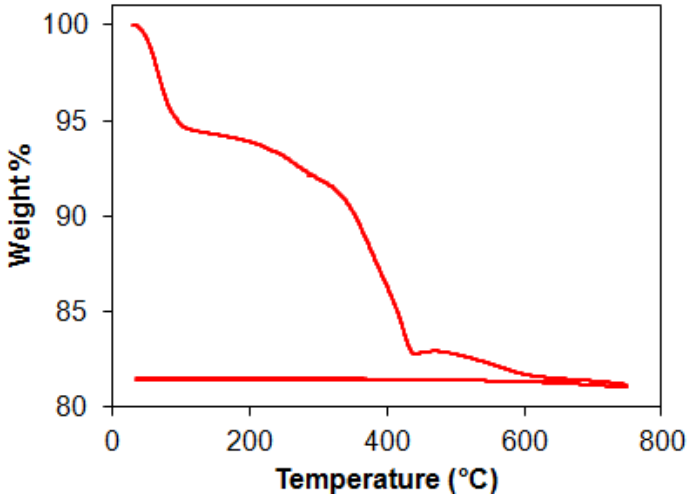

Figure 7.2.1: Thermogravimetric analysis of $Li_xMn_2O_{4-d}Cl_d$ of ash collected from glycine nitrate combustion.

7.2.2 Verifying Phase and Chlorine Presence

X-ray diffraction was used to determine the structure after the material was fired at 600 °C. Figure 7.2.2 shows the diffraction pattern for $Li_xMn_2O_{4-d}Cl_d$ and the corresponding JCPDS file for $LiMn_2O_4$ spinel (PDF 01-070-3120) without the presence of extra peaks signifying the achievement of single phase spinel. Due to the

possibility of nonstoichiometry, a material was synthesized in the same way as the chlorinated spinel only without the addition of $MnCl_2 \cdot 4H_2O$ and is included in Figure 7.2.2. The lattice parameter is calculated to be 8.2066Å and 8.1975Å for the chlorinated and non-chlorinated spinel, respectively. The lattice parameter is greater in the case of $Li_xMn_2O_{4-d}Cl_d$ likely due to the incorporation of the larger Cl^- anion (1.67 Å) in place of O^{2-} (1.26 Å). Additionally, the net positive charge from chlorine doping can be satisfied by reduction of Mn^{4+} to the larger Mn^{3+} cation. To further confirm the presence of chlorine through calcination, x-ray fluorescence spectroscopy (XRF) was used to quantify the elemental components of the material. Figure 7.2.3 shows the resulting XRF profile with a peak present at the corresponding energy for Cl (2.63keV). The calculated value for d in the fired samples ranged from 0.012 to 0.025 for the $Li_xMn_2O_{4-d}Cl_d$ samples synthesized in this work. The Si, P, and S are from the sample holder, and Pd is from the x-ray source. Both of these characterization methods support that the chlorine does in fact survive within the lattice during ash formation and firing and the desired spinel phase can be obtained when incorporating chlorine in-situ with just two hours of firing at just 600 °C. However, it is important to note that the pre-calcination levels of chlorine are significantly greater (about an order of magnitude). During further testing, it was determined that the chlorine level can be tuned as a function of firing time at 600 °C, which is supported by the slow mass loss above 550 °C in TGA. Longer firing times do not completely deplete the chlorine level as chlorine peak presence and quantity in XRF remain constant from 2 hours up to 10 hours of firing time at 600 °C. The evolved chlorine may be due to weak adhesion to the surface while the remaining

chlorine actually incorporated into the lattice. As a result, we selected the 2 hour firing time to keep minimize synthesis time while ensuring any nonstructural chlorine has evolved.

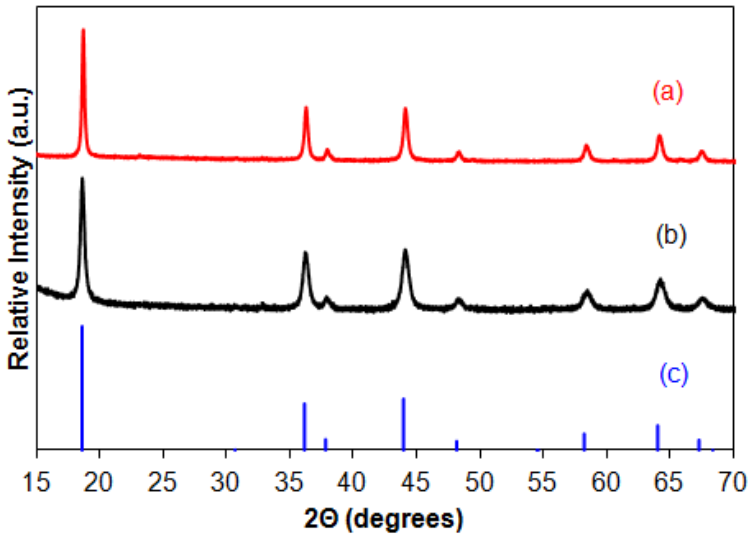

Figure 7.2.2: X-ray diffraction of (a) $Li_xMn_2O_{4-d}Cl_d$ and (b) $Li_xMn_2O_4$ after calcination compared with the (c) JCPDS file for $LiMn_2O_4$ spinel.

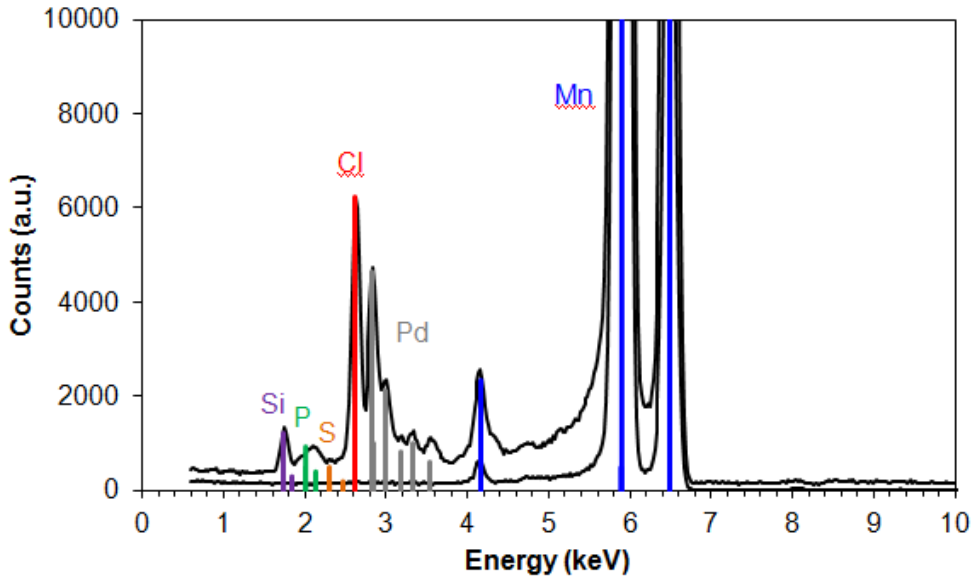

Figure 7.2.3: X-ray fluorescence results of calcined $Li_xMn_2O_{4-d}Cl_d$. The black peaks are the intensities recorded from two detectors. The elemental energies are shown in red for Cl, blue for Mn, gray for Pd (x-ray source), and purple, green, and orange for Si, P, and S respectively (sample holder).

7.2.3 BET Analysis and Particle Morphology

The final spinel material is observed under SEM to view the particle morphology. In Figure 7.2.4, the SEM image shows particles between 1 to 3 microns in size. The inset shows a higher magnification image where the particle surface can be observed. These micron-sized particles actually appear to be large agglomerations of much smaller primary particles, giving rise to the potential for the high surface area we had hoped to achieve for more reaction interfaces once implemented within the experimental cell. BET results confirm this showing an estimated particle size of 561 nm based on the measured surface area of 2.46 m^2/g. The BET particle size is smaller than what we see in the SEM images because the BET calculation assumes perfectly spherical particles. This means that a higher surface area would result in a calculated particle size smaller than the true particle

size because of surface roughness. The particles we formed have a much higher surface area than a smooth spherical particle of its particle diameter.

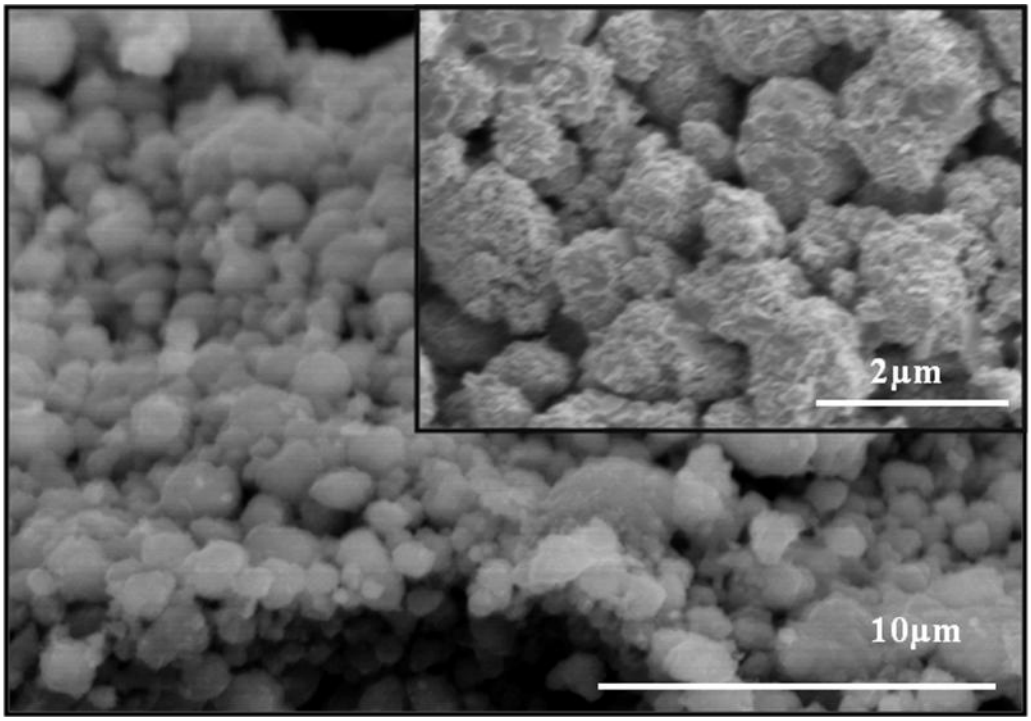

Figure 7.2.4: SEM micrograph of the calcined $Li_xMn_2O_{4-d}Cl_d$ powder. The inset presents a higher magnification to show surface morphology of the powder.

7.2.4 Cell Performance

The $Li_xMn_2O_{4-d}Cl_d$ active material was mixed into a cathode with PTFE and carbon black and incorporated into experimental button cells opposite a lithium metal anode and cycled from 4.75V to 3.5V at 1mA/cm^2. The first ten cycles, with the subsequent specific charge and discharge capacities are shown versus time in Figure 7.2.5. The higher charge capacity and plateau at 3.8V upon discharge of the first cycle is typical for a forming cycle. The initial overcharge becomes minimal after the second cycle and the remaining 8 cycles maintain a discharge capacity of 85.1 mAh/g. Figure 7.2.6 shows the first three cycles plotted as differential capacity,

clearly showing the initial forming cycle with an irreversible reaction at about 3.8V upon discharge. Differential capacity uses the galvanostatic control of the electrochemical cell and plots the capacity increase (charge) or decrease (discharge) as a function of potential. This is generated from the capacity measurements during charge and discharge and provides information similar to cyclic voltammetry (55).

Figure 7.2.7 shows the charge and discharge capacity up to 130 cycles where overcharge begins to impact the cell leading to eventual failure at cycle 180 (not shown). While this may indicate limitations in the active material itself, the cell is able to maintain greater than 95% of its discharge capacity over the 130 cycles as shown in Figure 7.2.8. Because the discharge capacity shows minimal loss, the active material appears robust enough to continue cycling. However, due to the higher starting voltage the $LiPF_6$ electrolyte is not sufficiently stable and might be causing the cell to fail prematurely. Yang et al. shows that above 4.5V, $LiPF_6$ with EC/DMC/DEC will oxidize at the surface of the electrode (118). One way to address this would be to charge to 4.5V rather than 4.75V as negligible capacity gain is seen in voltages above 4.5V. Additionally, as shown in Figure 7.2.6, no electrochemical activity is seen above 4.5V. Alternatively, this can be addressed through the incorporation of a more advanced high voltage compatible electrolyte, which is beyond the scope of the current investigation.

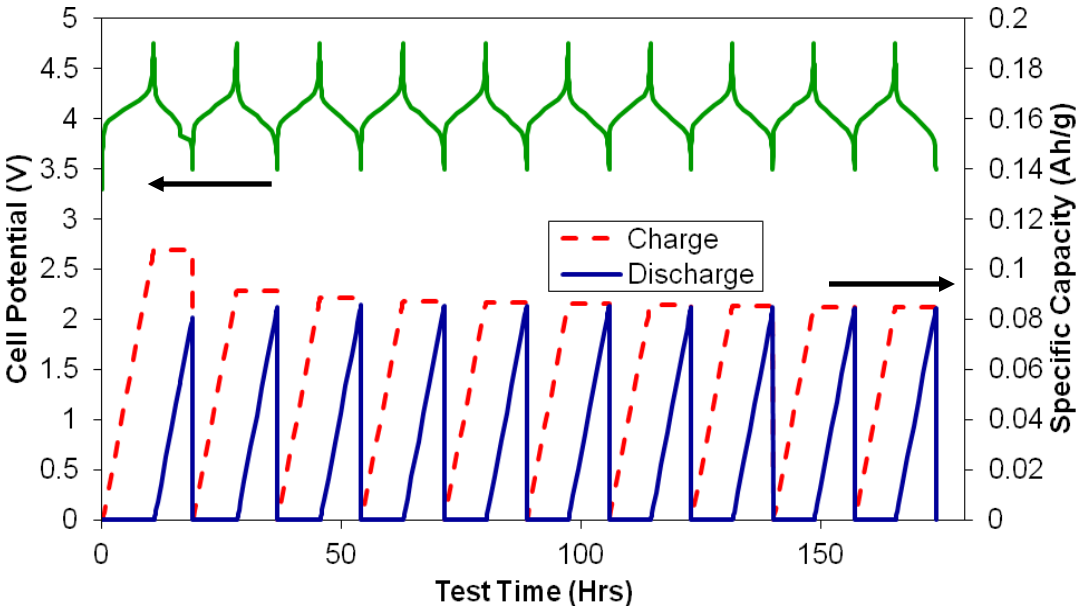

Figure 7.2.5: Voltage profile (top) and specific charge and discharge capacities (bottom) for the first ten charge/discharge cycles of the $Li_xMn_2O_{4-d}Cl_d$ experimental cells.

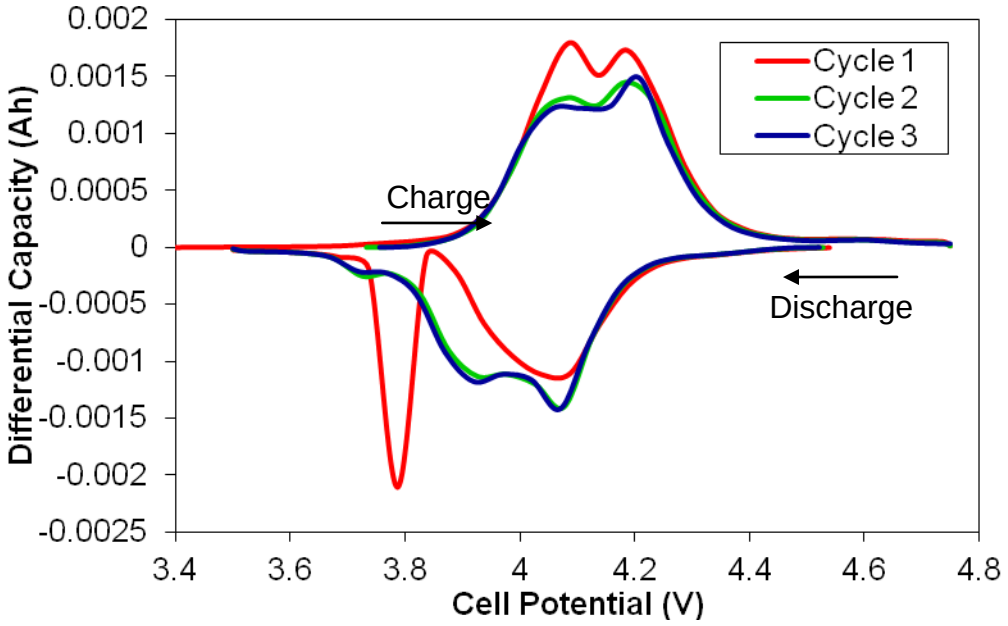

Figure 7.2.6: Differential capacity curves for the first 3 charge/discharge cycles of the $Li_xMn_2O_{4-d}Cl_d$ experimental cells.

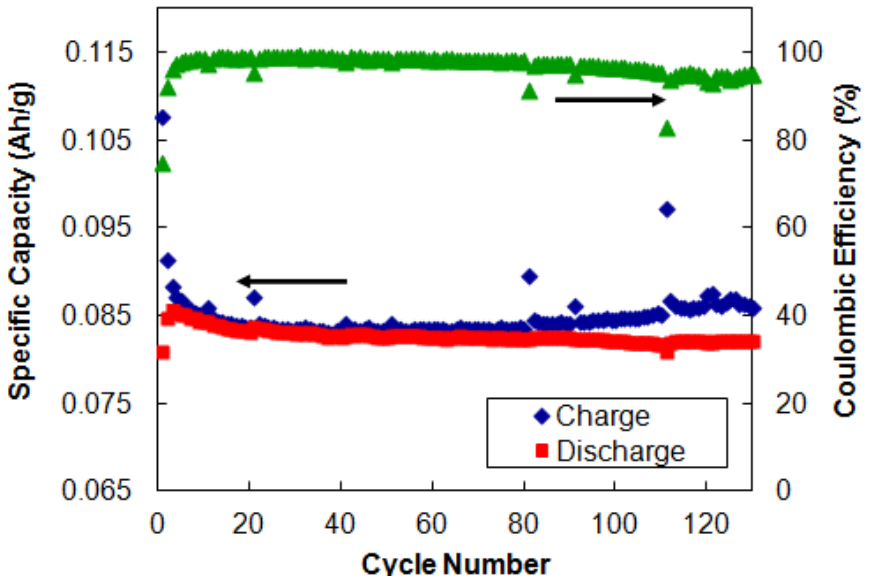

Figure 7.2.7: Specific capacity (bottom) and coulombic efficiency (top) during 130 charge/discharge cycles of the $Li_xMn_2O_{4-d}Cl_d$ experimental cells.

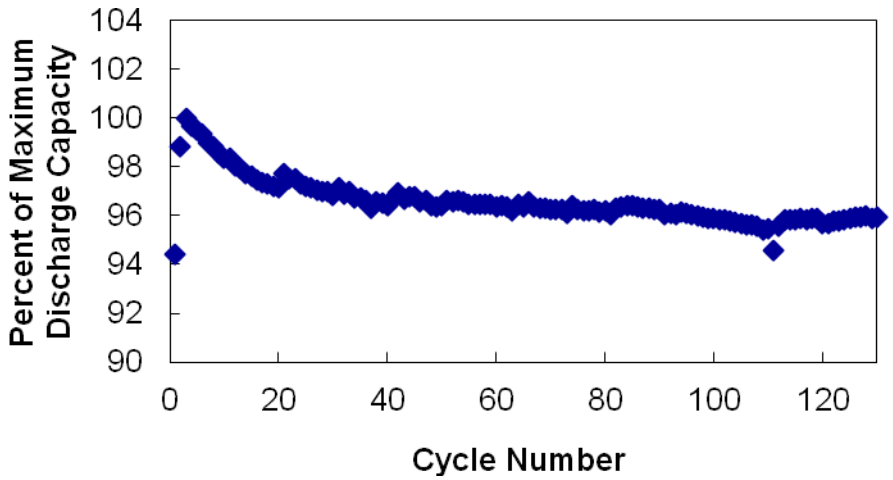

Figure 7.2.8: The percent of discharge capacity retention over 130 cycles.

In Figure 7.2.9 every tenth cycle up through 130 cycles is displayed in terms of differential capacity. The two oxidation and reduction peaks are typical for this spinel material and can be indexed to represent the equilibrium between λ-$Mn0_{2-d}Cl_d$ – $Li_{0.5}Mn_2O_{4-d}Cl_d$ and $Li_{0.5}Mn_2O_{4-d}Cl_d$ – $Li_xMn_2O_{1-d}Cl_d$ as the lithium is inserted or deinserted into the lattice (119). $Li_{0.5}Mn_2O_{4-d}Cl_d$ is the likely intermediate material due to a similar value for the area under the curve of the two peaks. As the number of

cycles increase, the peaks begin shifting to higher voltage upon charge and lower voltage upon discharge with peak broadening in the lower voltage regime, correlating with the degradation in coulombic efficiency. As discussed previously, this may be due to the formation of an oxide as the electrolyte interacts with the electrode at high voltages. It is also possible that the active material may have some slight structural changes over the course of cycling that could be leading to a diminished capacity or preferences for site occupancy. This would need to be studied further through structural analysis at various cycle values.

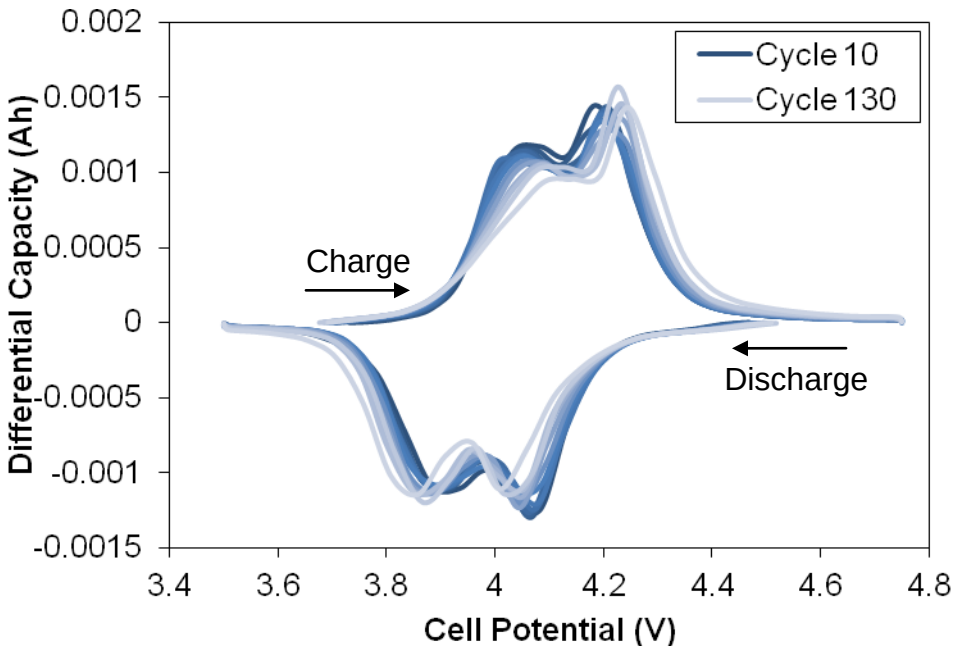

Figure 7.2.9: Differential capacity curves for every tenth cycle up to 130 cycles.

7.3 Conclusions

In-situ chlorination of the spinel is shown to be successful in preventing full evolution of the incorporated chlorine during post-processing of the precursor

material. Additionally, a high surface area material using basic ceramic processing techniques was achieved to extend the lithium insertion and deintersion interfaces. A full experimental cell can be fabricated in less than 8 hours from the mixture of the raw materials for the spinel. These cells exhibited long cycle life with greater than 95% of the highest discharge capacity achieved at cycle 130 with 82.3 mAh/ with no addition of B-site doping of transition metals.

Chapter 8: Chlorinated Lithium Manganate Spinel Containing Iron B-site Doping

8.1 Introduction: Improved cycle life via iron doping

Lithium manganese $AB_2O_{4-d}Cl_d$ materials were synthesized using a glycine nitrate combustion process and evaluated as a cathode for lithium and lithium-ion electrochemical systems. The general formula for the material is $Li_xMn_{2-y}Fe_yO_{4-z}Cl_z$ where $x \approx 1$, y ranges from 0.137 to 0.195 and z ranges from 0.014 to 0.028. By incorporating the chlorine and B - site iron doping during the synthesis of the spinel and generating a high surface area material, the synthesis time can be significantly reduced. The material properties were verified with x-ray diffraction, x-ray fluorescence, scanning electron microscopy, and Branaur-Emmett-Teller (BET) surface area analysis. Button cells were fabricated to evaluate the performance of the Li// $Li_xMn_{2-y}Fe_yO_{4-z}Cl_z$ electrochemical systems.

8.1.1 Background

Lithium manganese oxide spinel is a potential candidate for lithium-ion battery cathodes due to its low toxicity, comparable capacity, and low cost (48-50). However, this spinel suffers from capacity fading due to fracturing of the structure either through the Jahn-Teller distortion, alternative phase formation via non-stoichiometry, or loss of crystallinity (52-54). Historically, cycle life enhancements have been achieved by stabilizing the spinel structure through transition metal doping on the B - site of the lattice (104-111, 115). Iron as a dopant is of interest due partly

to its low toxicity but primarily its low cost. By adding the redox couple of this transition metal, this spinel can satisfy higher voltage (5.0 V) applications should compatible electrolytes be produced (120-122). Utilizing spray pyrolysis, Taniguchi and Bakenov demonstrate an increased capacity retention of $LiMn_{2-x}Fe_xO_4$ versus the undoped $LiMn_2O_4$ spinel over 100 cycles (123).

While b-site doping has proven moderately effective, this effort proposes to observe if cycle life can be even further enhanced in $Li_xMn_{2-y}Fe_yO_4$ (LMFO) by also incorporating anion dopants. Previously our group has incorporated chlorine and fluorine into the base $LiMn_2O_4$ material using solid state processing methods and demonstrated cyclability to 32 cycles (9, 116) due to the weakening of the Li-O bonds that allows for ease of lithium mobility. Others have also added chlorine and more commonly fluorine and demonstrated performance enhancements (106, 110-113). However rather than incorporating the halide into the lattice, most studies focus on surface modification of the spinel. Liu et al. did prepare a promising $LiMn_2O_{4-z}Cl_z$ material via a citrate gel method but only measured 10 charge/discharge cycles (112). In the case of fluorine, Amatucci et al. showed that while capacity gains from $LiMn_2O_{4-z}F_z$ are beneficial there was negligible impact on cycle life in his experiment (111). Son and Kim also showed that the fluorine doping of the pure spinel did improve the capacity, however the discharge capacity degraded below 87% of the highest capacity after only 20 cycles in the doped case (113).The present study intends to look more into the cycle life benefits of the less-studied chlorine incorporation into the bulk of an iron-doped spinel via *in situ* combustion synthesis of the material.

8.2 Results and Discussion

8.2.1 Thermal Gravimetric Analysis

TGA was performed in air from 30 °C to 750 °C at a rate of 10 °C per minute to determine the ideal calcination temperature. Figure 8.2.1 shows the resultant curve of weight percent with temperature. Between 30 and 120 °C, the mass loss can be attributed to the dehydration of the physically absorbed water molecules. From 200 to 300 °C a mass loss is observed and can be attributed to the melting and denitration of remaining nitrates in the precursor via NO_2 evolution. In the 300 to 400 °C range, the mass loss could be due to residual glycine decomposition into CO_2, N_2, and H_2O in combination with formation of the spinel (114, 117). Between 400 and 500 °C a slight mass increase occurs, potentially due to oxidation. Above 500 °C, the mass loss is most likely due to chlorine evolution as shown in the discrepancy between the before and after firing levels of chlorine determined through XRF and is discussed later.

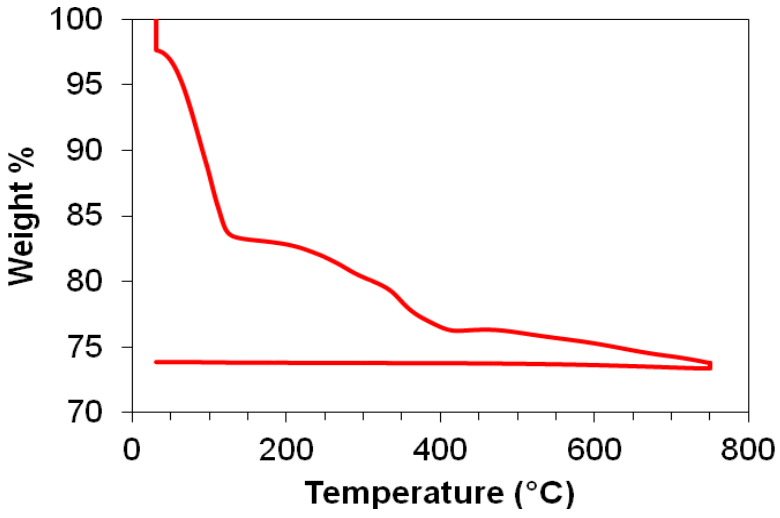

Figure 8.2.1: Thermal gravimetric analysis of $Li_xMn_{2-y}Fe_yO_{4-z}Cl_z$ ash collected from glycine nitrate combustion.

8.2.2 Chemical and Structural Analysis

After the material was fired, x-ray diffraction was used to determine the crystalline structure. Figure 8.2.2 shows the diffraction pattern for $Li_xMn_{2-y}Fe_yO_{4-z}Cl_z$ and the corresponding JCPDS file for $LiMn_2O_4$ spinel (PDF 01-070-3120) showing a majority single phase spinel but with the additional presence of Mn_2O_3. This can be eliminated by increasing the amount of lithium-containing precursor. A pure phase material is demonstrated in additional batches of LMFO-Cl material and included in Figure 8.2.2(b). Due to the possibility of non-stoichiometry, $LiMn_2O_{4-z}Cl_z$ was fabricated using the same processing method without the addition of $FeCl_3$ and is included in Figure 8.2.2(c). Most importantly, the desired spinel phase is formed with the present synthesis method without iron or chlorine-containing crystalline species forming but rather incorporating into the lattice via solid solution. In order to confirm the preservation of chlorine through calcination, x-ray fluorescence spectroscopy (XRF) was used to quantify the elemental components of the material. Figure 8.2.3 shows the resulting XRF profile with a peak present at the corresponding energy for Cl (2.63 keV), Mn (5.90, 6.49, 4.16 and 4.74 keV) and Fe (6.40 and 7.06 keV). The calculated value for *y* in three different fired powders were 0.137, 0.159, and 0.195 and the calculated value for *z* in the same three powders were 0.014, 0.022, and 0.028 respectively for the $Li_xMn_{2-y}Fe_yO_{4-z}Cl_z$ samples synthesized in this work. The Si, P, and S are from the sample holder, and Pd is from the x-ray source. Both of these characterization methods support that the chlorine does in fact survive within the lattice without secondary phases during ash formation and firing and the desired spinel phase can be obtained when

incorporating chlorine in-situ with just two hours of firing at just 600 °C. However, it is important to note that the pre-calcination levels of chlorine as measured through XRF are significantly greater by about an order of magnitude. During further testing, it was determined that the chlorine level can be tuned as a function of firing time at 600 °C, which is supported by the slow mass loss above 550 °C in TGA.

Longer firing times do not completely deplete the chlorine level as chlorine peak presence and quantity in XRF remain constant from two hours up to 10 hours of firing time at 600 °C. The evolved chlorine may be due to weak adhesion to the surface while the remaining chlorine is actually incorporated into the lattice. As a result, the two-hour firing time was selected to minimize processing time while ensuring the possible nonstructural chlorine has evolved.

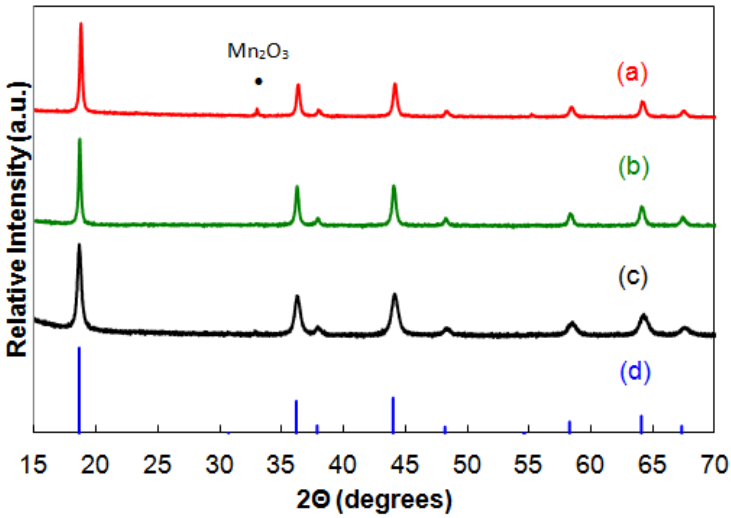

Figure 8.2.2: X-ray diffraction of (a) $Li_xMn_{2-y}Fe_yO_{4-z}Cl_z$, (b) $Li_xMn_{2-y}Fe_yO_{4-z}Cl_z$ with increased amount of lithium nitrate precursor eliminating Mn_2O_3 peak, and (c) $Li_xMn_2O_4$ after calcination compared with the (d) JCPDS file for $LiMn_2O_4$ spinel.

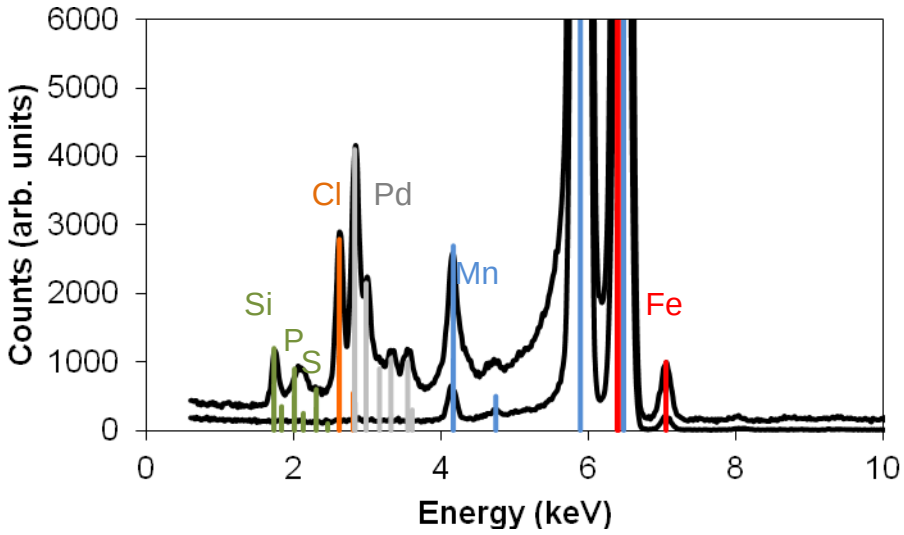

Figure 8.2.3: X-ray fluorescence results of calcined $Li_xMn_{2-y}Fe_yO_{4-z}Cl_z$. The black peaks are the intensities recorded from two detectors. The elemental energies are shown in blue for Mn, orange for Cl, red for Fe, gray for Pd (x-ray source), and green for Si, P, and S (sample holder).

8.2.3 Morphology

Morphologically the material is desired to be in the nanoscale in order to take advantage of short diffusion paths for Li^+ that may improve the cycle life of the material. BET surface area analysis results show that the material has a high surface area of 8.48 m^2/g through this synthesis method with a calculated particle size of 161 nm and pore size of 14 nm. This particle size corresponds to the approximate primary particle size we can resolve in the SEM image shown in Figure 8.2.4. The pore size is important for forecasting the rate capability of the material as porosity facilitates the transport of Li^+ ions (124). A recent and thorough study by Pico et al. prepared the non-chlorinated LMFO using five different methods yielding specific surface areas of 5 to 11 m^2/g and pore sizes between 3 to 5 nm (121). We achieved a similar surface area, but the roughly 3-fold increase in pore diameter through the synthesis described in this work should improve the rate capability beyond the promising results demonstrated by Pico et al.

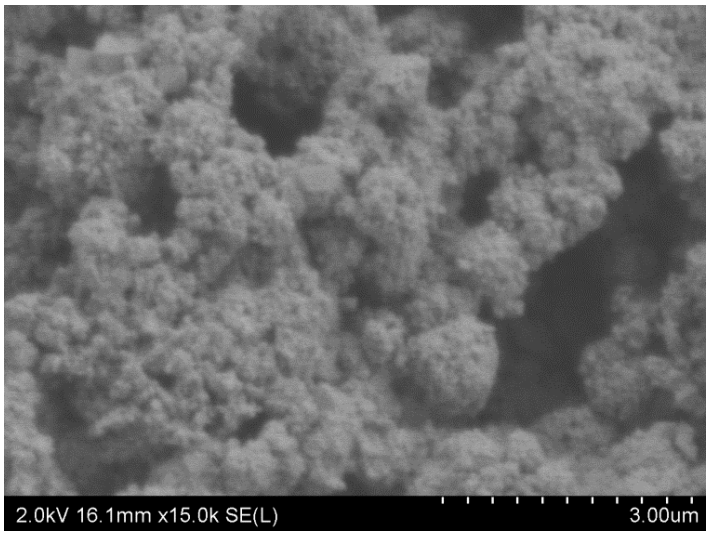

Figure 8.2.4: SEM micrograph of $Li_xMn_{2-y}Fe_yO_{4-z}Cl_z$ as calcined showing the nano-sized primary particles synthesized

8.2.5 Electrochemical Performance y = 0.137 and z = 0.014

The $Li_xMn_{2-y}Fe_yO_{4-z}Cl_z$ active material was mixed into a cathode with PTFE and carbon black and incorporated into experimental button cells opposite a lithium metal anode and cycled from 4.75 V to 3.5 V, 4.5 V to 3.5 V or 4.5 V to 2.25 V, at 1.0 mA/cm^2 or 2.0 mA/cm^2. Figures 8.2.5 to 8.2.8 display electrochemical performance data for $Li//Li_xMn_{2-y}Fe_yO_{4-z}Cl_z$ cells with a stoichiometry where y = 0.137 and z = 0.014. The first ten cycles, with the subsequent specific charge and discharge capacities are shown versus time in Figure 8.2.5. The higher charge capacity and plateau at 3.8V upon discharge of the first cycle is typical for a forming cycle. The initial overcharge becomes minimal after the second cycle and the remaining 8 cycles maintain a discharge capacity of 92 mAh/g. Figure 8.2.6 illustrates the first three cycles plotted in differential capacity and shows the initial forming cycle with an irreversible reaction at about 3.8V upon discharge. Differential capacity uses galvanostatic control of the electrochemical cell and plots the capacity

increase (charge) or decrease (discharge) as a function of potential. This is generated from the capacity measurements during charge and discharge and provides information similar to cyclic voltammetry (55). The two cycles following the forming cycle are representative of typical spinel structure and coincide with each other, indicating the forming reaction has completed. Figure 8.2.7 displays cycles 11-30 for a Li//$Li_xMn_{2-y}Fe_yO_{4-z}Cl_z$ cycled between 4.5 and 3.5 V at 1.0 mA/cm^2. The cell was previously subjected to a 4.75 V to 3.5 V charge and discharge at 1.0 mA/cm^2 for ten cycles shown in Figure 8.2.5. However due to the fact that the iron redox couple isn't accessible below 5.0 V, it was considered unnecessary to continue cycling at 4.75 V. This decision took into consideration the voltage degradation characteristics of the $LiPF_6$ with EC/DMC/DEC electrolyte that demonstrates oxidation at the surface of the electrode above 4.5 V (118, 125). This can be addressed through the incorporation of a more advanced high voltage compatible electrolyte, which is beyond the scope of the current investigation. The discharge capacity is very consistent up to 30 cycles with a capacity of 88.9 mAh/g at cycle 11 and 87.9mAh/g at cycle 30, a loss of just 1.1%. Due to the overcharge on cycle 30, it was excluded from the differential capacity curves in Figure 8.2.8. Again (as previously stated) this graph demonstrates the very consistent cyclability of the experimental cell as evidenced by the overlapping curves. Unfortunately, the overcharge on cycle 30 predicted a short in the cell and it was removed from testing on cycle 33.

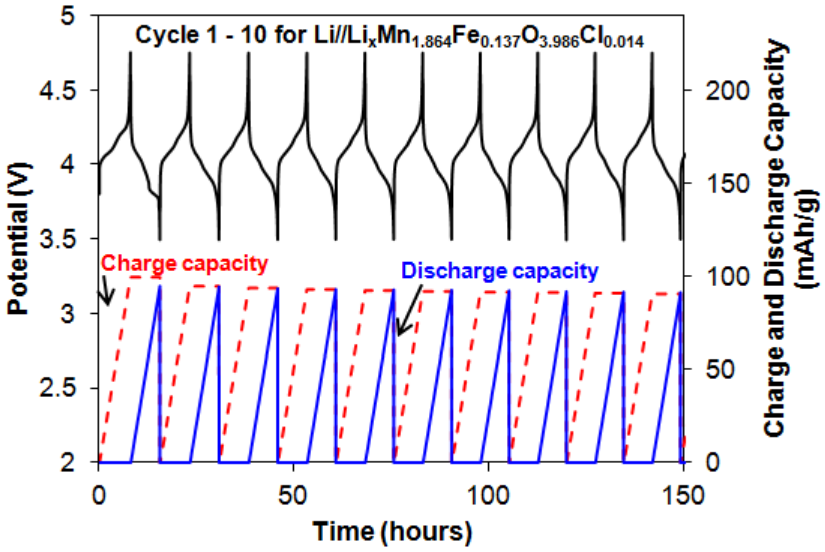

Figure 8.2.5: Voltage profile (top) and specific charge and discharge capacities (bottom) for the first ten charge/discharge cycles of the $Li_xMn_{2-y}Fe_yO_{4-z}Cl_z$ experimental cell for y = 0.137 and z = 0.014.

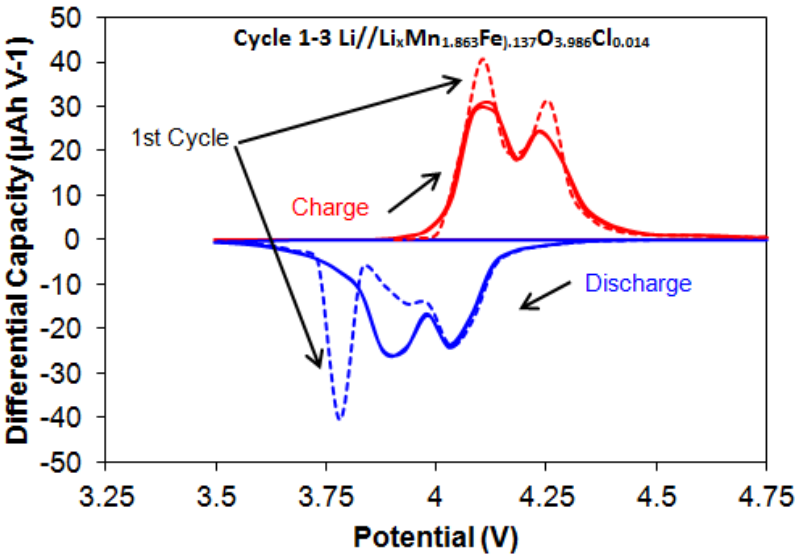

Figure 8.2.6: Differential capacity curves for the first three charge/discharge cycles of the $Li_xMn_{2-y}Fe_yO_{4-z}Cl_z$ experimental cell for y = 0.137 and z = 0.014 including the forming cycle shown in a dashed line.

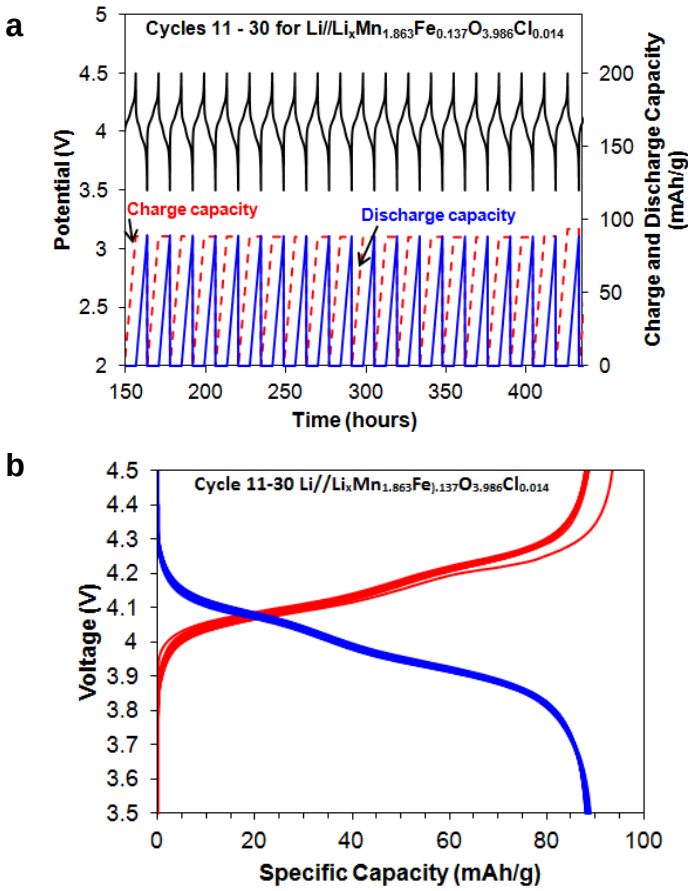

Figure 8.2.7: a) Voltage profile (top) and specific charge and discharge capacities (bottom) for charge /discharge cycles 11-30 and b) charge (red)/discharge (blue) curves for cycles 11-30 of the $Li_xMn_{2-y}Fe_yO_{4-z}Cl_z$ experimental cell for y = 0.137 and z = 0.014.

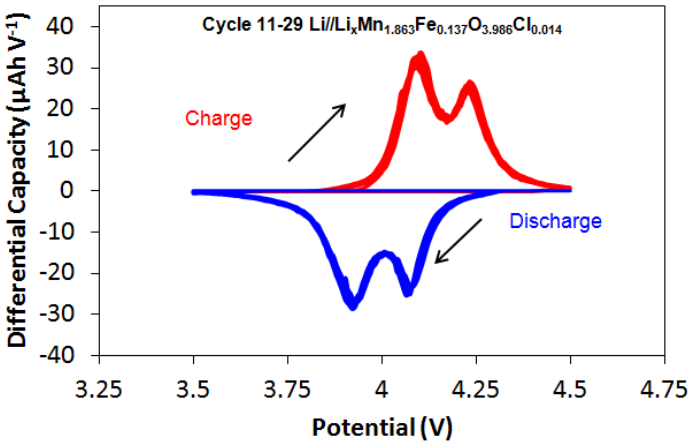

Figure 8.2.8: Differential capacity curves for charge/discharge cycles 11-29 cycles of the $Li_xMn_{2-y}Fe_yO_{4-z}Cl_z$ experimental cell for y = 0.137 and z = 0.014.

8.2.6 Electrochemical Performance y = 0.195 and z = 0.028

Figures 8.2.9 - 8.2.11 display electrochemical performance data for $Li//Li_xMn_{2-y}Fe_yO_{4-z}Cl_z$ cells with a stoichiometry where y = 0.195 and z = 0.028. Figure 8.2.9 shows the charge and discharge capacity and coulombic efficiency up to 250 cycles where shorting begins to become severe. At cycle 250, the discharge capacity is better than 98% of the original discharge capacity. In Figure 8.2.10 the discharge capacity for 300 cycles is shown where the cell has survived shorting and exhibited a normal cycle with a change in scale to amplify any variances in capacity. Excluded from this figure is cycle 286 (shown in Figure 8.2.14) as the cell was deep discharged from 4.5 to 2.25 V. For all surviving cycles, the discharge capacity remains above 94% of the original capacity, with cycle 300 exhibiting 98% of the original capacity. Because the discharge capacity of both cells where y = 0.195 and y = 0.137 show minimal loss, the active material is robust enough to continue cycling, thus the electrolyte may be leading to the degradation of the cell. Additionally, our experimental cell fabrication incorporates a nonwoven glass separator that acts as a wick rather than a true separator that could prevent shorting through dendritic growth. However once the short is alleviated, the cell is able to return to normal function. This demonstrates that the chemistry of the designed cathode is sound but alternative cell fabrication is necessary to observe the optimal capability of the material. This indicates that the cathode is likely to survive greater than 300 cycles with less than 2% capacity fade should an effective electrolyte and separator be used.

While the capacity of the material remains intact, there is a gradual change in shape and a voltage shift of the differential capacity curves from cycle 5 through 300, shown in Figure 8.2.11. This behavior is typical for electrolyte degradation with high

voltage spinel cathodes as well as deformation of the spinel structure (126-127). However, because the discharge capacity suffers minimal loss in surviving cycles, the lithium insertion and deinsertion appears to remain reversible. This indicates that the structural changes may not be impeding the lithium pathways and electrolyte degradation may be the primary mechanism. More experimentation with cells capable of being disassembled would be necessary in order to externally monitor structural changes after cycling at various lengths.

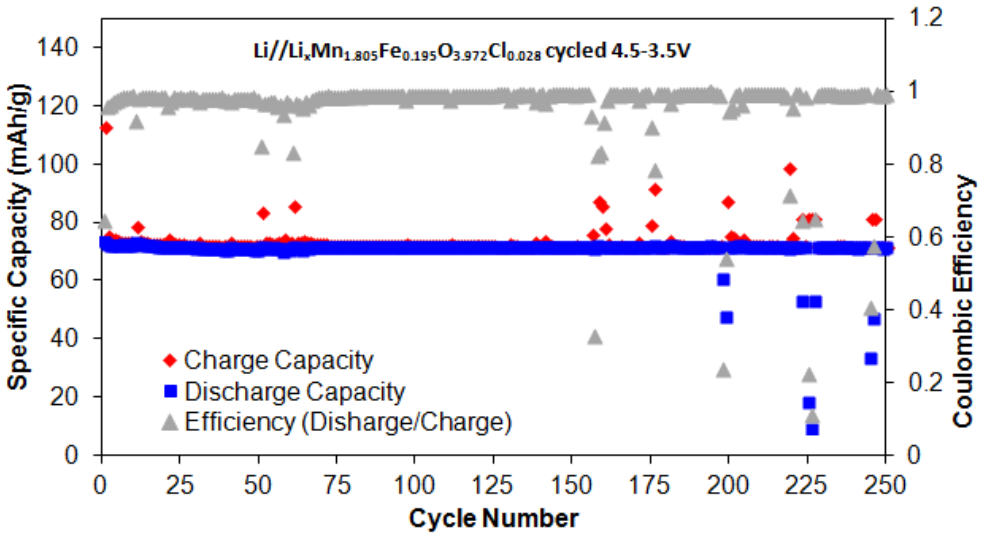

Figure 8.2.9: Specific capacity (bottom) and coulombic efficiency (top) during 250 charge/discharge cycles of an $Li_xMn_{2-y}Fe_yO_{4-z}Cl_z$ experimental cell for y = 0.195 and z = 0.022.

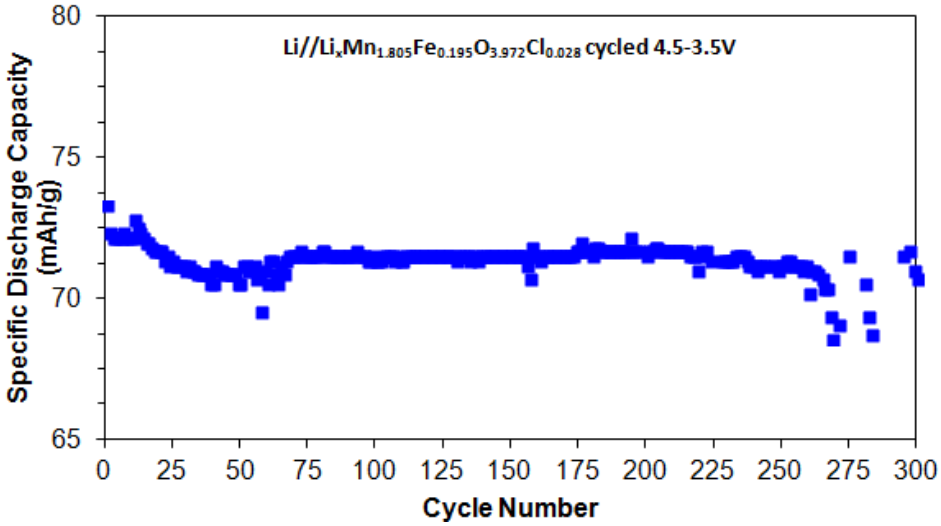

Figure 8.2.10: Specific discharge capacity of surviving cycles from 1-300 of an $Li_xMn_{2-y}Fe_yO_{4-z}Cl_z$ experimental cell for y = 0.195 and z = 0.022.

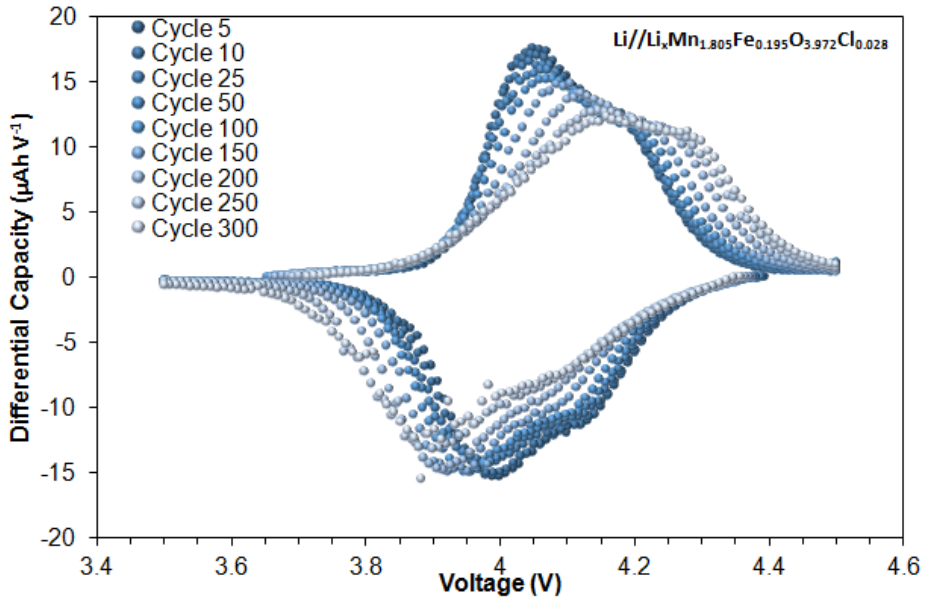

Figure 8.2.11: Differential capacity curves for cycles 5, 10, 25, 50, 100, 150, 200, 150, and 300 of an $Li_xMn_{2-y}Fe_yO_{4-z}Cl_z$ experimental cell for y = 0.195 and z = 0.022.

8.2.7 Performance during deep discharge to 2.25 V

Figures 8.2.12 - 8.2.13 display electrochemical performance data for two separate cells of the same stoichiometry of $Li//Li_xMn_{2-y}Fe_yO_{4-z}Cl_z$ where y = 0.159 and z = 0.022. The first ten cycles at 4.5V to 3.5V at 2mA/cm^2 is shown in Figure 12 with the forming cycle shown in the dotted line. Cycle 11 (dashed line) was

performed to demonstrate the ability of the cell to discharge down to 2.25 V at 2.0 mA/cm^2 and recharge completely to 4.5V. This shows the reversibility of the lower voltage chemistry. Figure 8.2.13 illustrates the first 3 cycles, excluding the forming charge, of a separate cell where the cell was cycled between 4.5 V and 2.25 V at 2.0 mA/cm^2 again demonstrating the reversibility of the reaction at the lower voltages. In order to determine if this deep discharge is possible at advanced cycle life and if it has negative impacts on future capacity loss, the experimental cell of $Li_xMn_{2-y}Fe_yO_{4-z}Cl_z$ for $y = 0.195$ and $z = 0.022$ was discharged down to 2.25 V at cycle 286. Even during a period of several shorting events, cycles 299 and 300 overlap and exhibit 98% capacity as mentioned before. All of the cells shown in Figures 8.2.12 - 8.2.14 exhibited a discharge capacity of 145 - 150 mAh/g during the discharge to 2.25 V. This ability to obtain additional discharge capacity is a desirable trait for military applications where more capacity may be required in dire circumstances. The cell will be able to recharge again for future normal use should new replacement cells be inaccessible.

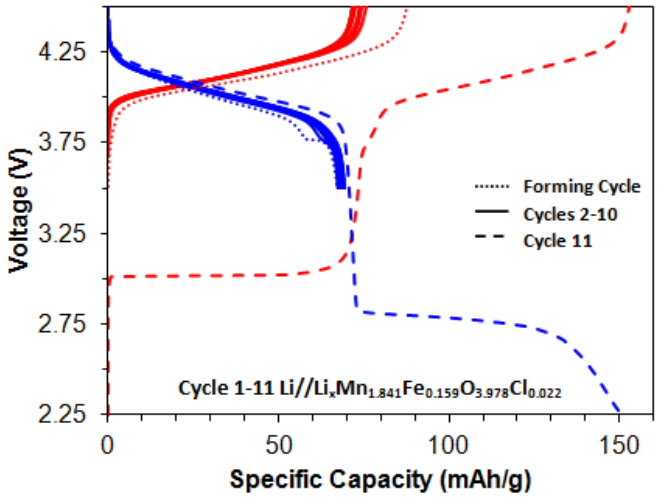

Figure 8.2.12: Charge(red) /discharge (blue) curves for cycles 1-11 of an $Li_xMn_{2-y}Fe_yO_{4-z}Cl_z$ experimental cell for y = 0.159 and z = 0.022. Dotted line indicates the forming cycle, solid line includes cycles 2-10 and the dashed line is cycle 11 demonstrating a full deep discharge to 2.25 V at 2.0 mA/cm^2.

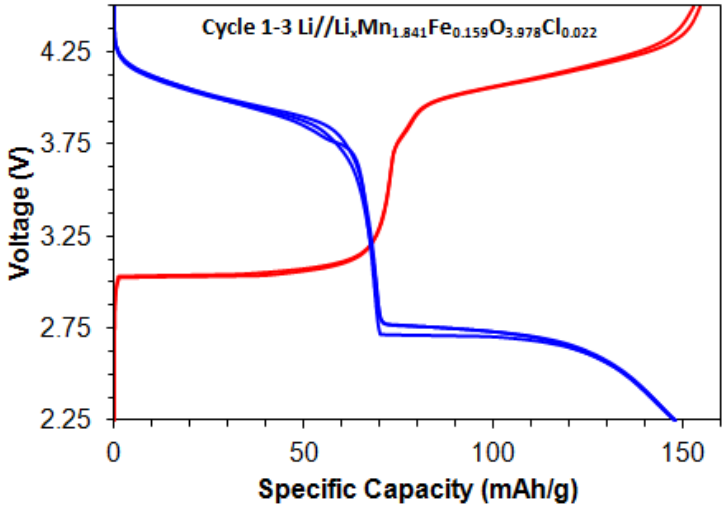

Figure 8.2.13: Charge (red) /discharge (blue) curves for cycles 1-3 of an $Li_xMn_{2-y}Fe_yO_{4-z}Cl_z$ experimental cell for y = 0.159 and z = 0.022 excluding the forming charge. Cell cycled deep from 4.5V to 2.25 V at 2.0 mA/cm^2.

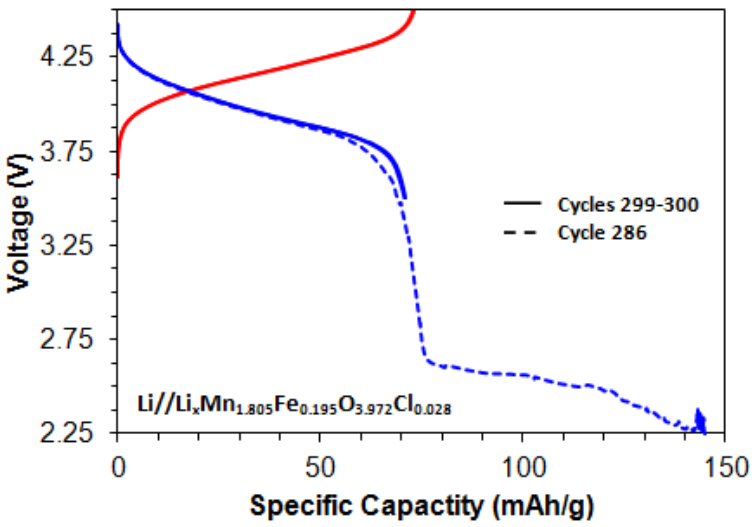

Figure 8.2.14: Discharge (dashed) curve for cycle 286 and charge (red) /discharge (blue) curves for cycles 299 - 300 of an $Li_xMn_{2-y}Fe_yO_{4-z}Cl_z$ experimental cell for y = 0.195 and z = 0.028.

8.3 Conclusion

A nanoscale $Li_xMn_{2-y}Fe_yO_{4-z}Cl_z$ material was synthesized in three different compositions and desirable phase and morphological properties were achieved. The material was demonstrated to repeatedly achieve minimal capacity loss with short term cycling and yielded 98% of the original discharge capacity at the 300th cycle. Discharging below the 4.1 V plateau to 2.25 V did not immediately impact the cells as the reaction was reversible. However more extensive investigation into the extended reversibility in this voltage region needs to be completed for more conclusive analysis. The primary limitations for these experimental cells were the inadequacy of the electrolyte preventing access to the higher voltage plateau at 5.0 V where more capacity could be achieved, and the need for incorporating a more robust separator that has better resistance to dendrite shorts. However the cathode chemistry appears to withstand advanced cycling and further work with cell component improvements could emphasize the extent of its performance capabilities.

Chapter 9: Demonstration of High Capacity via Nickel Doping

In the previous section, iron was selected as the B-site dopant and has great potential if the electrolyte allowed the cell to be cycled at higher voltage and laboratory cells incorporated a more robust separator. The cells achieved very long cycle life, but at the lower capacities between 71 and 90 mAh/g. In order to access some of the higher voltage region, nickel is selected as a B-site dopant of the form $Li_xMn_{1-y}Ni_yO_{4-z}Cl_z$ (LMNO-Cl) due to its redox reaction centered around 4.7 V instead of 5.0 V in the case of iron.

9.1 Background

B-site doping of transition metals (Cr, Cu, Co, Fe, Ni, etc.) is the most common method today for enhancing the electrochemical properties of the lithium manganese oxide spinel due to the stabilization of the spinel lattice that is known to break down in the undoped lithium manganese oxide spinel (105-107, 110-111, 122, 128-130). Of these, Ni has proven to be the most promising due to good cycling behavior and higher capacity due to a sizeable plateau at 4.7 V (131-132). The molar ratio of 1:4 Ni to Mn has become the most studied material for single B-site doping (133). However, a disadvantage of this chemistry is that calcination above 750 °C leads to the formation of an inactive impurity phase of the rock salt structure as

reported in literature (131, 134-136). Additionally, annealing at 700 °C has shown Ni/Mn ordering starts at just 50 minutes with full ordering occurring at 60 hours (134, 136). The ordered phase tends to exhibit less cycle life and lower capacity than the disordered phase. (134, 137-139). By utilizing the developed procedure using the glycine nitrate combustion method as outlined in Chapter 2, the material is calcined at just 600 °C for 2 hours. This synthesis is therefore likely to avoid the formation of the ordered B-site metals and rocksalt structures that plague the materials requiring temperatures above 700 °C. Additionally, the cathode synthesis can be completed in full in just 4 hours. Several other methods are used to synthesize nickel-doped lithium manganate spinel including solid state, sol gel, coprecipitation, spray pyrolosis, molten salt, sacrificial templating, among others (131, 133, 140-148). However these methods are either very complex, expensive, time consuming or cumbersome for efficient production. Furthermore, by including the anion dopant chlorine, which has been demonstrated to extend the lower voltage plateau after high lithium deinsertion (deep discharge), we may be able to demonstrate high capacity in low voltage conditions.

9.2 Chemical and Structural Characterization

The attempted chemistries for this experiment were $Li_xMn_{2-y}Ni_yO_{4-z}Cl_z$ where y = 0.1, 0.2, 0.3, 0.4, and 0.5 which will be referred to as 1LMNO-Cl, 2LMNO-Cl, 3LMNO-Cl, 4LMNO-Cl, and 5LMNO-Cl respectively. However, XRF results presented in Table 9.2.1 show that the actual stoichiometry had a higher Ni-content than anticipated for each material. In order to confirm the prevention of the rocksalt-

type $Li_xNi_{1-x}O$, x-ray diffraction was performed for structural analysis. The spectra for the calcined LMNO-Cl materials are shown in Figure 9.2.1. All of the materials but 1LMNO-Cl exhibit the pure phase spinel structure. In the case of 1LMNO-Cl, more lithium precursor is necessary to eliminate the Mn_2O_3 that is present. Because of the very small size of these crystals, which are nanosized according to the SEM image presented in Figure 9.2.2, the peaks do not exhibit very high intensity so any formation of the rocksalt phase at $2\Theta = 37.5°$, 43.8°, and 63.8° should be visibly present if any of the rocksalt structure had formed. However our low temperature synthesis has eliminated the presence of the rocksalt phase. Figure 9.2.1g shows how the increased doping level of nickel shifts the (400) peak to higher angle, indicating a shift to smaller lattice parameter with additional Ni but also demonstrating solid solution of the Ni phase.

Table 9.2.1: Attempted and calculated value for y in $Li_xMn_{2-y}Ni_yO_{4-z}Cl_z$ from XRF results

Attempted Ni Content	Actual Ni Content
y = 0.10	y = 0.12
y = 0.20	y = 0.24
y = 0.30	y = 0.36
y = 0.40	y = 0.48
y = 0.50	y = 0.60

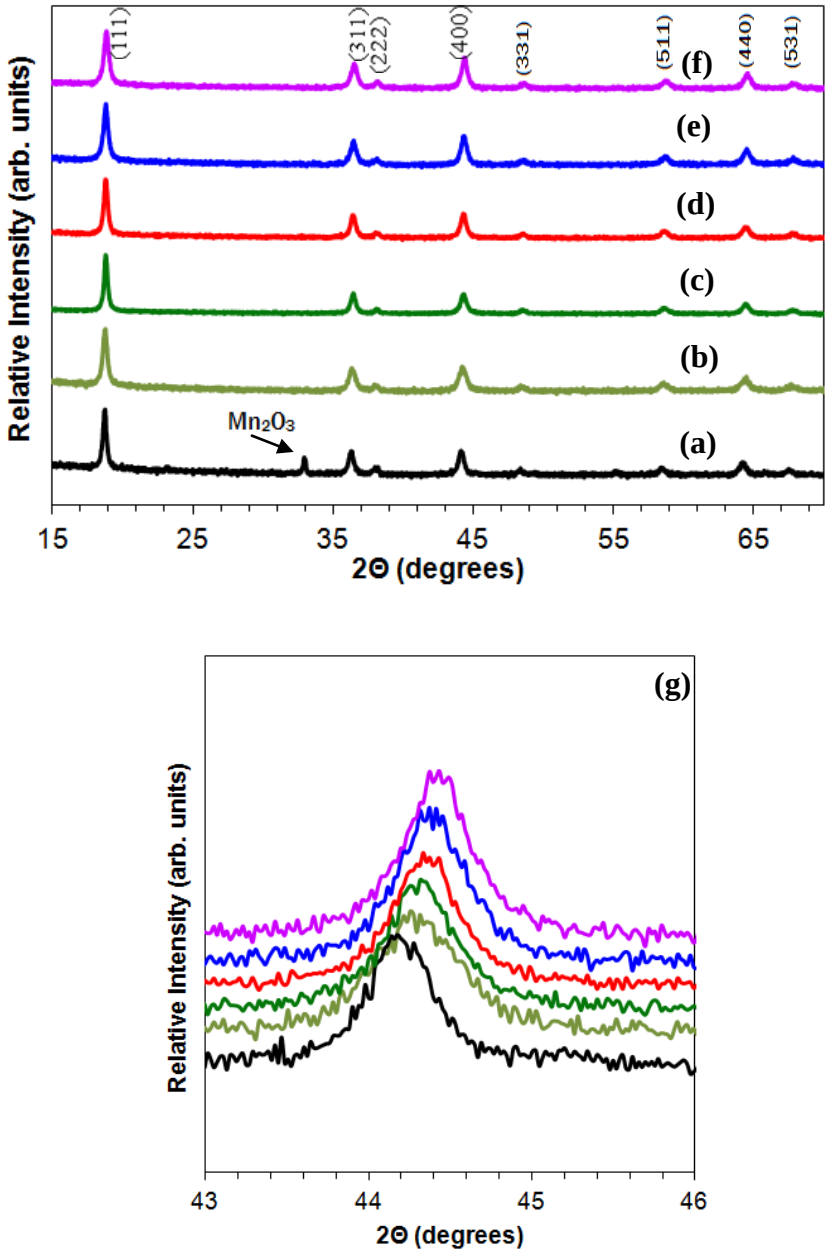

Figure 9.2.1: X-ray diffraction peaks for a) 1LMNO-Cl b) 2LMNO c) 2LMNO-Cl d) 3LMNO-Cl e) 4LMNO-Cl, and f) 5LMNO-Cl. The (400) peak is enhanced to show changes in peak position from 1LMNO-Cl to 5LMNO-Cl in g).

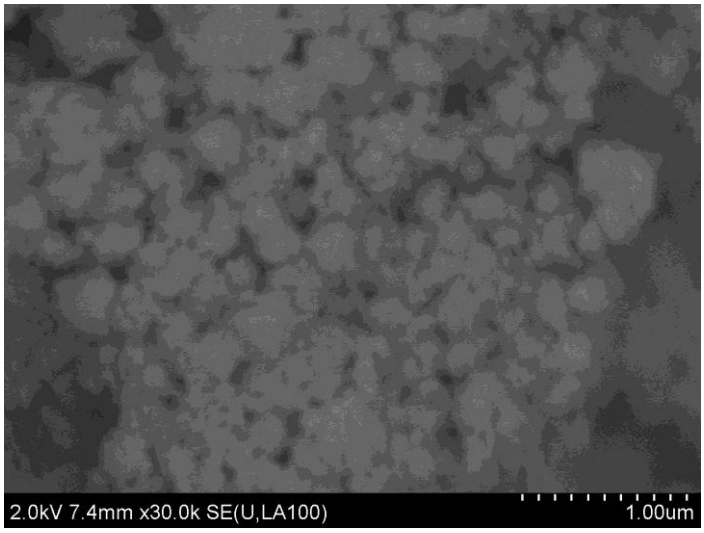

Figure 9.2.2: Representative SEM image of calcined LMNO-Cl powder

9.3 Electrochemical Performance

The calcined powders were incorporated into a button cell as described in Chapter 2. The cells were charged to 5V and discharged to 2V at 1mA/cm^2 for the forming cycle, and the second cycle under the same charge/discharge conditions for each composition (1LMNO-Cl, 2LMNO-Cl, 3LMNO-Cl, 4LMNO-Cl, and 5LMNO-Cl) is shown in Figure 9.3.1a-e. As the Ni doping level is increased, the ratio of the 4.7V to 4.1V plateaus increases, representing the shift from the Mn spinel redox couple to the Ni redox couple. Two of the compositions show noticeable differences from the set, the first is 1LMNO-Cl. The plateau centered near 3V is much shorter in the 1LMNO-Cl. Because this material had second phase Mn_2O_3, it is likely that this not electrochemically active species is impeding the insertion and deinsertion of the lithium into the lattice at these high lithium levels in the cathode. There may also be less protection from lattice distortion as more Mn exists in the Mn^{3+} which is known as the primary Jahn-Teller distortion ion (149). Both reasons can justify the lower capacity in the 1LMNO-Cl, and therefore no conclusions can be made based upon the

nickel content. The second composition with an abnormality is 3LMNO-Cl. This only reached 4.78V before discharge due to technical difficulties during a summer storm/ power surge. There may be some capacity lost in that higher voltage charge; in 4LMNO-Cl there was nearly 50 mAh/g of charge capacity above 4.78V. Unfortunately due to the nature of my appointment for this work, I cannot redo this measurement until I begin my position with the Army. But this under-charging is the primary cause of the lower capacity when compared to the rest of the data set as the 4.1V and 3V plateaus exhibit reasonable length.

The highest capacities achieved were 4LMNO-Cl and 2LMNO-Cl with 118 and 109 mAh/g at 3.5V and 205 and 196 mAh/g, respectively. Stoichiometrically, these represent $Li_xMn_{1.52}Ni_{0.48}O_{3-\delta}Cl_z$ and $Li_xMn_{1.76}Ni_{0.24}O_{3-\delta}Cl_z$, very close to 1/4 and 1/8 of the lattice sites substituted with Ni. In perfect homogeneity, this represents a Ni in every octant of the unit cell for 1/4 Ni, or every other octant of the unit cell for 1/8 Ni. However because ordering is avoided with our low temperature synthesis, we don't expect perfect homogeneity. Recall this was intentional as Kim et al. demonstrates that the disordered structure is ideal due to less strain during the one-step phase transition during cycling while the ordered structure undergoes a two-step transition during cycling (137). But because we have an appropriate average number of Ni in the unit cell, even during disorder the impact on the nearby lithium can average a holistic benefit of the Ni redox couple without the impeding effects from defect association of the Ni. The result of this over-doping can be seen in Figure 9.3.1e where we accidentally achieved $Li_xMn_{1.4}Ni_{0.6}O_{3-\delta}$. There is noticeable capacity loss and the voltage difference of the 4.7V charge and discharge plateau show how

cumbersome the charging is with so much Ni in the lattice. This difference can be seen more clearly in Figure 9.3.1f where the 5LMNO-Cl has a slightly lower 4.7V plateau on discharge and slightly higher plateau on charge than the rest of the data set.

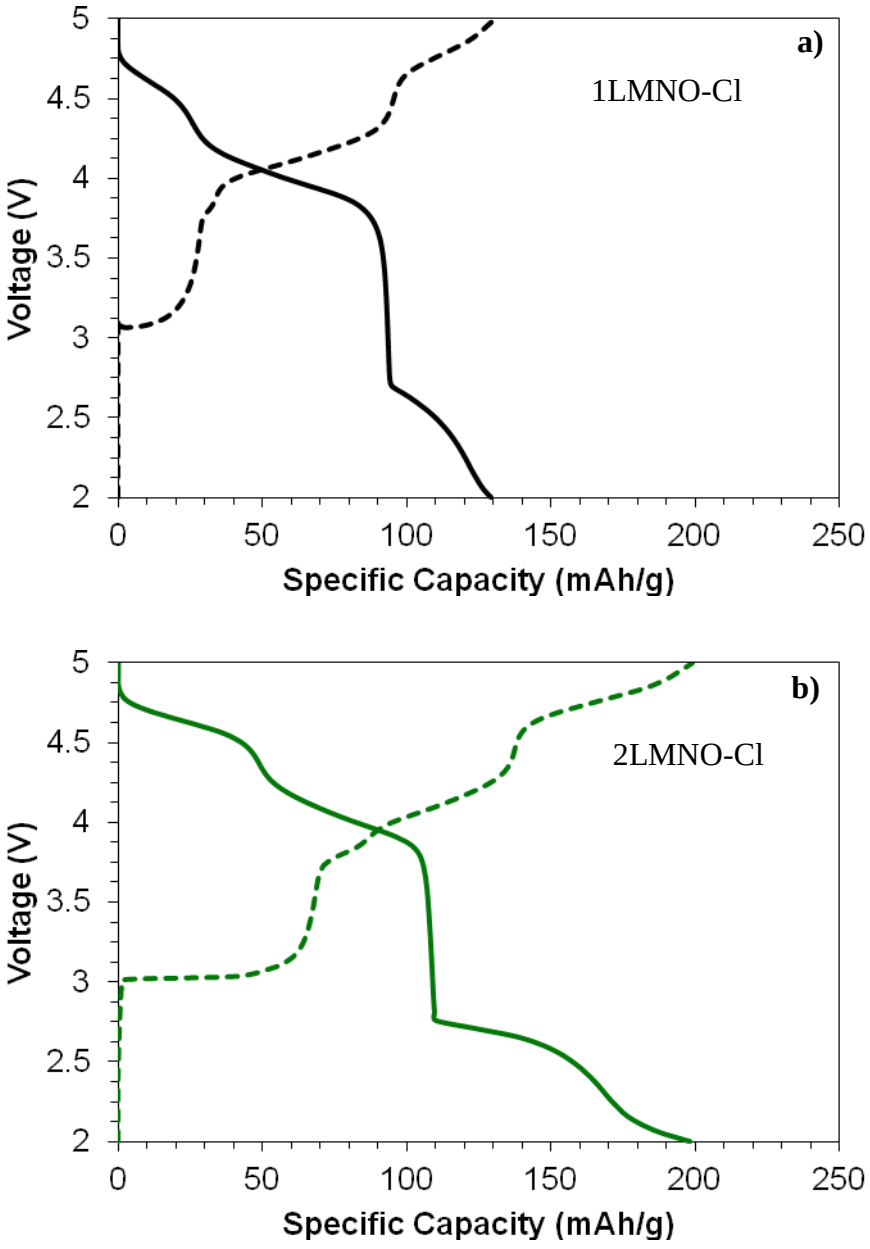

Figure 9.3.1: Charge and discharge curves from 5V to 2V at 1mA/cm^2 for a) 1LMNO-Cl, b) 2LMNO-Cl, and continued on next pages are: c) 3LMNO-Cl, d) 4LMNO-Cl, e) 5LMNO-Cl, and f) overlaid summary of all five samples.

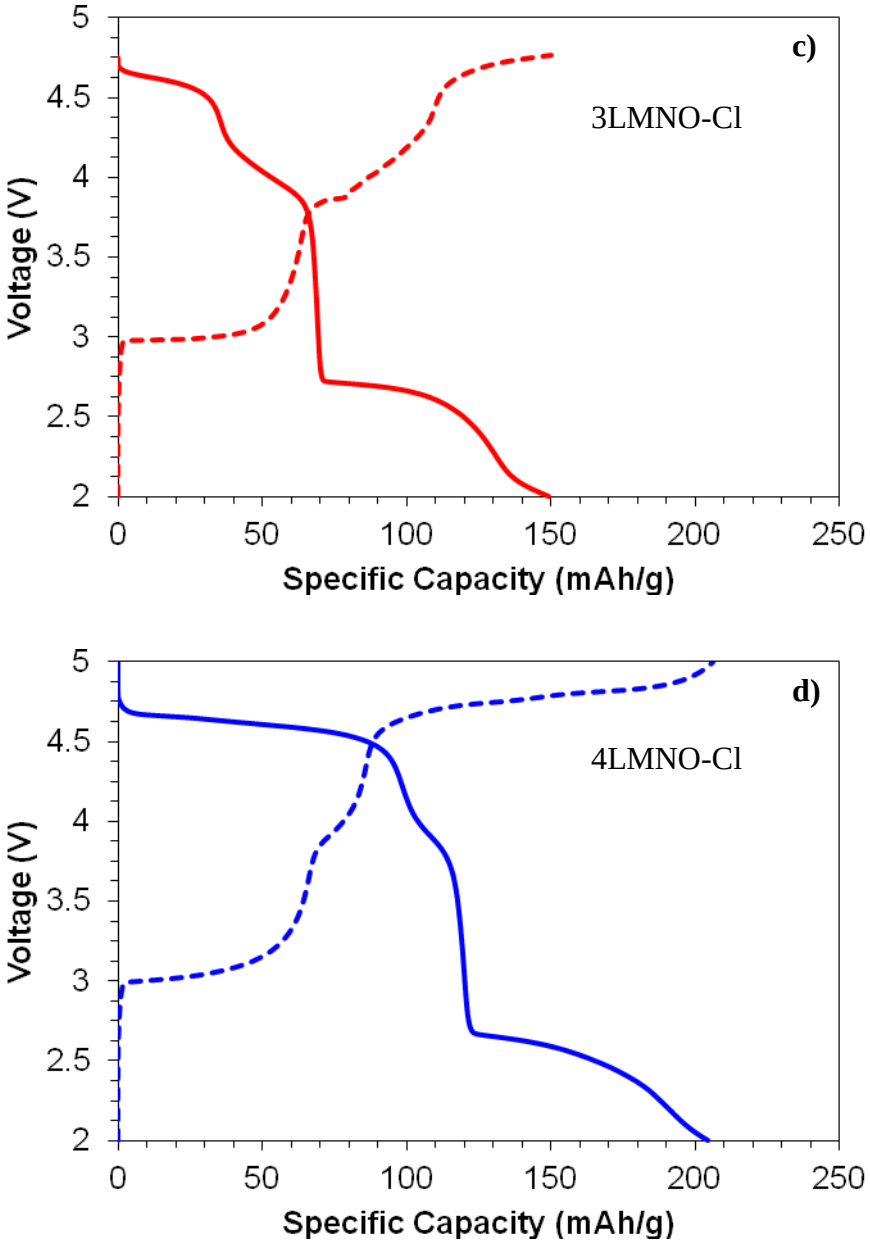

Figure 9.3.1: Charge and discharge curves from 5V to 2V at 1mA/cm^2 for a) 1LMNO-Cl and b) 2LMNO-Cl on previous page, c) 3LMNO-Cl, d) 4LMNO-Cl, and continued on next page are e) 5LMNO-Cl, and f) overlaid summary of all five samples.

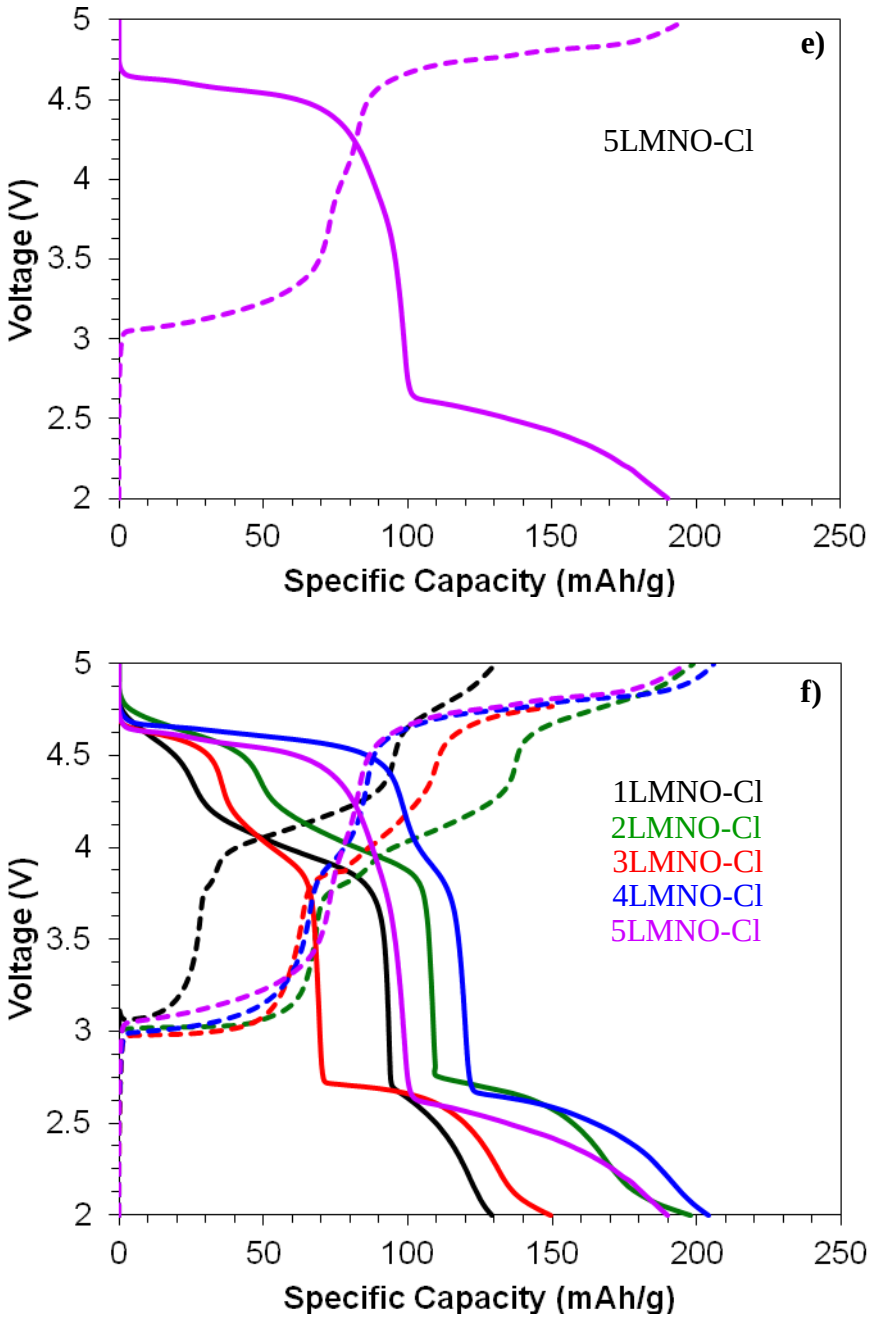

Figure 9.3.1: Charge and discharge curves from 5V to 2V at 1mA/cm^2 on previous pages are: a) 1LMNO-Cl, b) 2LMNO-Cl, c) 3LMNO-Cl, d) 4LMNO-Cl, and on this page are e) 5LMNO-Cl, and f) overlaid summary of all five samples.

In order to study the influence of the Ni-substitution and benefit of chlorine doping, $Li_xMn_2O_{4-\delta}$ (LMO) and $Li_xMn_{1.76}Ni_{0.24}O_{4-\delta}$ (2LMNO) were synthesized using the GNP method and compared with the 2LMNO-Cl sample in Figure 9.3.2. Most

noticeably, the Ni-doping clearly shows extension of the capacity above 3.5V. When comparing the LMO and 2LMNO only, the lower voltage plateau at 3V are nearly identical in length. Upon the addition of the chlorine however, comparing 2LMNO-Cl and 2LMNO, the high voltage curves are nearly indistinguishable, but the lower voltage plateau is clearly extended, just as we expected to achieve based on our previous work (9). This directly shows the added benefit of chlorine addition for applications requiring additional capacity for extreme cycling across 5V to 2V.

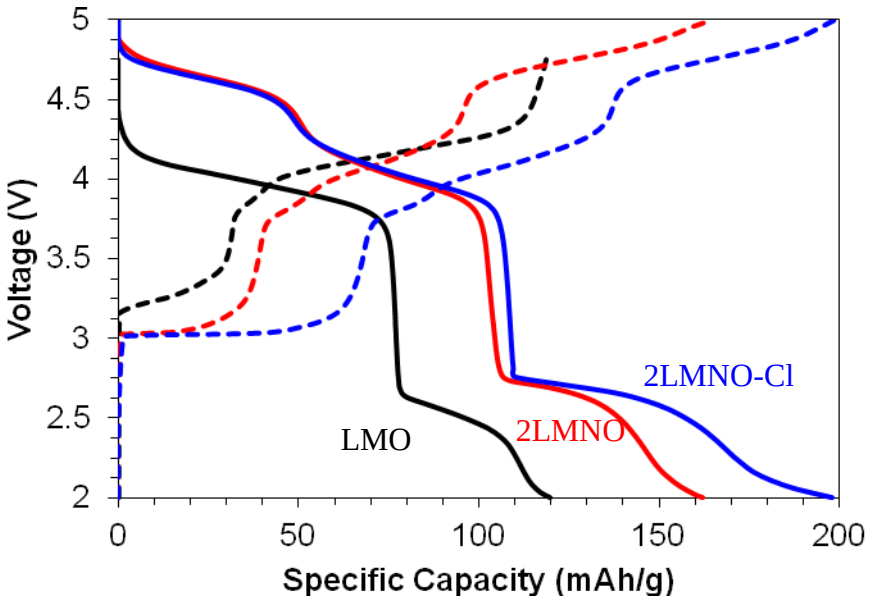

Figure 9.3.2: Comparison of cycling curves from 5V to 2V at 1mA/cm^2 of LMO, 2LMNO, and 2LMNO-Cl

9.4 Conclusions

LMNO-Cl materials were synthesized in less than 8 hours with various doping levels of Ni and confirmed to achieve no rocksalt structure at all doping levels due to the low temperature synthesis. XRF determined our attempted doping levels were lower than the actual doping level with a ratio of 1:1.2 of attempted to actual Ni doping. Charge/discharge curves of each material showed the highest capacity was

achieved in the 4LMNO-Cl and 2LMNO-Cl cases. However in the case of 1LMNO-Cl and 3LMNO-Cl, second phase Mn_2O_3 and failure to reach 5V, respectively, limited the capacity of the materials. Comparing the results from LMO, 2LMNO, and 2LMNO-Cl, we demonstrated the enhanced lower voltage plateau due to the addition of the chlorine as we expected from our previous work.

9.5. Future Work

The critical limitation of these cells is the inability to cycle at high voltage due to electrolyte degradation that is well known for $LiPF_6$ electrolytes (120-121). Eftekhari demonstrated a significant improvement in cycleability of 5V electrolytes by using $LiBF_4$, which is known to have lesser Mn dissolution (120, 150). Others have improved $LiPF_6$ with an additive that has demonstrated minimal Mn dissolution. Wang et al. added lithium bis(fluorosulfonyl)imide (LiFSI) to $LiPF_6$ in various molar ratios and determined cells with 0.3 M LiPF6 + 0.7 M LiFSI showed the smallest self-discharge and the lowest charge transfer resistance after 40 degrees C storage (151). Seng et al. first demonstrated the addition of FEC (fluoroethylene carbonate) with transition metal oxides and showed samples with FEC maintained coulombic efficiency above 95% out to 50 cycles while the samples without FEC fell below and continued to diminish after 30 cycles (152). We intend to take advantage of more modern electrolytes in order to determine the true impact of the chlorinated spinel on cyclability across the 5V to 2V range.

Currently, the additional benefits of adding the chlorine anion are not understood. One of our hypotheses for the added benefits of chlorine is that it may

assist in the octahedral to tetrahedral transition for lithium by lowering the activation energy, which is shown in the low voltage charge/discharge. Another possible benefit is that as the lithium is depleted from the crystal manganese will not achieve the full +4 valence, helping to minimize the dissolution of the manganese. This can be supported by the work by Oh et al. and Du et al. (146, 153). In their work, the fluorine addition to the lattice incorporated a more polarized Metal-F bond over the Metal-O bond. This is favorable for polar electrolytes and the liquid to solid transfer of Li^+ can be assisted. Both of these hypotheses are of interest for future study upon completion of this thesis using further analysis, for example by measuring the area specific impedance as a function of state of discharge.

Research Summary

SOFCs require high performance at lower operating temperatures for commercialization. In order to improve low temperature performance, reducing the loss due to Ohmic polarization can be achieved by designing electrolytes with improved ionic conductivity via double doping of bismuth oxides. With the highly polarizable dopants Dy, W, and Gd, a property that is linearly related to the ionic radius as it approaches that of Bi^{3+}, a lower total doping level of 12 mol% versus 20 mol% for the single doped ESB can successfully stabilize the ideal cubic fluorite structure with 25% intrinsic oxygen vacancies. Additionally, Dy in combination with Ce can also stabilize the phase even though the ionic radius of cerium is greater than of bismuth. This demonstrates the impact of adding entropy to the system.

With two dopants, there are two separate radii to create disorder and oxygen transport can be facilitated. In fact all of the double doped bismuth oxides presented here have higher conductivity than the single doped ESB, resulting in a higher mazimum power density. However, there is a limitation to this stability with the inclusion of cerium, and the structure does degrade over time. But for DWSB and DGSB, the phase and conductivity remains stable for as long as 100 hours at 650 °C in an SOFC button cell. This is a significant consideration because with less total doping, and using dopants closer in ionic radius to Bi^{3+} than erbium, one can still stabilize the structure and achieve better performance.

The performance of an SOFC was also enhanced by optimizing the design of the bilayer thickness, preventing the decomposition of electrolytes that can reduce the open circuit voltage via electrolyte reduction in low P_{O2} environments. In GDC, this

presents itself through the reduction of the valence state of Ce^{4+} to Ce^{3+}, creating mobile small polarons. In ESB, the phase can decompose into bismuth metal, clearly preventing adequate ionic conductivity with the shift of the primary charge carriers to electrons. By utilizing the bilayer concept developed by our group and identifying a critical ESB/GDC ratio while considering the degradation of OCV over time, a high performance cell was fabricated with 1.4 W/cm^2 at 650 °C in 200 SCCM H_2. This exceeds the performance of all similar bilayer cells in the literature with inexpensive and scalable synthesis methods. Not only does this result demonstrate an enhancement in the technology, but additionally the underlying science is better understood through the model developed for the bilayer and its application to the ESB and GDC system.

The improvements in these bismuth oxide materials and the bilayer design motivate a need for developing a compatible high performance cathode due to the limitations of the low melting temperature bismuth oxide that can make sintering difficult as well as its tendency for reactivity with common cathode materials containing cobalt. Engineering of an in situ co-assembled nanocomposite cathode required careful design of a synthesis method to achieve the ideal microstructure without inter-reaction. Here such a cathode is made in LSMESB; its performance is equivalent to the current very high performing state of the art cathode, BSCF (17). Though logic implies the addition of a higher conductivity material like DWSB should further improve the ASR, LSMDWSB has nearly an identical performance with the same LSM to bismuth oxide ratio due to the enhanced oxygen exchange kinetics in ESB discovered via IIE. This indicates a need for considering the

incorporation kinetics that is required for making a composite with LSM, which is known to have good oxygen dissociation kinetics but poor incorporation.

In lithium ion batteries, the incorporation of a high voltage cathode requires phase stability. A common plague to lithium manganese oxide spinels is this phase degradation due to volume changes, Mn^{3+} dissolution, or second phase formation. Our group had previously demonstrated enhanced cycle life with the addition of Cl on the O-site of AB_2O_4 likely due to the M-Cl bonding that assists with Li^+ insertion and deinsertion and possibly adding a small activation energy barrier to dissolving the manganese into the electrolyte. Incorporating high surface area cathodes can address the strain caused by volume change, so with simple synthesis a new cathode can enhance cycle life even further from 31 to 130 cycles.

B-site doping of the chlorinated spinel with Fe or Ni giving access to their redox couples and 5.0 and 4.7 V respectively, demonstrated great potential for robust chemistries. With non toxic and inexpensive Fe, one can preserve the structure longer. A cell is cycled from 4.5V to 3.5V up to 250 cycles at $1mA/cm^2$ with just 2% capacity loss. Careful cell design in the future can realize the true capability without separator or electrolyte limitations. Additionally, several different doping levels of chlorinated lithium manganese oxide with Fe or Ni can achieve successful charge and discharge across two stoichiometric lithium voltage regimes. For Ni incorporation, over 200 mAh/g can be achieved from 5V to 2V, providing emergency access to a 3V plateau for the user without damaging the cell, particularly useful for combat situations. Cycle life has yet to be realized, but by eliminating known concerns with

the Ni-doped spinel through a synthesis that eliminates cation ordering or rocksalt structure formation, the anticipation of cyclibility is optimistic.

The work presented in this dissertation is clearly divided into two parts, solid oxide fuel cells, and lithium ion batteries. Logistically, this is due to the time spent at both the University of Maryland and Army Power Division. But in this work, a number of themes are present in both sections. These topics are linked in their basic design as electrochemical devices for energy, as well as in their synthesis. Both pass charge carriers through an electrolyte between electrodes, and externally a compensating electron current can be utilized to perform work.

All of the materials discussed here are solid oxide or ceramic materials with a tailored microstructure and crystal structure that is necessary for carrying ions through or to an electrolyte, whether they are oxygen ions or lithium ions. These materials are characterized to ensure the correct phase or dopant concentration needed for its application. Because they are all in the same class of materials, ceramic processing techniques have been employed for both SOFC and Li ion battery materials, namely solid state ball milling, co-precipitation, or glycine nitrate combustion synthesis followed by a calcination to form the correct crystal structure. In cathodes for both SOFCs and Li ion batteries, a high surface area as a result of the glycine nitrate process allows for more sites for the incorporation the charge carrier (oxygen or lithium) and has demonstrated improvement of performance.

These materials all begin from the lab bench as raw materials and are developed through to laboratory devices. And furthermore, electrochemical measurements are performed on these devices to observe how the designed properties

behave in a full system. Additionally, these materials are desired to be utilized in real commercial systems. Perhaps a defining characteristic of both the Army Power Division lab as well as the Wachsman lab is the span of research from basic research to real devices as the end product. One is for actual incorporation into military specific solutions, and the other is motivated by the highest performing SOFC system that is likely to come to market this decade. So there is a need in both sections of this work to develop inexpensive and scalable synthesis methods. Thus the inclusion of cheaper materials in LSM over bismuth ruthenate, or transition metals for B-site doping of lithium manganese oxide spinels. Additionally, device fabrication must be fast and scalable. The battery cathode can be made and then incorporated into a cell immediately after calcination, preliminary EIS can be performed, and the cell can be cycling less than 8 hours from opening a bottle of raw material. Similarly, high performance bismuth oxides can be applied to substrates using a very easy ink deposition, made scalable with screen printing. And as a result of the OCV degradation realization, it was determined that the cathode can also be easily applied and the ESB electrolyte and LSMESB cathode can be co-sintered just as the NiO-GDC anode and GDC electrolyte can.

While the subject of the research changes, it is clear several themes have remained throughout the entire body of work. New solid oxide materials have been synthesized and the performance of devices with these new materials were improved. Specifically, a DGSB material has the highest conductivity known in the literature and an optimized ESB/GDC bilayer has likewise outperformed others like it with a scalable design and an inexpensive LSMESB cathode material that is equivalent to

the current state of the art but with compatibility with the excellent ionic conductors in bismuth oxides. Lithium ion battery cathodes with high voltage capability can be synthesized in less than 8 hours and still achieve enhanced cycle life and access to high capacity. These materials have been engineered to achieve maximum performance with future device commercialization in mind.

Appendices

A- Open Circuit Voltage and Electrochemical Performance of SOFCs

The open circuit voltage (OCV) of the cell is expressed by the Nernst equation:

$$E = E^0 - \frac{RT}{2F} ln \left[\frac{(P_{H2O})_{anode}}{(P_{H2})_{anode} \cdot (P_{O2})^{1/2}_{cathode}} \right] \qquad \textit{(Eq. A.1)}$$

where E^0 is standard voltage, T is the temperature, R is the gas constant (8.314 J/molK), F is Faraday's constant (9.65 * 10^{-4} C/mol), $(P_{H2O})_{anode}$, $(P_{H2})_{anode}$ are the partial pressure of water and hydrogen fuel at the anode, respectively and $(P_{O2})_{cathode}$ is the oxygen partial pressure at the cathode. The equilibrium constant K for overall reaction can be expressed as the natural long term:

$$K = \frac{(P_{H2O})_{anode}}{(P_{H2})_{anode} \cdot (P_{O2})^{1/2}_{cathode}} \qquad \textit{(Eq. A.2)}$$

The standard Gibbs free energy change for this reaction is calculated using this term:

$$\Delta G^0 = -RT lnK = -nFE^0 \qquad \textit{(Eq. A.3)}$$

where n is the number of electrons participating in the reaction. Substituting back into Eq. A.1 for the standard voltage:

$$E = \frac{RT}{2F} ln \left[K \bullet \frac{(P_{H2})_{anode} \cdot (P_{O2})^{1/2}_{cathode}}{(P_{H2O})_{anode}} \right] \qquad \textit{(Eq. A.4)}$$

From Eq. 1.4, the equilibrium constant for water dissociation can be determined as

follows:

$$K_{H2O} = \frac{(P_{H2})_{anode} \cdot (P_{O2})^{1/2}_{cathode}}{(P_{H2O})_{anode}} = \frac{1}{K} \qquad \textit{(Eq. A.5)}$$

By rearranging to solve for $(P_{O2})^{1/2}_{cathode}$ gives:

$$(P_{O2})^{1/2}_{cathode} = \frac{(P_{H2O})_{anode}}{(P_{H2})_{anode} \cdot K} \qquad \textit{(Eq. A.6)}$$

Inserting back into Eq. 1.5 gives the following equation:

$$E = \frac{RT}{2F} \ln \left(\frac{(P_{O2})^{1/2}_{cathode}}{(P_{O2})^{1/2}_{anode}} \right) \qquad \textit{(Eq. A.7)}$$

Therefore, the P_{O2} difference between the two electrodes has a strong impact on OCV. This has implications for the work in Chapter 4 where we must consider the interfacial oxygen partial pressure in the electrolyte system where decomposition of one electrolyte can impact the open circuit voltage.

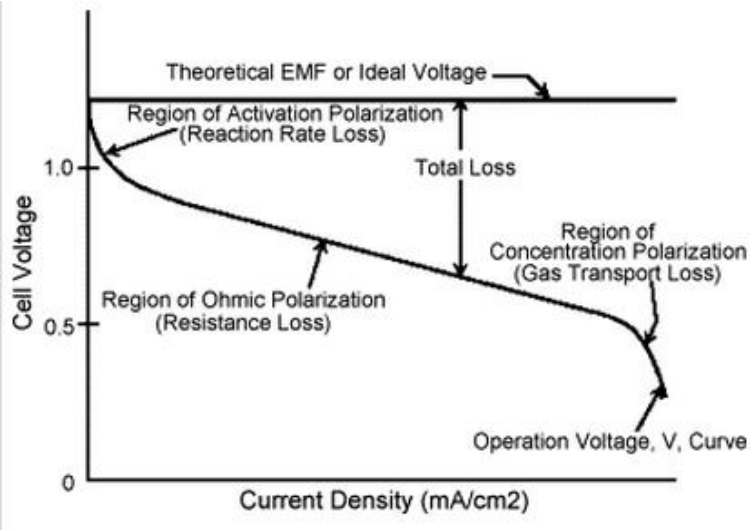

Figure A.1: Theoretical and actual cell voltage for an SOFC (31)

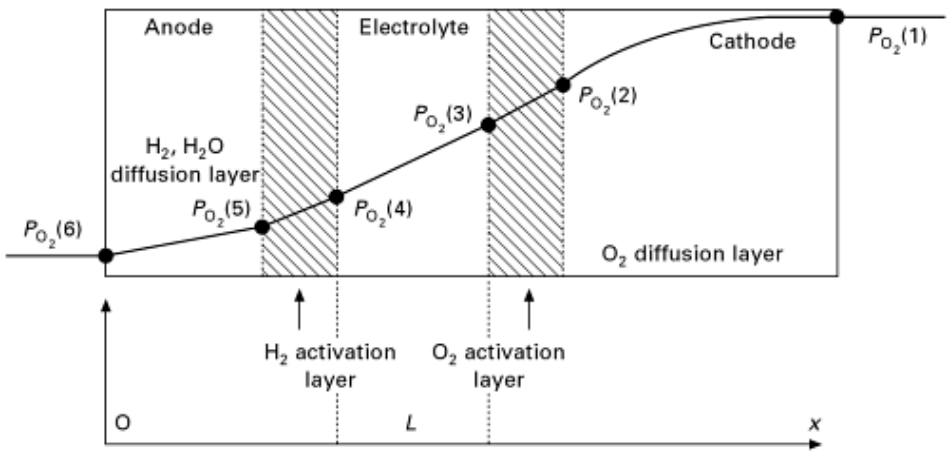

Figure A.2: Schematic of P_{O2} profile across the functional layers of an SOFC (32)

The actual electrochemical cell potential is less than its ideal potential due to irreversible losses. These losses are known as overpotentials or polarization. Figure A.1 shows a schematic diagram which explains multiple phenomena associated with irreversible losses in an actual fuel cell. Figure A.2 shows the schematic of a fuel cell with the considerations of P_{O2} and electrolyte thickness, L. The first of these is activation polarization ($\eta_{activation}$) and this originates from the activation energy of the electrochemical reactions shown earlier at the electrodes. A high activation energy for oxygen dissociation at the cathode, for example, would increase this polarization. This is shown in Figure A.2 as the activation layers. The second type is ohmic polarization (η_{ohmic}) . These losses are caused by contact resistance, ionic and electronic resistances in the cell components and as the name suggests, follows Ohm's law. The third is concentration polarization ($\eta_{concentration}$). This type of polarization is due to mass transport limitations and strongly depends on the current density, reactant activity and electrode structure. For example, high tortuosity in the anode could result in the inability of H_2 to get to the triple phase boundary in order to combine

with the O^{2-}. These losses occur in the diffusion layer regions of Figure A.2. Considering these losses, and actual voltage can be expressed as:

$$V = V_0 - \eta_{activation} - \eta_{ohmic} - \eta_{concentration} \qquad \textit{(Eq. A.8)}$$

where V is the actual voltage, and V_o is the theoretical voltage.

Among these three polarization mechanisms, ohmic polarization occurs because of resistance to the flow of ions and electrons in the electrolyte and electrodes, respectively. As mentioned previously, this polarization obeys Ohm's Law:

$$\eta_{ohmic} = IR \qquad \textit{(Eq. A.9)}$$

where I is the current flowing through the cell, and R is the total cell resistance. This total resistance includes an electronic contribution, ionic contribution, and any contact resistance. The ohmic resistance normalized by the active cell area (in cm^2) is referred to as the area specific resistance (ASR). The ASR is a function of the cell design, material choice and density. The ohmic polarization can be explained by:

$$\eta_{ohmic} = IR = i \bullet (ASR) = i \bullet \rho \bullet L = i \bullet (1/\sigma) \bullet L \qquad \textit{(Eq. A.10)}$$

where i is the current density, L is the current path length (thickness), ρ is the resistivity, and σ is the conductivity.

It is evident that ohmic polarization in the electrolyte is determined by its conductivity and thickness. As such we must minimize the thickness of the electrolyte by using anode-supported cells and select a high conductivity material like bismuth oxide for use in SOFCs.

B- Electrochemical Impedance Spectroscopy

Also known as AC Impedance Spectroscopy due to the application of alternating current, electrochemical impedance spectroscopy (EIS) is used in this work for determining conductivity of the bismuth oxide ionic conductors and for determining the area specific resistance (ASR) for cathode materials. Upon application of an excitation voltage, in our case 50 mV in amplitude, at several frequencies, the result at each frequency can be plotted in a Nyquist plot with real and imaginary components to the impedance. Consider that the impedance is much like resistance in that it is the measure of the opposition to current flow but in an alternating current rather than direct current. As such it depends upon the frequency, ω. By adding this time consideration to the well known relationship of Ohm's law:

$$Z(\omega) = \frac{V(t)}{I(t)} \qquad \textit{(Eq. B.1)}$$

where V is the AC voltage and I is the current. This value for Z can also be separated into real (Z') and imaginary (Z") components:

$$Z = Z' + iZ'' \qquad \textit{(Eq. B.2)}$$

When plotting Z' vs. Z", a semicircle is formed and its intersection with the x-axis (where the imaginary term is equal to zero) corresponds to a resistance, R. The most basic example is shown in Figure B.1 of an RC circuit, and this value of R corresponds to the resistance of the resistor in the circuit. But often there are additional resistances without a capacitive component, shown in Figure B.2 as R_u.

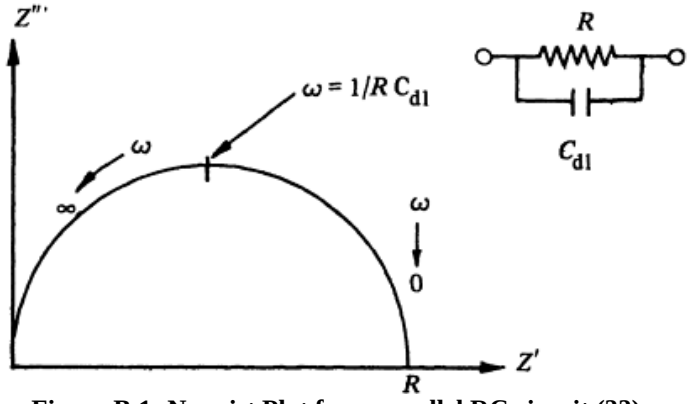

Figure B.1: Nyquist Plot for a parallel RC circuit (33)

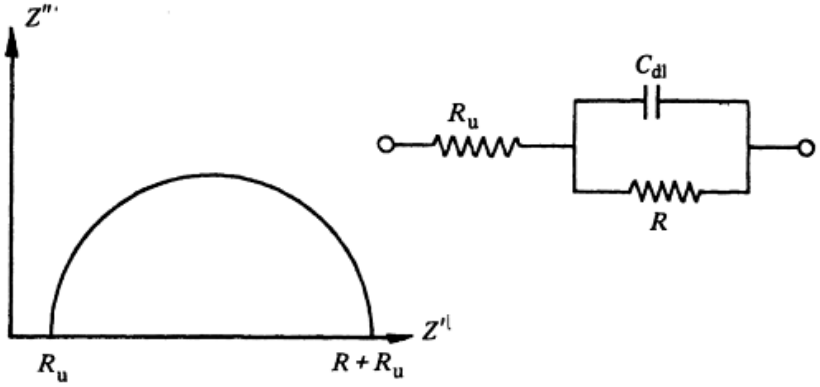

Figure B.2: Nyquist plot of RC parallel circuit with the addition of an uncompensated solution (electrolyte) resistance, R_u (33)

In SOFC materials, there can be several relaxation processes that are described by more than one arc. Typically we can attribute these arcs in order of highest to lowest frequency to the bulk, grain boundary, and electrode processes in typical polycrystalline ceramic conductors (154). However these arcs don't always center on the x-axis to create the perfect semicircle but rather are secanted by the x-axis and appear to be depressed below the x-axis. This requires a model that replaces the capacitor with a constant phase element that represents a distribution of capacitors in parallel whose phase angle is less than 90 degrees.

In bismuth oxides, the grain boundary resistance is absent, resulting in only bulk and electrode processes to be determined through EIS (155). In this work, we

are interested in both of these for the bismuth oxide ionic conductivity and cathode ASR determination. An example result from a 20 mol% Er doped bismuth oxide (ESB) made using SS and CP methods with platinum current collectors at 550 °C is shown in Figure B.3. The grain boundary resistance is negligible, so we consider the high frequency intercept with the x-axis to be equivalent to the bulk resistance of the ESB. Due to the high conductivity of our material we have to subtract the resistance of the experimental set up. In our case this ranged from 1.2 to 1.8 Ω and was measured each time leads were connected to the set up. Knowing the resistance of the bulk material, from the sample geometry we can calculate the conductivity:

$$\sigma = \frac{d}{A \cdot R} \qquad \textit{(Eq. B.3)}$$

where d is the sample thickness and A is the cross-sectional area that is perpendicular to the direction of current flow. When this measurement is performed at various temperatures, the activation energy, E_a can be determined from the slope of an Arrhenius plot according to:

$$\sigma T = A exp\left(-\frac{E_a}{kT}\right)$$

where k is Boltzmann's constant, and A is a pre-exponential factor that is a product of several factors, including entropy, ion jump attempts, crystal structure and parameter.

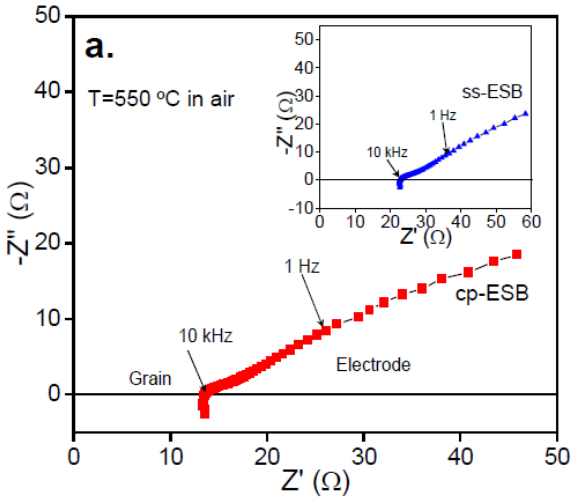

Figure B.3: Typical impedance spectra of cp-ESB in air at 550 °C (inset : ss-ESB)(34)

In Figure B.4, an example of a symmetric cell LSMDWSB cathode on ESB at 700 °C in air is shown. The low frequency x-axis intercept (~2.73 Ω in this example) is considered the total resistance. This resistance less the bulk resistance (high frequency intercept, 2.545 Ω) can be attributed to the resistance of the electrode. In symmetric cells, the electrodes are both the cathode material, so this resistance is divided by two and multiplied by the cross-sectional area to determine the area specific resistance (ASR) of the cathode at the given temperature.

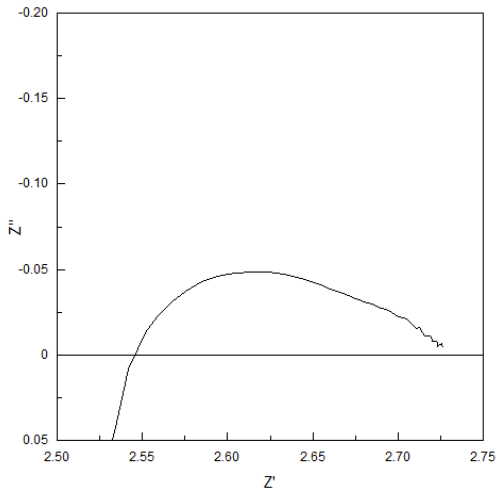

Figure B.4: Impedance plot for LSMDWSB on ESB in air at 700 °C

Bibliography

1. E. D. Wachsman and K. T. Lee, *Science*, **334**, 935 (2011).
2. J.-Y. Park and E. D. Wachsman, *Ionics*, **12**, 15 (2006).
3. J. S. Ahn, M. A. Camaratta, D. Pergolesi, K. T. Lee, H. Yoon, B. W. Lee, D. W. Jung, E. Traversa and E. D. Wachsman, *Journal of The Electrochemical Society*, **157**, B376 (2010).
4. U. S. D. o. Energy, Types of Fuel Cells, in.
5. P. Shuk, H. D. Wiemhöfer, U. Guth, W. Göpel and M. Greenblatt, *Solid State Ionics*, **89**, 179 (1996).
6. M. J. Verkerk and A. J. Burggraaf, *Solid State Ionics*, **3–4**, 463 (1981).
7. M. Verkerk and A. Burggraaf, *Journal of The Electrochemical Society*, **128**, 75 (1981).
8. H. Xia, Y. Meng, L. Lu and G. Ceder, *Journal of The Electrochemical Society*, **154**, A737 (2007).
9. T. Atwater and P. Tavares, *SAE International Journal of Materials and Manufacturing*, **6**, 85 (2013).
10. D. Oh, FUNDAMENTAL UNDERSTANDING OF SURFACE CHARACTERSITIC AND
CHROMIUM CONTAMINATION ON SOLID OXIDE FUEL CELL CATHODES, in, University of Florida (2010).
11. E. P. Murray and S. Barnett, *Solid State Ionics*, **143**, 265 (2001).
12. F. Deganello, V. Esposito, M. Miyayama and E. Traversa, *Journal of The Electrochemical Society*, **154**, A89 (2007).
13. F. Han, R. Mücke, T. Van Gestel, A. Leonide, N. H. Menzler, H. P. Buchkremer and D. Stöver, *Journal of Power Sources*, **218**, 157 (2012).
14. E. P. Murray, M. Sever and S. Barnett, *Solid State Ionics*, **148**, 27 (2002).
15. C. Xia, Y. Zhang and M. Liu, *Applied physics letters*, **82**, 901 (2003).
16. X. Lou, S. Wang, Z. Liu, L. Yang and M. Liu, *Solid State Ionics*, **180**, 1285 (2009).
17. Z. Shao and S. M. Haile, *Nature*, **431**, 170 (2004).
18. Q. Zhang, A. Hirano, N. Imanishi, Y. Takeda and K. Yamahara, *Journal of fuel cell science and technology*, **6**, 011001 (2009).
19. J. Li, S. Wang, X. Sun, R. Liu, X. Ye and Z. Wen, *Journal of Power Sources*, **185**, 649 (2008).
20. J. Li, S. Wang, Z. Wang, R. Liu, T. Wen and Z. Wen, *Journal of Power Sources*, **194**, 625 (2009).
21. Z. Jiang, L. Zhang, K. Feng and C. Xia, *Journal of Power Sources*, **185**, 40 (2008).

22. Z. Jiang, Z. Lei, B. Ding, C. Xia, F. Zhao and F. Chen, *International Journal of Hydrogen Energy*, **35**, 8322 (2010).
23. K. T. Lee, D. W. Jung, H. S. Yoon, A. A. Lidie, M. A. Camaratta and E. D. Wachsman, *Journal of Power Sources*, **220**, 324 (2012).
24. H. Rietveld, *Journal of applied Crystallography*, **2**, 65 (1969).
25. A. Le Bail, H. Duroy and J. Fourquet, *Materials Research Bulletin*, **23**, 447 (1988).
26. D. W. Jung, Conductivity and stability of bismuth oxide-based electrolytes and their applications for IT-SOFCs, in, University of Florida (2009).
27. T. Suzuki, M. Awano, P. Jasinski, V. Petrovsky and H. U. Anderson, *Solid State Ionics*, **177**, 2071 (2006).
28. S. P. Jiang, *Materials Science and Engineering: A*, **418**, 199 (2006).
29. E. P. Murray, T. Tsai and S. A. Barnett, *Solid State Ionics*, **110**, 235 (1998).
30. K. T. Lee, A. A. Lidie, H. S. Yoon and E. D. Wachsman, *Angewandte Chemie International Edition*, **53**, 13463 (2014).
31. I. EG&G Technical Services, *Fuel Cell Handbook* (2004).
32. K. Huang and J. B. Goodenough, *Solid oxide fuel cell technology: principles, performance and operations*, Elsevier (2009).
33. D. Pletcher, R. Greff, R. Peat, L. Peter and J. Robinson, *Instrumental methods in electrochemistry*, Elsevier (2001).
34. K. T. Lee, A. A. Lidie, S. Y. Jeon, G. T. Hitz, S. J. Song and E. D. Wachsman, *Journal of Materials Chemistry A*, **1**, 6199 (2013).
35. A. B. Stambouli and E. Traversa, *Renewable and Sustainable Energy Reviews*, **6**, 433 (2002).
36. Y. Arachi, H. Sakai, O. Yamamoto, Y. Takeda and N. Imanishai, *Solid State Ionics*, **121**, 133 (1999).
37. V. Kharton, F. Marques and A. Atkinson, *Solid State Ionics*, **174**, 135 (2004).
38. S. Boyapati, E. D. Wachsman and N. Jiang, *Solid State Ionics*, **140**, 149 (2001).
39. N. Jiang, E. D. Wachsman and S.-H. Jung, *Solid State Ionics*, **150**, 347 (2002).
40. E. D. Wachsman, *Journal of the European Ceramic Society*, **24**, 1281 (2004).
41. H. Harwig, *Zeitschrift für anorganische und allgemeine Chemie*, **444**, 151 (1978).
42. N. Jiang and E. D. Wachsman, *Journal of the American Ceramic Society*, **82**, 3057 (1999).
43. E. D. Wachsman, S. Boyapati and N. Jiang, *Ionics*, **7**, 1 (2001).
44. D. W. Jung, K. L. Duncan and E. D. Wachsman, *Acta Materialia*, **58**, 355 (2010).
45. E. Wachsman, G. Ball, N. Jiang and D. Stevenson, *Solid State Ionics*, **52**, 213 (1992).
46. T. Takahashi, T. Esaka and H. Iwahara, *Journal of Applied Electrochemistry*, **7**, 299 (1977).
47. J. S. Ahn, D. Pergolesi, M. A. Camaratta, H. Yoon, B. W. Lee, K. T. Lee, D. W. Jung, E. Traversa and E. D. Wachsman, *Electrochemistry Communications*, **11**, 1504 (2009).

48. B. Ebin, S. Gürmen, C. Arslan and G. Lindbergh, *Electrochimica Acta*, **76**, 368 (2012).
49. D. Liu, W. Zhu, J. Trottier, C. Gagnon, F. Barray, A. Guerfi, A. Mauger, H. Groult, C. M. Julien, J. B. Goodenough and K. Zaghib, *RSC Advances*, **4**, 154 (2014).
50. H. Xia, Y. S. Meng, M. O. Lai and L. Lu, *Journal of The Electrochemical Society*, **157**, A348 (2010).
51. A. Manthiram, *The Journal of Physical Chemistry Letters*, **2**, 176 (2011).
52. H. Xia, Z. Luo and J. Xie, *Progress in Natural Science: Materials International*, **22**, 572 (2012).
53. H. Huang, C. A. Vincent and P. G. Bruce, *Journal of The Electrochemical Society*, **146**, 3649 (1999).
54. Y. Xia and M. Yoshio, *Journal of The Electrochemical Society*, **143**, 825 (1996).
55. T. B. Atwater, P. C. Tavares and L. M. Marzocca, *Proceedings 44th Power Sources Conference*, **44** (2010).
56. Q. Zhen, G. M. Kale, G. Shi, R. Li, W. He and J. Liu, *Solid State Ionics*, **176**, 2727 (2005).
57. L. Leontie, M. Caraman, A. Visinoiu and G. I. Rusu, *Thin Solid Films*, **473**, 230 (2005).
58. T. Takahashi and H. Iwahara, *Journal of Applied Electrochemistry*, **3**, 65 (1973).
59. G. Meng, C. Chen, X. Han, P. Yang and D. Peng, *Solid State Ionics*, **28**, 533 (1988).
60. M. Drache, P. Conflant and J. Boivin, *Solid State Ionics*, **57**, 245 (1992).
61. K. Huang, M. Feng and J. B. Goodenough, *Solid State Ionics*, **89**, 17 (1996).
62. R. Shannon and C. Prewitt, *Acta Crystallographica Section B: Structural Crystallography and Crystal Chemistry*, **26**, 1046 (1970).
63. S. Boyapati, E. D. Wachsman and B. C. Chakoumakos, *Solid State Ionics*, **138**, 293 (2001).
64. E. D. Wachsman, S. Boyapati, M. J. Kaufman and N. Jiang, *Journal of the American Ceramic Society*, **83**, 1964 (2000).
65. J. Y. Park, H. Yoon and E. D. Wachsman, *Journal of the American Ceramic Society*, **88**, 2402 (2005).
66. E. Wachsman, *Solid State Ionics*, **152**, 657 (2002).
67. E. Wachsman, P. Jayaweera, N. Jiang, D. Lowe and B. Pound, *Journal of The Electrochemical Society*, **144**, 233 (1997).
68. K. Eguchi, T. Setoguchi, T. Inoue and H. Arai, *Solid State Ionics*, **52**, 165 (1992).
69. M. Verkerk, K. Keizer and A. Burggraaf, *Journal of Applied Electrochemistry*, **10**, 81 (1980).
70. S. Shen, L. Guo and H. Liu, *International Journal of Hydrogen Energy*, **38**, 13084 (2013).
71. S. Shen, L. Guo and H. Liu, *International Journal of Hydrogen Energy*, **38**, 1967 (2013).
72. T.-H. Kwon, T. Lee and H.-I. Yoo, *Solid State Ionics*, **195**, 25 (2011).

73. S. H. Chan, X. J. Chen and K. A. Khor, *Solid State Ionics*, **158**, 29 (2003).
74. S. Shen and M. Ni, *Journal of The Electrochemical Society*, **162**, F340 (2015).
75. K. Pearson, *The London, Edinburgh, and Dublin Philosophical Magazine and Journal of Science*, **2**, 559 (1901).
76. B. Steele, *Solid State Ionics*, **129**, 95 (2000).
77. E. P. Murray, T. Tsai and S. Barnett, *Nature*, **400**, 649 (1999).
78. K. T. Lee, C. M. Gore and E. D. Wachsman, *Journal of Materials Chemistry*, **22**, 22405 (2012).
79. S. Park, J. M. Vohs and R. J. Gorte, *Nature*, **404**, 265 (2000).
80. Y.-H. Huang, R. I. Dass, Z.-L. Xing and J. B. Goodenough, *Science*, **312**, 254 (2006).
81. L. Yang, S. Wang, K. Blinn, M. Liu, Z. Liu, Z. Cheng and M. Liu, *Science*, **326**, 126 (2009).
82. E. D. Wachsman, C. A. Marlowe and K. T. Lee, *Energy & Environmental Science*, **5**, 5498 (2012).
83. S. B. Adler, *Chemical reviews*, **104**, 4791 (2004).
84. W. Zhou, Z. Shao, R. Ran and R. Cai, *Electrochemistry Communications*, **10**, 1647 (2008).
85. A. Petric, P. Huang and F. Tietz, *Solid State Ionics*, **135**, 719 (2000).
86. A. Mai, M. Becker, W. Assenmacher, F. Tietz, D. Hathiramani, E. Ivers-Tiffée, D. Stöver and W. Mader, *Solid State Ionics*, **177**, 1965 (2006).
87. E. Bucher, A. Egger, G. Caraman and W. Sitte, *Journal of The Electrochemical Society*, **155**, B1218 (2008).
88. D. Oh, D. Gostovic and E. D. Wachsman, *Journal of Materials Research*, **27**, 1992 (2012).
89. S. P. Yoon, J. Han, S. W. Nam, T.-H. Lim, I.-H. Oh, S.-A. Hong, Y.-S. Yoo and H. C. Lim, *Journal of Power Sources*, **106**, 160 (2002).
90. E. Armstrong, K. Duncan, D. Oh, J. Weaver and E. Wachsman, *Journal of The Electrochemical Society*, **158**, B492 (2011).
91. E. N. Armstrong, K. L. Duncan and E. D. Wachsman, *Physical Chemistry Chemical Physics*, **15**, 2298 (2013).
92. D. W. Jung, K. L. Duncan and E. D. Wachsman, *Acta Materialia*, **58**, 355 (2010).
93. K. T. Lee, H. S. Yoon and E. D. Wachsman, *Journal of Materials Research*, **27**, 2063 (2012).
94. B. Steele, J. Kilner, P. Dennis, A. McHale, M. Van Hemert and A. Burggraaf, *Solid State Ionics*, **18**, 1038 (1986).
95. R. D. Bayliss, S. N. Cook, S. Kotsantonis, R. J. Chater and J. A. Kilner, *Advanced Energy Materials*, **4** (2014).
96. C. Kan, H. Kan, F. Van Assche, E. Armstrong and E. Wachsman, *Journal of The Electrochemical Society*, **155**, B985 (2008).
97. C. Kan and E. Wachsman, *Journal of The Electrochemical Society*, **156**, B695 (2009).
98. C. Kan and E. Wachsman, *Solid State Ionics*, **181**, 338 (2010).
99. S. Jain, K. Adiga and V. P. Verneker, *Combustion and flame*, **40**, 71 (1981).

100. D. Yoon, J.-J. Lee, H.-G. Park and S.-H. Hyun, *Journal of The Electrochemical Society*, **157**, B455 (2010).
101. E.-O. Oh, C.-M. Whang, Y.-R. Lee, S.-Y. Park, D. H. Prasad, K. J. Yoon, J.-W. Son, J.-H. Lee and H.-W. Lee, *Advanced Materials*, **24**, 3373 (2012).
102. K. T. Lee, H. S. Yoon, J. S. Ahn and E. D. Wachsman, *Journal of Materials Chemistry*, **22**, 17113 (2012).
103. E. Perry Murray and S. Barnett, *Solid State Ionics*, **143**, 265 (2001).
104. N. M. Hagh and G. G. Amatucci, *Journal of Power Sources*, **256**, 457 (2014).
105. S. Jayapal, R. Mariappan, S. Sundar and S. Piraman, *Journal of Electroanalytical Chemistry*, **720**, 58 (2014).
106. X. He, J. Li, Y. Cai, Y. Wang, J. Ying, C. Jiang and C. Wan, *Journal of Power Sources*, **150**, 216 (2005).
107. J. Morales, L. Sánchez and J. Tirado, *Journal of Solid State Electrochemistry*, **2**, 420 (1998).
108. J. Amarilla, J. Martin de Vidales and R. Rojas, *Solid State Ionics*, **127**, 73 (2000).
109. H. J. Bang, V. Donepudi and J. Prakash, *Electrochimica Acta*, **48**, 443 (2002).
110. G. Amatucci, A. Du Pasquier, A. Blyr, T. Zheng and J.-M. Tarascon, *Electrochimica Acta*, **45**, 255 (1999).
111. G. Amatucci, N. Pereira, T. Zheng, I. Plitz and J. Tarascon, *Journal of Power Sources*, **81**, 39 (1999).
112. W.-R. Liu, S.-H. Wu and H.-S. Sheu, *Journal of Power Sources*, **146**, 232 (2005).
113. J. Son and H. Kim, *Journal of Power Sources*, **147**, 220 (2005).
114. M. T. Makhlouf, B. Abu-Zied and T. Mansoure, *Physical Chemistry*, **2**, 86 (2012).
115. C. Wu, F. Wu, L. Chen and X. Huang, *Solid State Ionics*, **152**, 335 (2002).
116. T. B. Atwater and P. C. Tavares, Solid state preparation method for lithium manganese oxide AB 2 O 4 battery cathode, in, US Patent 8,900,756 (2014).
117. L. Cong, T. He, Y. Ji, P. Guan, Y. Huang and W. Su, *J Alloy Compd*, **348**, 325 (2003).
118. L. Yang, B. Ravdel and B. L. Lucht, *Electrochemical and Solid-State Letters*, **13**, A95 (2010).
119. W. Liu, G. Farrington, F. Chaput and B. Dunn, *Journal of The Electrochemical Society*, **143**, 879 (1996).
120. A. Eftekhari, *Journal of Power Sources*, **124**, 182 (2003).
121. M. Pico, I. Álvarez-Serrano, M. López and M. Veiga, *Dalton Transactions*, **43**, 14787 (2014).
122. H. Kawai, M. Nagata, M. Tabuchi, H. Tukamoto and A. R. West, *Chemistry of materials*, **10**, 3266 (1998).
123. I. Taniguchi and Z. Bakenov, *Powder technology*, **159**, 55 (2005).
124. N. Kang, J. H. Park, J. Choi, J. Jin, J. Chun, I. G. Jung, J. Jeong, J. G. Park, S. M. Lee and H. J. Kim, *Angewandte Chemie*, **124**, 6730 (2012).
125. L. Hu, Z. Zhang and K. Amine, *Journal of Power Sources*, **236**, 175 (2013).
126. Z. Yang, Y. Jiang, J.-H. Kim, Y. Wu, G.-L. Li and Y.-H. Huang, *Electrochimica Acta*, **117**, 76 (2014).

127. J. H. Lee and K. J. Kim, *Electrochimica Acta*, **102**, 196 (2013).
128. C. Sigala, D. Guyomard, A. Verbaere, Y. Piffard and M. Tournoux, *Solid State Ionics*, **81**, 167 (1995).
129. H. Kawai, M. Nagata, H. Kageyama, H. Tukamoto and A. R. West, *Electrochimica Acta*, **45**, 315 (1999).
130. H. Shigemura, H. Sakaebe, H. Kageyama, H. Kobayashi, A. West, R. Kanno, S. Morimoto, S. Nasu and M. Tabuchi, *Journal of The Electrochemical Society*, **148**, A730 (2001).
131. Q. Zhong, A. Bonakdarpour, M. Zhang, Y. Gao and J. Dahn, *Journal of The Electrochemical Society*, **144**, 205 (1997).
132. T. Ohzuku, S. Takeda and M. Iwanaga, *Journal of Power Sources*, **81–82**, 90 (1999).
133. R. Santhanam and B. Rambabu, *Journal of Power Sources*, **195**, 5442 (2010).
134. K. M. Shaju and P. G. Bruce, *Dalton Transactions*, 5471 (2008).
135. D. Pasero, N. Reeves, V. Pralong and A. West, *Journal of The Electrochemical Society*, **155**, A282 (2008).
136. L. Cai, Z. Liu, K. An and C. Liang, *Journal of Materials Chemistry A*, **1**, 6908 (2013).
137. J.-H. Kim, S.-T. Myung, C. Yoon, S. Kang and Y.-K. Sun, *Chemistry of materials*, **16**, 906 (2004).
138. A. Bhaskar, N. N. Bramnik, A. Senyshyn, H. Fuess and H. Ehrenberg, *Journal of The Electrochemical Society*, **157**, A689 (2010).
139. K. Takahashi, M. Saitoh, M. Sano, M. Fujita and K. Kifune, *Journal of The Electrochemical Society*, **151**, A173 (2004).
140. S.-H. Park, S.-W. Oh, S.-T. Myung, Y. Kang and Y.-K. Sun, *Solid State Ionics*, **176**, 481 (2005).
141. M. Lazarraga, L. Pascual, H. Gadjov, D. Kovacheva, K. Petrov, J. Amarilla, R. Rojas, M. Martin-Luengo and J. Rojo, *Journal of Materials Chemistry*, **14**, 1640 (2004).
142. J.-H. Kim, S.-T. Myung and Y.-K. Sun, *Electrochimica Acta*, **49**, 219 (2004).
143. Q. Sun, X.-h. Li, Z.-x. Wang and Y. Ji, *Transactions of Nonferrous Metals Society of China*, **19**, 176 (2009).
144. H.-s. Fang, Z.-x. Wang, X.-h. Li, H.-j. Guo and W.-j. Peng, *Journal of Power Sources*, **153**, 174 (2006).
145. B. J. Hwang, Y. W. Wu, M. Venkateswarlu, M. Y. Cheng and R. Santhanam, *Journal of Power Sources*, **193**, 828 (2009).
146. G. Du, Y. NuLi, J. Yang and J. Wang, *Materials Research Bulletin*, **43**, 3607 (2008).
147. S.-T. Myung, S. Komaba, N. Kumagai, H. Yashiro, H.-T. Chung and T.-H. Cho, *Electrochimica Acta*, **47**, 2543 (2002).
148. J. C. Arrebola, A. Caballero, M. Cruz, L. Hernán, J. Morales and E. R. Castellón, *Advanced Functional Materials*, **16**, 1904 (2006).
149. J. H. Kim, S. T. Myung, C. S. Yoon, S. G. Kang and Y. K. Sun, *Chemistry of materials*, **16**, 906 (2004).
150. M. Mohamedi, D. Takahashi, T. Itoh and I. Uchida, *Electrochimica Acta*, **47**, 3483 (2002).

151. D. Y. Wang, A. Xiao, L. Wells and J. R. Dahn, *Journal of The Electrochemical Society*, **162**, A169 (2015).
152. K. H. Seng, L. Li, D.-P. Chen, Z. X. Chen, X.-L. Wang, H. K. Liu and Z. P. Guo, *Energy*, **58**, 707 (2013).
153. S.-W. Oh, S.-H. Park, J.-H. Kim, Y. C. Bae and Y.-K. Sun, *Journal of Power Sources*, **157**, 464 (2006).
154. J. Bauerle, *Journal of Physics and Chemistry of Solids*, **30**, 2657 (1969).
155. P. Duran, J. Jurado, C. Moure, N. Valverde and B. Steele, *Materials Chemistry and Physics*, **18**, 287 (1987).

Biographical Sketch

Ashley Ruth, nee Lidie, was born in Baltimore, Maryland. She grew up enjoying the natural treasures of the woods and streams in her own back yard, the Appalachian Mountains where both the extended family farm and hunting club are located, bobbing on the Chesapeake Bay and enjoying its famous crustaceans in the summer, and making the trip to Ocean City, MD at least once a year. Nature had proven to be fascinating, and what better way to study nature than to study the science of things, or materials. The love for all this state has to offer, in addition to some persuasive in-state scholarship funding, led Ashley to attend the University of Maryland for her undergraduate degree in Materials Science and Engineering.

Coming from a family of military servicemen in the Marines, National Guard, and Air Force, she selected an internship position working on transparent armor for the Army Research Laboratory after her freshman year. She continued to work for them for the remaining three years until graduation. This opportunity landed her the SMART Scholarship that provided her with the funding needed to go to graduate school and continue working for the Department of Defense. Deciding to shift gears while applying her ceramic background, she wanted to work in the energy field and found a great home in SOFCs under the guidance of Dr. Eric Wachsman at the University of Maryland, where she has spent her graduate school time thus far. Additionally, she spends her summers working in another energy research field, Li-ion batteries at CERDEC's Army Power Division. This appointment will become her full-time position upon graduation.